UNIVERSITÀ DEGLI STUDI DI PADOVA

SCUOLA DI INGEGNERIA

Dipartimento di Tecnica e Gestione dei Sistemi Industriali

Laurea Magistrale in Ingegneria Gestionale

Tesi di Laurea Magistrale

Characterization of the Lightweight Potential of Solid Solution Strengthened Ductile Iron

Relatore:
Ch.mo Prof. Franco Bonollo

Correlatori:
Moritz Riebisch, M.Sc.
Dr. Ing. Bjorn Püstal

Laureando:
Mattia Luise

Anno Accademico 2018/2019

"Home is behind, the world ahead,

and there are many paths to tread,

through shadows to the edge of night,

until the stars are all alight."

— **J.R.R. Tolkien, The Lord of the Rings**

Acknowledgements

I am grateful to my relator Prof. Franco Bonollo, to Università degli studi di Padova and to *Rheinisch-Westfälische Technische Hochschule* Aachen for the opportunity they gave me. Developing my master thesis abroad was the best way to finish my study path.

I also want to personally acknowledge my tutor and co-relator Moritz Riebisch and all the *Gießerei-Institut* personal for the patience and the time they dedicated to my project.

Thanks to my grandparents, that hosted and substained me for three and a half years (and counting).

Thanks to all my friends, the salt of my life.

Thanks to Mom and Dad, that made all of my life possible. I try my best every day to make you proud of your efforts.

Abstract

Silicon solid solution strengthened ductile iron (SSDI) is characterized by excellent static mechanical properties. Due to the graphitizing effect of the element silicon this material solidifies completely gray compared to conventional GJS even at higher cooling rates. Regarding the exploitation of lightweight potentials, this cast material is therefore of interest for the casting of thin-walled components (2-3 mm), both in sand castings and gravity die casting.

To develop the lightweight potential of solid solution strengthened ductile iron with up to 4.3% silicon for thin wall thicknesses, the wall thickness dependent analysis of casting properties and microstructure is necessary. For this purpose, the limits for the formation of a mottled structure as a function of the wall thickness and the Si content are determined experimentally using a suitable test geometry in sand (5-4-3-2-1 mm plates of 15 x 10 cm) and a permanent mold (a 3-step mold of 30-20-12 mm thickness). The aim is to avoid white solidification as much as possible.

This thesis is developed in two main parts: the first part analyzes the known features of ductile iron, from the mechanical properties to the metallographic characteristics; the second part describes the experiment, its preparation, the practical procedure, and the discussion of the results.

The results show that, in the conditions exposed above, it was possible to obtain a carbide free microstructure for a wall thickness inferior to 3 mm for the two alloys with higher Silicon content, the GJS-500-14 and the GJS-600-10, that also presented a fully ferritic matrix at 4 and 3.5 mm, respectively. The other two alloys analyzed present the same conditions at higher wall thicknesses; more specifically, it wasn't possible to obtain a fully ferritic matrix (less than 5 wt% of pearlite), but a carbide free microstructure was obtained at 4.5 and 3.5 mm. Mechanical tests showed that the 4 mm sample of the GJS-600-10 satisfies the DIN EN 1563 limits, while for the GJS-500-14 the 5 mm sample Elongation at rupture value was slightly under the limit. For the other two alloys it wasn't possible to match these values since none of the plates was found fully ferritic in the conditions of this work.

Italian Abstract

Le ghise sferoidali rinforzate con silicio in soluzione solida sono caratterizzate da eccellenti proprietà meccaniche statiche. Grazie all'effetto grafitizzante del silicio, queste ghise risultano essere completamente grigie rispetto alle convenzionali GJS, anche a tassi di raffreddamento più elevati. Questo materiale è dunque di interesse per la produzione di componenti a spessore sottile (2-3 mm), sia per la fonderia in sabbia, sia per stampi permanenti, grazie alle sue potenzialità di ridurre il peso dei componenti mantenendo inalterate le proprietà meccaniche.

Per poter sviluppare il potenziale di queste ghise (con tenore di silicio fino al 4.3%), è necessario mettere in relazione microstruttura e proprietà fisiche dei campioni ottenuti tramite le colate con lo spessore degli stessi campioni. A tale scopo, utilizzando un'apposita geometria sia di uno stampo in sabbia (piatti di 5-4-3-2-1 mm di spessore, delle dimensioni di 15 x 10 cm) sia di uno stampo permanente (stampo a 3 spessori di 30-20-12 mm, dalle dimensioni di 10 x 6 cm), si vuole determinare sperimentalmente la relazione tra la formazione di una struttura "mottled" (ossia contenente sia ghisa bianca sia ghisa grigia) e due fattori principali: lo spessore del getto e il contenuto di silicio. Lo scopo è limitare la formazione di questa struttura ed ottenere campioni privi di cementite.

La tesi è sviluppata in due sezioni principali: la prima parte analizza le caratteristiche note delle ghise sferoidali, dalle proprietà meccaniche all'analisi metallografica; la seconda parte descrive l'esperimento, la sua preparazione, la procedura pratica, e la discussione dei risultati. I risultati mostrano che, nelle condizioni in cui si è operato, è possibile ottenere strutture prive di cementite con pareti di spessore inferiore a 3 mm per le leghe GJS-500-14 e GJS-600-10, oltre a strutture completamente ferritiche rispettivamente a 4 e 3.5 mm di spessore. Le altre due leghe analizzate, GJS-400-10 e GJS-450-15, presentano le stesse condizioni a spessori maggiori, come auspicabile per l'inferiore contenuto di Silicio. Nello specifico, una struttura completamente ferritica (considerata tale ad un tenore di perlite inferiore al 5%) non è stata raggiunta, mentre è stata registrata l'assenza di cementite a 4.5 e 3.5 mm. I test meccanici hanno mostrato una corrispondenza (rispetto alla norma DIN EN 1563) dei risultati ottenuti per il campione di 4 mm di spessore della GJS-600-10, mentre per la GJS-500-14 sono stati ottenuti dei risultati leggermente sotto i limiti richiesti per quanto riguarda l'allungamento a rottura nel campione da 5 mm. Per le altre due leghe non era possibile raggiungere questi limiti in quanto nessun campione è stato trovato al 100% ferritico nelle condizioni di questo esperimento.

Table of contents

Introduction

Due to the necessary attention that must be paid to environmental problems, since many years the research in many industrial areas (especially automotive and transports) is led by the need to reduce the energetic impact of processes and materials. Focusing in automotive in general, the quest is mostly addressed into creating lighter materials with comparable or even better mechanical properties, since the consumption of fuel is the real key factor that determines the energy savings: it's reported in several automotive Life Cycle Assessment (LCA) that the Fuel Reduction Value (FRV) that can be obtained by reducing the weight of a car by 100 kg is between 0.15 and 0.35 l every 100 km [1], [2]. As reported by U.S. EIA [3], transports were responsible for over the 28% of the U.S. primary energy consumption in 2017, and the data of 2018 are following the same trend.

A very consistent solution through the years has been the substitution of cast iron alloys with aluminum alloys. This choice is justified by the low density of this material, and by many other advantages. As summed up by Fras et al. [4], some of them are:

- Low melting and pouring temperatures, that allow a relatively low mold pre-heating and the exploitation of permanent molds, that provide higher dimensional accuracy and improved surface quality.

- High thermal conduction which promotes an efficient cooling.

- Finishing and aesthetics.

- Non-magnetic nature, that helps the scrap selection processes.

These features progressively allowed Al to invade the market of cast-iron: an example of the Italian production trend of foundry pieces is reported in Figure 0.1 [5]. Beside 2007-2008 crisis, where both productions were strongly influenced, Al raised constantly in the last 20 years, while cast iron did not. More recent data are shown in Figure 0.2.

The development path for cast-iron is therefore trying to reach aluminum alloys in terms of weight, without losing his excellent mechanical properties that are consistently higher than its counterpart, as well as the better wear and damping properties, and the total energy consumption.
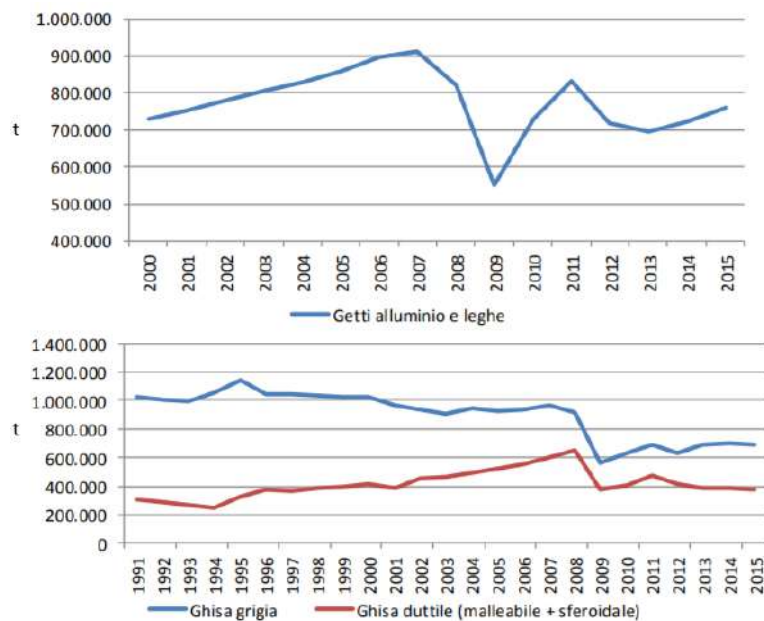
Figure 0.1: Italian production of Al and Al alloys (top) and graphitic irons castings (bottom, grey iron in blue and ductile iron in red).

Figure 0.2: Italian production of Al and Al alloys (top) and graphitic irons castings (bottom, grey iron in blue and ductile iron in red), recent update of June 2018.

2

Production costs and energy consumption of cast iron are way lower than aluminum components. An article by Frás summarizes this economic gap: a ton of primary Al produced by electrolysis requires from 164 to 171 GJ of energy, while 1 ton of pig iron needs about ten times less (from 16.8 to 18.8 GJ). Then, secondary Al production needs at least two melting processes, while cast iron melting is normally a one-phase procedure and can be melted many times without losing quality [4].

Another interesting comparison can be made about the cost per unit tensile strength of the materials, and also in this case cast iron (and ductile iron specifically) is cheaper than aluminum (see Table 0.1)

Table 0.1: Materials cost per tensile strength unit [4]

Material	Cost per TS Unit
Cast Iron	$\frac{1500\ \$/ton}{200\ to\ 250\ MPa} = 6.0\ to\ 7.5\ \$/MPa$
Ductile Iron	$\frac{1700\ \$/ton}{350\ to\ 900\ MPa} = 1.8\ to\ 4.8\ \$/MPa$
Aluminum Alloys	$\frac{8000\ \$/ton}{158\ to\ 310\ MPa} = 25.8\ to\ 50.6\ \$/MPa$

For this reason, several studies tried to find out how to realize cast-iron with a lower wall thickness, and this branch of alloys is named Thin Wall Ductile Iron (TWDI). As reported by Sulamet-Ariobimo et al. [6], the definition of the limit thickness for a cast-iron wall to be considered part of the group, changed several times: Caldera defined TWDI as ductile iron castings with a wall thickness below 5 mm, while Stefanescu considers a limit of 3 mm. In several experiments, it was possible to obtain castings of 1 mm of thickness, and this opportunity opens the road to new studies: the low thickness of the casting walls causes higher cooling rates, a problem for the formation of carbides and the optimization of the microstructure.

Already in 2002, Stefanescu et al. [7] published important results regarding TWDI, and it was found out that the analyzed plates (thickness between 1.5 and 7 mm) exceeded ASTM (American Society for Testing and Materials) specifications for as-cast ductile iron. The actual researches are focused on optimizing casting variables to obtain high performing thin wall components also in high Si content grades.

The European Standard for Ductile Cast Iron in 2012 introduced three new grades (bet-

ter explained later) at high Si content that take the name of Solution Strengthened Ductile Iron, that have a unique combination of tensile strength and elongation (for example Rm = 500 MPa and A = 14%).

The goal of this thesis was indeed finding a relation between the elements that effect the quality of the casting (content of some elements, pouring temperature, etc.), due to exploit the lightweight potential of this solid solution strengthened alloys, since their use in foundries is limited by the difficulty to obtain thin sections without macro metallurgical defects (mainly carbides) and that can consequently satisfy the standards. A further area of interest that can be related to the TWDI are the Thin Wall Austempered Ductile Iron (TWADI), that reach extremely high mechanical properties (comparable to some steels). The TWADI are supposed to reach a production of 300.000 tons by 2020 [6], but to reach a high quality in these alloys it's necessary to consolidate the knowledge of the TWDI that would be later austempered. However, this argument is not part of the present work.

Using a suitable geometry test both in a sand mold and in a permanent mold, several melts were performed to analyze the mechanical and metallographic features of SSDI, and characterize the lightweight potential od Solution Strenghtened Ductile Iron.

1 Solid Solution Strengthened Ductile Iron

The European Standard for ductile cast iron (EN-GJS) already since 2012 added to the standard some new alloys characterized by a solution-strengthened fully ferritic matrix, generated by a high silicon content, from 3 to 4.3 wt%. These new alloys, namely EN-GJS-450-18, EN-GJS-500-14, EN-GJS-600-10 have excellent mechanical properties and a cost-efficient machining (tool life is about 50-60% longer than the standard grades [8]). Also, cyclic properties are good thanks to the absence of the pearlite.

These features are possible since many improvements in the element analysis were made: the high content of Si, that promotes a ferritic matrix, enables a higher tolerance for pearlite and carbide promoting elements, that cause the embrittlement of the structure. Better inoculation techniques allow then an optimal graphite shape, a key factor for good mechanical properties.

Silicon gives better tensile properties up to a certain weight percentage, even though there are some controversial on this limit. More specifically, Stets et al. found that Si rises Yield Strength (from now on $R_{p0.2}$) and Ultimate Tensile Strength (UTS, from now on R_m) up to 4.6 wt% and 4.3 wt% respectively [8]. Glavas obtained a lower limit of 4.22 wt% for both values [9], while González-Martínez et al. [10] recently obtained consistently different results, namely 5.0-5.2 wt% for Rm and 5.2-5.4 wt%. However, as much higher these values are, the less elongation (from now on A_5) the material can sustain. Both papers confirmed the linear evolution on the hardness: a higher Si content causes embrittlement, that means a hardening of the matrix (however losing plasticity).

For these unique combination of properties, Silicon Solution Strenghtened Ductile Iron is expected to grow in terms of market demand, and especially in automotive engineering, research is active to promote the optimization of these grades, i.e. the possibility to use small wall thicknesses [8].

1.1 Metallographic Features

1.1.1 Graphite Shape

The distinctive feature of ductile irons is the spheroidal shape of the graphite, that starts to grow together with austenite after the eutectic temperature (in a range between $1147-1154$°C depending if the transformation is metastable or stable). At this temperature, if the iron has a grey solidification (helped by some elements like silicon and by slow cooling rates), the liquid starts to lose C and graphite starts to grow in the liquid. The growth of graphite can happen in two ways: horizontal growth (grey iron) or vertical growth (ductile iron), as shown in Figure 1.1. The vertical growth (layer by layer, Figure 1.3) leads to the formation of the spheroidal shape, that gives extraordinary ductility to the material, since it avoids the propagation of the dislocations, and it's the typology of material that was considered in this study. In this case, graphite starts to grow in the liquid and than results surrounded by austenite, while if the graphite is lamellar, it will always keep the contact with the liquid during the eutectic transformation.
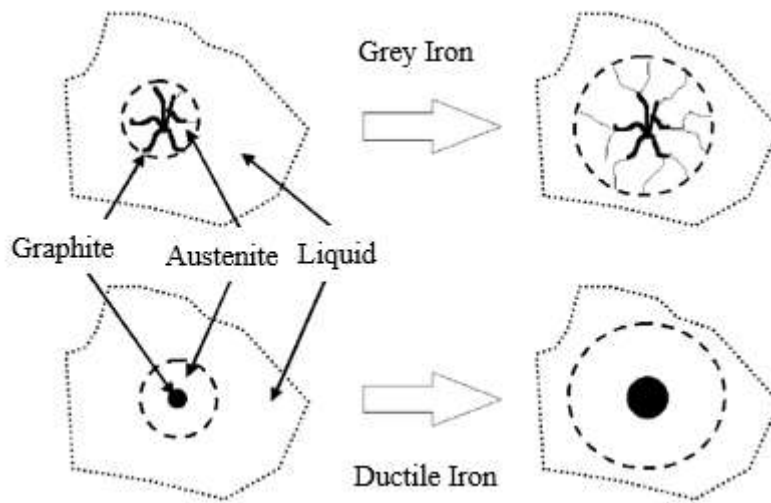

Figure 1.1: Nucleation of graphite nodules in the two ways, grey iron or ductile iron [11].

The vertical growth is helped by higher cooling rates and by the presence of some elements, especially Mg. The addition of Mg is called spheroidization, and it's a very sensitive operation, since the maximum content of this element is 0.06 wt%: after this level, Mg binds with C and O and creates inclusions. It's also an easily fading element.
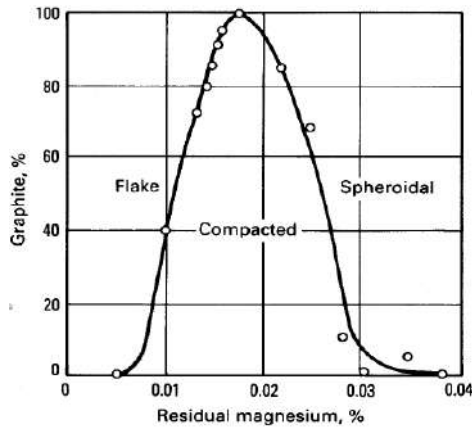
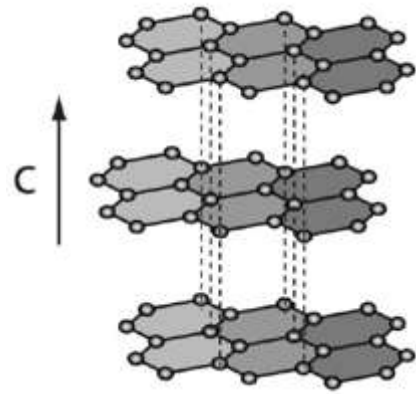Figure 1.2: Effect of Mg content on graphite shape [12]

Figure 1.3: Vertical layer growth of the lattice along the basal plane [12]

In general, graphitic irons (the family that includes both grey and ductile irons) can present 6 different graphite shapes, as shown in Figure 1.4
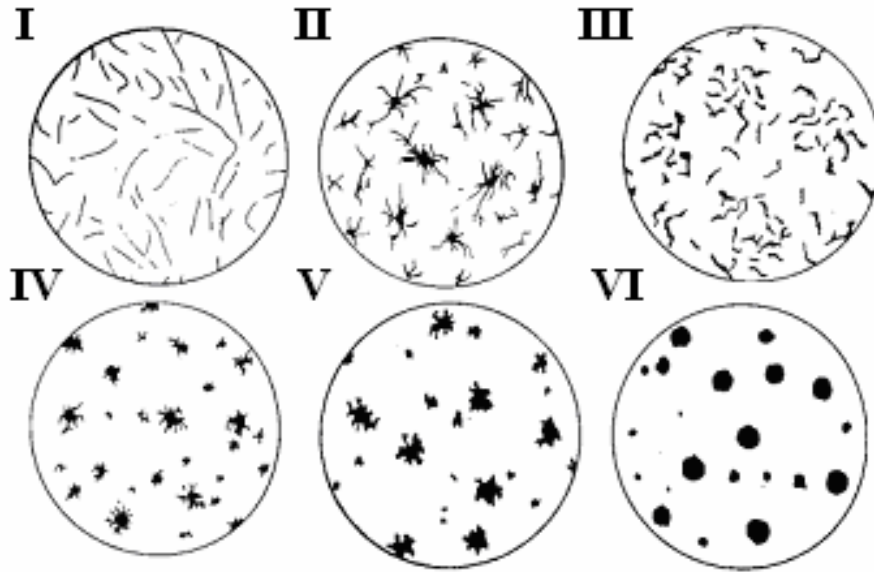

Figure 1.4: Graphite morphology in graphitic irons [13]

Type I and VI are grey iron and ductile iron respectively. Types from II to V are intermediate situations:

- Type II: Crab or Spiky.

- Type III: Vermicular or Compacted.

- Type IV: Exploded graphite.

- Type V: Malleable iron.

Obviously good mechanical properties depend on the shape of graphite, and the interest is necessarily to obtain a spheroidal shape. Many ways to determine the belonging of a nodule to this class (VI) were presented in the literature. As classified by Ruxanda [14] , the most common factors are Sphericity (S, Equation 1.1) and Compactness (C, Equation 1.9):

$$S = \frac{4 * \pi * Area}{(Perimeter)^2} \tag{1.1}$$

$$C = \frac{4 * \pi * Area}{(ConvexPerimeter)^2} \tag{1.2}$$

The difference between these two parameter is a variable called Convex Perimeter, exposed in Figure 1.5. Convex perimeter is calculated not taking account of convex indentations of the graphite nodules, so that it is possible to have a measure of how much the nodule has a compact structure.
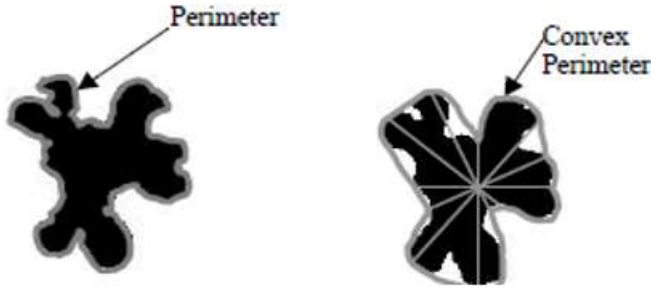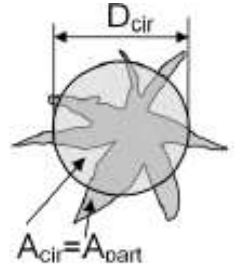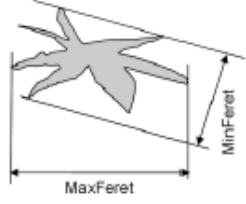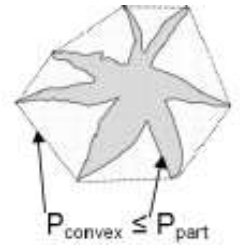

Figure 1.5: Difference between Perimeter and Convex Perimeter [14]

Other possible factors that are useful to classify graphite shapes are exposed by Velichko [15] (see Table 1.1).

Parameter	Formula	Description	Image
Roundness	$R = \dfrac{4 * Area}{\pi * (MaxFeret)^2}$ (1.3)	Ratio between object area and the area of the circumscribed circle	Figure 1.6: Roundness
Circularity	$Cir = \sqrt{\dfrac{4 * Area}{\pi * (MaxFeret)^2}}$ (1.4)	Ratio between the diameter of the circle with the same area of the object area and the object's maximum Feret diameter	Figure 1.7: Circularity
Aspect Ratio	$AR = \dfrac{MinFeret}{MaxFeret}$ (1.5)	Ratio between the object's minimum and maximum Feret diameter	Figure 1.8: Aspect Ratio
Convexity	$Conv = \left(\dfrac{ConvexP}{P}\right)^2$ (1.6)	Squared ratio between object's convex perimeter and its perimeter	Figure 1.9: Convexity

Ruxanda suggests considering a nodule acceptable if presents both S > 0.65 and C > 0.7. The magnification plays also a role in the nodule count since there is a dependence with the pixel size of the lens; the common analysis is performed between 100x and 200x.

Calculating these values allows to determine an important factor called nodularity, normally expressed in percentage. As defined in ASTM A247, the formula is:

$$\%Nodularity = \frac{Acceptable\ Particle\ Area}{Acceptable\ Particle\ Area\ +\ Unacceptable\ Particle\ Area} * 100 \quad (1.7)$$

This equation obviously considers acceptable a particle with the previously described features.

Another approach is presented by Velichko [15], where Roundness is taken instead of sphericity, and the classes are determined as a combination of it with compactness, as shown in Fig. 1.10:
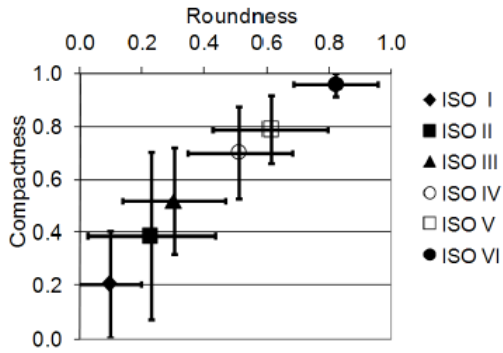

Figure 1.10: DIN EN ISO 945 classification method for graphite shapes

Consequently, it is possible to use a more specific equation to determine nodularity, as shown in Equation 1.8 [16]

$$\%Nodularity = \frac{\sum_{VI} A_i + \frac{1}{2}\sum_{IV}^{V} A_i}{\sum_{I}^{VI} A_i} * 100 \qquad (1.8)$$

Another element connected to the nodule count is the interparticle spacing (Equation

1.9, expressed in nodule count per mm^2, Seher, 1971). The higher the nodule count, the lower this index is. It basically represents the carbon diffusion distance.

$$\lambda_G = 55.4 * \left(\frac{d_{avg}}{Nodule\ Count} \right)^2 \qquad (1.9)$$

The wall thickness, and consequently the cooling rate has a direct impact on the nodule count: the higher the cooling rate, the higher the number of nodules (Figure 1.11), with a necessary positive impact on mechanical properties and fatigue resistance, as it will be pointed out in the next paragraph.
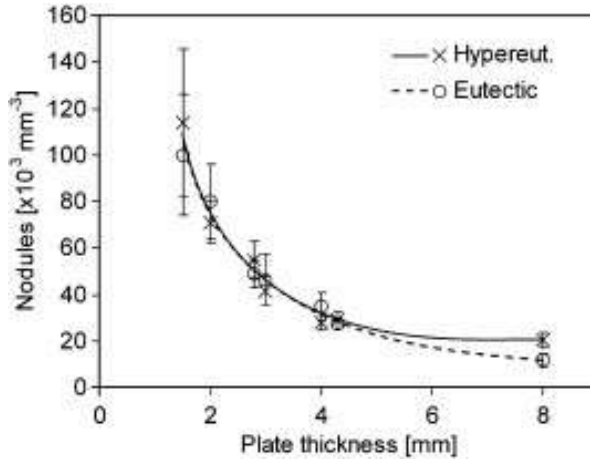
Figure 1.11: Relation between wall thickness and nodules count [17]

A highly sensitive parameter that can influence the nodularization is the rare earth content. Rare earths (RE) are necessary in a low amount to contrast the anti-nodularizing effect of some elements like lead (Pb) or titanium (Ti). Also, Sb and Bi if added in excess are deleterious, but still they have a meaning especially in thin walled applications, as it will be pointed out. However, rare earths help controlling all these elements. An article by Choi et al. analyses the effect of RE on thin wall ductile iron castings, and it was confirmed that RE help the nodularization, more in the thinner plates than in the thicker [18], up to a RE content of 0.2 wt% (Figure 1.12, Figure 1.13).
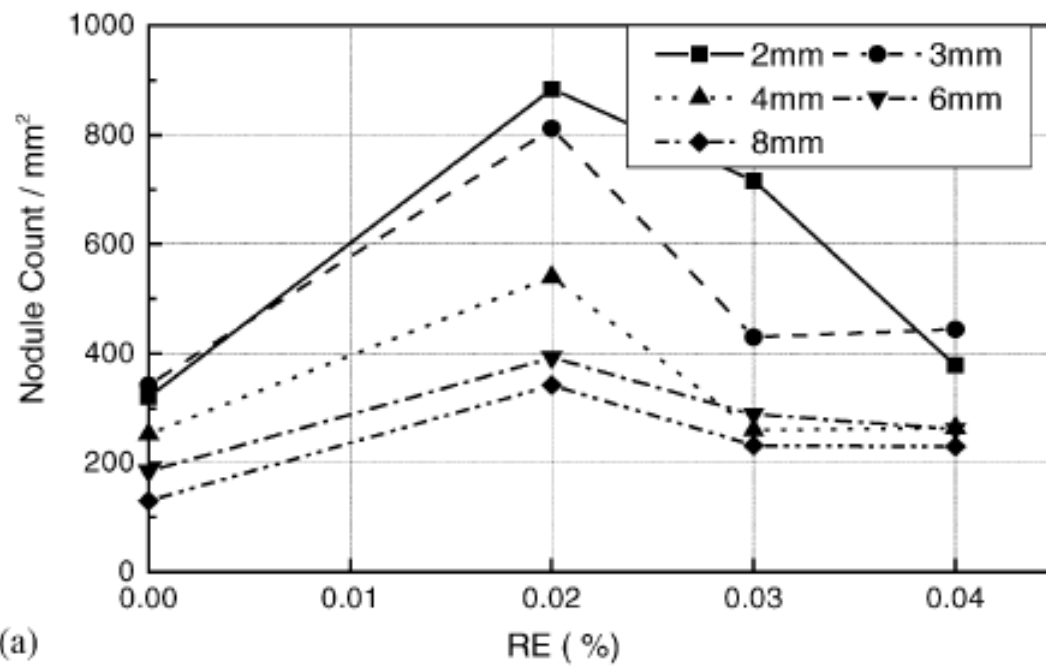
(a)

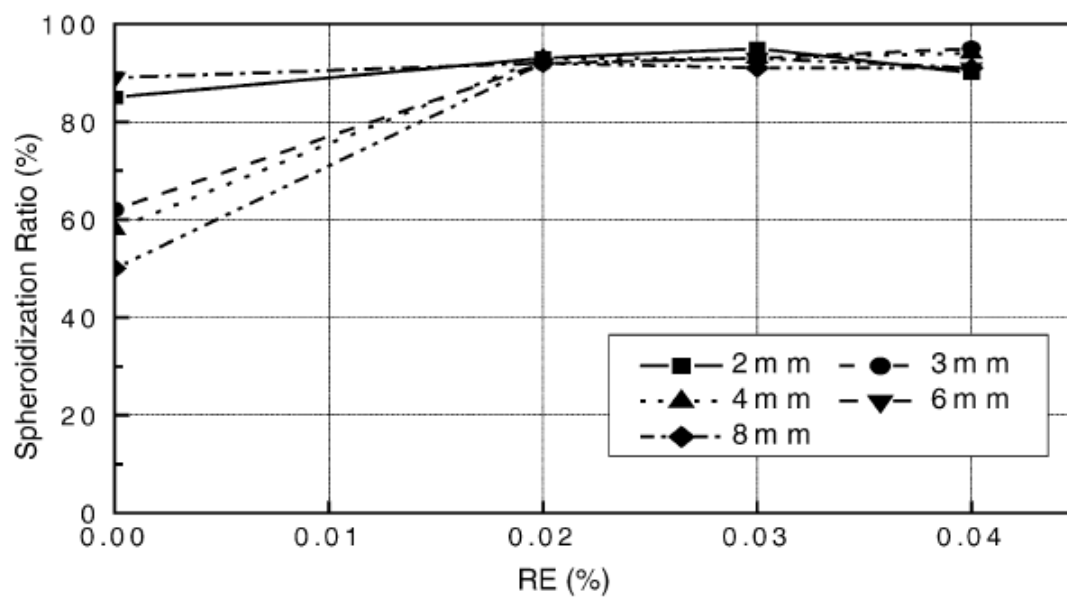Figure 1.12: Effect of Rare Earths on Nodule Count

Figure 1.13: Effect of Rare Earths on Spheroidization Ratio

12

1.1.2 Ferrite and Pearlite Formation

After the eutectic transformation of the liquid, other transformations happen as it will be pointed out. When these transformations are over, at room temperature ductile iron can present a matrix composed by pearlite or ferrite (or a combination of them) and graphite nodules. The result depends on the chemical composition and on the cooling rate.

Elements like Si and Al are ferrite promoters, while Cu, Sn, Mn, Cr are pearlite promoters. In Table 1.2 the effects of the main elements are shown.

Table 1.2: Effect of the main alloying elements on cast iron matrix [19]

Element	wt% Range	Positive Effect	Negative Effect
Ferrite Promoters			
Si	1.8-4.3	Promotes graphite formation since widens the eutectic transformation range. At high contents helps to avoid carbides in thin sections. Ferrite promoter.	Can segregate negatively. Embrittles the ferrite at high contents.
Al	0.003-0.06	Deoxidizer. Like Si, increases the stable eutectic temperature and decrease the metastable eutectic temperature. Ferrite promoter.	Promotes vermicular graphite.
Pearlite Promoters			
Cu	0.01-0.9	Graphite promoter. In combination with Mo gives great hardness to the structure. Pearlite promoter.	Only refines pearlite weakly. Must be used at high purity, otherwise gives problem with Pb, As, Te, Sn, H.

Sn	< 0.1	Excellent pearlite promoter. Together with Cu gives higher pearlite contents in heavier sections and a more homogeneous matrix.	Can lead to embrittlement. At >0.10% form flake graphite.
Mn	<1.2	Promote pearlite and decrease the metastable eutectic temperature.	Moderate carbide promoter. Decreases the stable eutectic temperature
Cr	<0.05	Pearlite promoter, to keep as low as possible.	Carbide promoter. Reduces the eutectic temperature range.
P	<0.5	Pearlite promoter, to keep as low as possible.	Carbide promoter.
Pearlite Refiners			
Ni	0.01-2.00	Promotes and refines pearlite. Reduce chilling and carbides. Graphite promoter. Minimize variations in mechanical properties between thin and thick.	Segregate negatively.
Mo	0.01-0.75	Graphite promoter, since decreases metastable eutectic temperature. In combination with Cu, Ni and Cr hardens the structure.	Carbide promoter. Decrease the stable eutectic temperature.
V	<0.03	Strongly hardenening element. Mid pearlite promoter and pearlite refiner.	Strong chill and carbide former.

		Spheroidizing Elements	
Mg	0.03-0.05	Deoxidizer and desulphurizer. Main element that promotes spheroidization (ductile iron). Decreases the metastable eutectic temperature.	High content promotes dross defects and carbides, low content compact graphite. Fades at high temperature (evanescence). Decrease the stable eutectic temperature.
Rare Earths (RE)	<0.03	Together with Bi have the greatest effect on thin wall sections. Decrease the amount of carbide and increase nodule count and quality. Neutralize deleterious effects of elements such as Pb, Sb, Bi and Ti.	Excess promotes carbides in thin sections and chunky graphite in heavy sections.
Ca	<0.03	Increase nodule count and improves nodule quality. Reduce the fading rate of Mg.	Can give problems with slag. Cancels the effect of Sr (increasing nodule count).
Ba	<0.01	Increase nodule count. Optimizes inoculation.	
Ce	<0.01	Causes spheroidization and improves Mg recovery. Neutralize undesirable trace elements. Fades slower than Mg.	Less adaptable and cheap than Mg. Promote chunky graphite in heavy sections. In excess is a strong carbide former.

Pearlite (Figure 1.14 is a lamellar eutectic structure of ferrite and cementite (Fe_3C) and gives higher values of R_m and $R_{p0.2}$ compared to ferrite (Figure 1.15), that on the other hand gives better ductility.
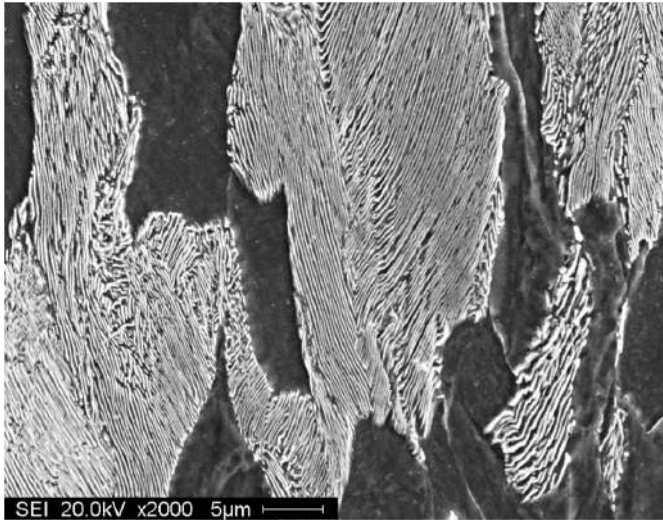
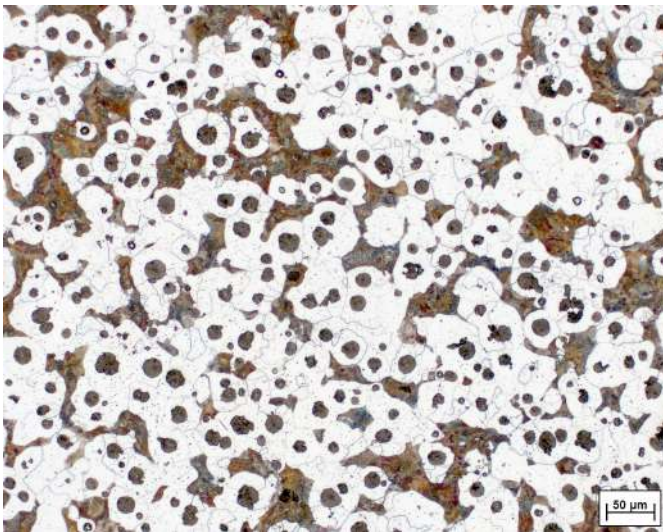Figure 1.14: Pearlite lamellar structure caught with a scanning electron microscope [20]

Figure 1.15: Ferrite rings (white) around graphite nodules. Brown areas are the pearlite fractions of the matrix. Photo taken in the Gießerei-Institut

Both structures are originated by the decomposition of austenite (γ phase iron and C in solid solution) between the eutectic temperature and the eutectoid temperature (738°C). In this interval, austenite loses C that is received by the graphite nodules, and ferrite α starts to grow at the graphite nodules boundaries, as shown in Figure 1.16.

16

Figure 1.16: Formation of ferrite around graphite nodules [21]

After the first phases of this process, C must reach the graphite through diffusion, since the ferrite completely surrounds the graphite nodules. This process is helped by low cooling rates, since a more stable transformation can occur. If these conditions are not enough present, the formation of ferrite goes along with the formation of cementite (C aggregates with ferrite), and this leads to the formation of pearlite. Pearlite starts to form at austenite grain boundary: when austenite starts to lose C, a cementite needle nucleates at the boundary, and the surrounding area results poorer in C, and this causes the formation of a ferrite needle (Fe-α poor of C). This mechanism goes on until all the austenite is transformed. Pearlite growth is much faster than ferrite.
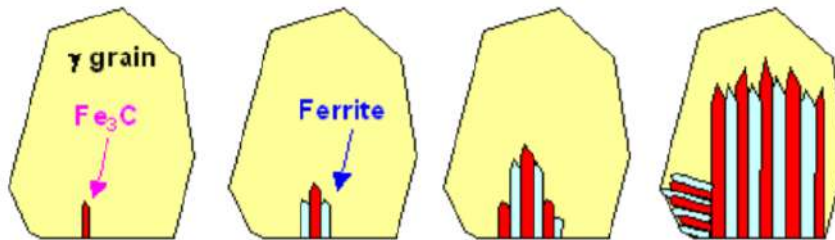
Figure 1.17: Formation of pearlite at grain boundaries [22]

The combination of ferrite and pearlite obviously influences mechanical properties: a standard ferritic ductile iron reaches 400 MPa, while a perlitic can reach up to 700 MPa of Rm. However, the main difference between traditional Ductile Irons and Solid Solution Strenghtened Ductile Irons is the Si content. In Table 1.3 an example of the chemical composition of the 3 new grades introduced in 2012 and that will be part of this study:

Table 1.3: Typical SSDI grades composition in wt% [23]

	Si	P	Mn
EN-GJS-450-18	3.2	0.05	<0.5
EN-GJS-500-14	3.8	0.05	<0.5
EN-GJS-600-10	4.3	0.05	<0.5

Silicon promotes the graphite formation instead of the cementite, and the formation of a ferritic matrix. As exposed by Glavas experiment [9], an amount of Si over 3.80 wt% leads to the formation of a fully ferritic matrix, and already with a 3.11 wt% the pearlite content is very low (1.9 wt%). The ferritic matrix is the element that provides better ductility and machinability. In the next sections the effect of Si on mechanical properties will be discussed.

Figure 1.18 sums up all the possible cast iron microstructures that can be obtained in relation to the cooling rate [24]:
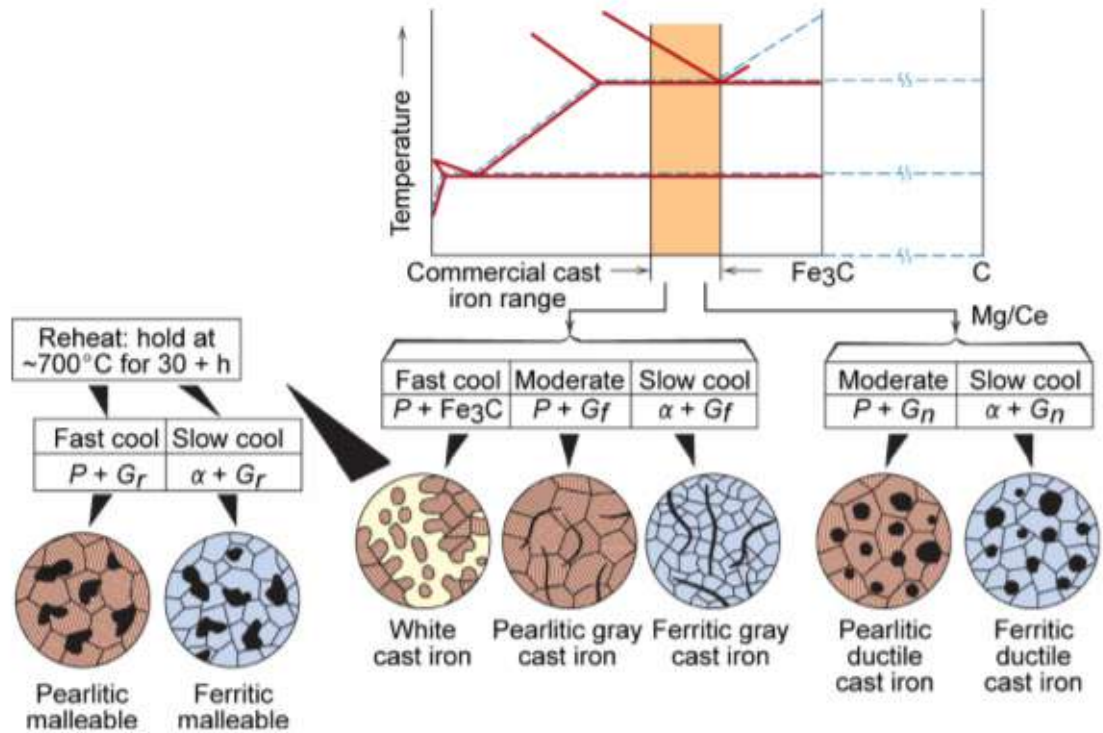
Figure 1.18: Cast iron microstructures in relation with cooling rate

1.1.3 Solid Solution Strengthening

Solid solution strengthening is a basic concept below every alloyed element: adding a solute element to the crystalline lattice of an element, this structure changes: in fact, the lattice results distorted, and it's harder for the dislocations to cross the material and damaging it. Steel and cast iron are stronger than pure iron since carbon is a solid solution into iron and it creates a strain in the matrix. These processes at the atomic level result in an increase in strength (R_m, $R_{p0.2}$, Hardness) and a reduction in plasticity [25].

The strengthening (or hardening) with solid solution can result in two different ways of substitution: interstitial or substitutional Fig. 1.14. In substitutional solid solutions, the added atoms take the place of one of the atoms of the pre-existing phase, without changing the lattice structure. Substitution can be unlimited or limited; most of the time the matrix has a solubility limit, that if is overcome, brings to a total change of the lattice. The conditions to understand if a solid solution is unlimited are exposed by William Hume-Rothery:

- Minimum difference between the radius of the solvent and the solute (maximum 15%).

- The materials must have the same crystal structure (for Fe-C is faced-centered cubic for Fe-γ and body centered cubic for Fe-α after solidification).

- The elements must have the same valence; in other words, belonging to the same group of the periodic table.

- The elements must have similar electronegativity, to avoid the formation of ionic and co-valent bonds.

Interstitial solid solution can otherwise happen just if the atom radius of the solute element is enough smaller than the radius of the elements of the matrix. Regarding Fe-C alloys, interstitial elements are H (hydrogen), O (oxygen), N (nitrogen), C (carbon), B (boron). The necessary conditions that allow the possibility of an interstitial solid solution is expressed again by Hume-Rothery with the following equation:

$$0.41 < \frac{r_{solute}}{r_{solvent}} < 0.59 \qquad (1.10)$$

SSDI exploit again this physical fact, adding Si as a solute element. The solid solution strengthening in spheroidal graphite cast iron is not a new concept, and especially the role of Si on mechanical properties will be discussed in the "Mechanical properties" section. An important factor that must be observed is that beside gaining strength because of the distortion of the lattice caused by the substitutional solid solution of Si, SSDI are not characterized by an embrittlement if compared to the conventional ductile ferritic-perlitic irons; this is again promoted by silicon. As mentioned before, Si has a key role into the precipitation of graphite instead of cementite carbides, and it is a ferrite promoter. Ferritic matrix is the reason behind the fact that SSDI keep excellent ductility values beside the solution strengthening.
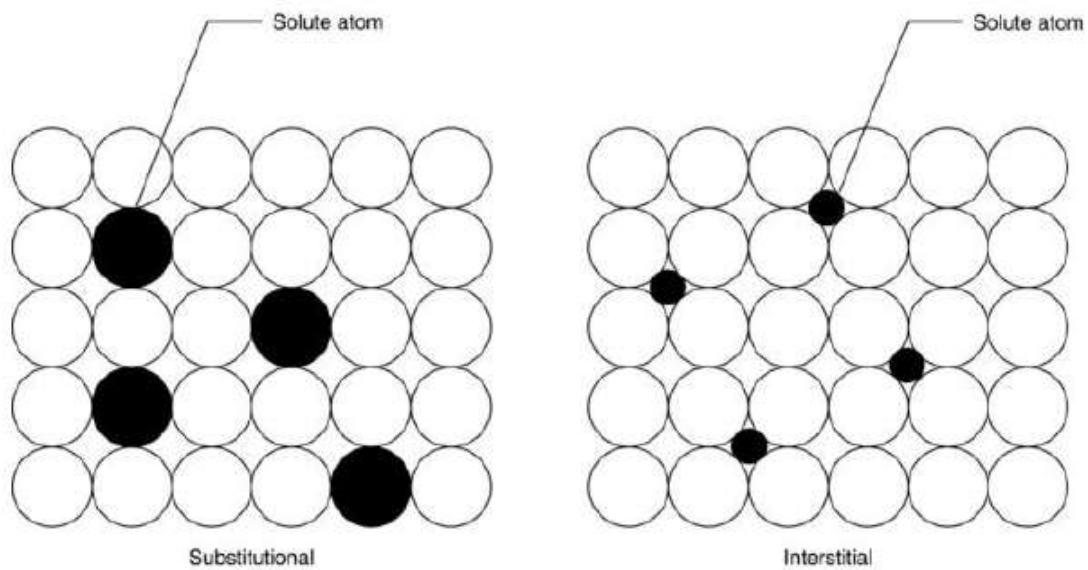
Figure 1.19: Solid Solution Possibilities [26]

1.1.4 Inoculation Process

Inoculation is a necessary passage in ductile iron foundry processes, because it allows the formation of graphite even in thin-walled components, where Si content could not be enough and higher cooling rates make the formation of carbides easier.

Inoculation consists in adding to the melted alloy some heterogeneous agents that have the key role to perform as grafting point for the nucleation of graphite. These inoculants are ferro - silicon based fine powders containing elements like Ca, Al, Zr (Zirconium), Ba (Barium), RE, Bi. According to [27], the introduction of these powders allows the formation

of hexagonal silicate phases on the surface of the oxide inclusions that are formed during the Mg treatment (MgO $\cdot$ SiO$_2$, 2MgO $\cdot$ SiO$_2$), probably due to an exchange reaction with MgO, and these phases (XO $\cdot$ SiO$_2$, XO $\cdot$ Al$_2$O$_3$ $\cdot$ 2SiO$_2$,with X representing Cr, Sa or Ba) help the nucleation of the graphite (see Figure 1.20)

The effect is function of the type of inoculant, but normally these operations can lead to a good uniformity on the composition. Another variable to be considered is time, since the effect of the inculation tends to reduce for longer solidifications (thick walled components): it's the so-called fading effect.
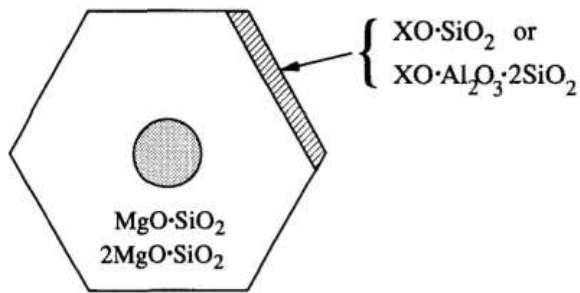
Figure 1.20: Effect of inoculation: Silicate phase on the surface of the oxide inclusion formed during the Mg treatment help the nuclation of graphite.

1.2 Mechanical Properties

As for every metallic material, mechanical properties depend from the microstructure at room temperature. For the moment the effect of thermic treatments is not included in the analysis. Conventional ductile irons have a wide range of mechanical behaviors, depending on the ferritic / perlitic ratio. In Figure 1.21 the mechanical properties of the main microstructures are exposed. The numbers in the green boxes are R_m.
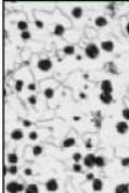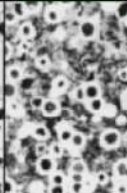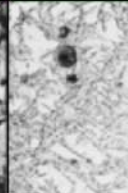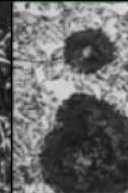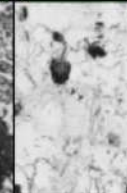
MATRIX							
Ferritic Grade 60-40-18	Ferritic-pearlitic Grade 80-55-06	Pearlitic Grade 100-70-03	Martensitic (With retained austenite)	Tempered Martensitic	ADI Grade 150-100-70	ADI Grade 230-185-	Austenitic
414 MPa	552 MPa	690 MPa	~600 MPa	793 MPa	1050 MPa	1600 MPa	310 MPa

Figure 1.21: R_m depending on the final microstructure. This notation follows the ASTM Standards, where the first and the second number are R_m and $R_{p0.2}$ expressed in ksi (kilopound per square inch, 1 ksi = 6.895 MPa) [12].

Obviously, also the cooling rate (and consequently the section thickness) has a considerable effect on the final properties, as shown in Figure 1.22. The reason is the graphite grains number and size that prevent the dislocation movement.
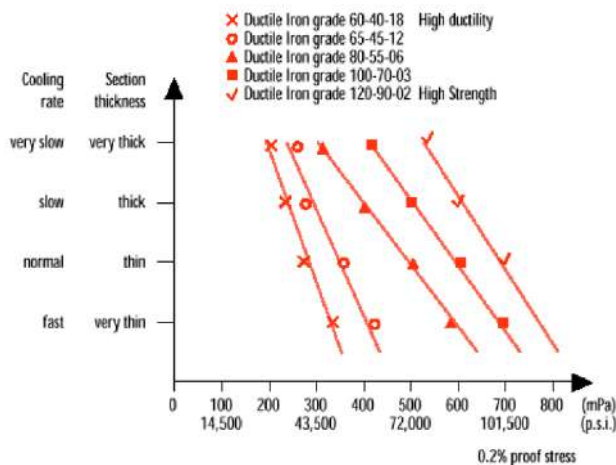
Figure 1.22: Effect of cooling rate on $R_{p0.2}$ [12]

It is also clear that higher levels of $R_{p0.2}$ and R_m lead to a general embrittlement, and consequently to lower levels of elongation (A, Figure 1.23):
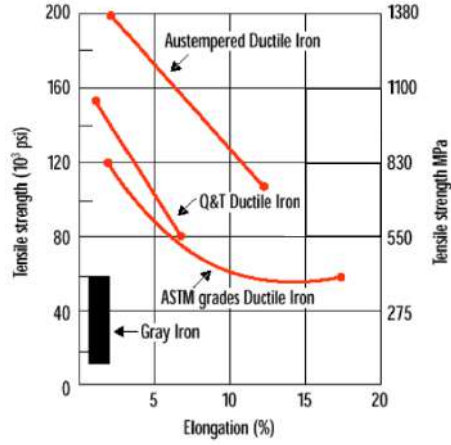

Figure 1.23: Tensile Strength R_m and elongation A_5 correlation [12]

More specifically, in the minimum tolerance of conventional ductile iron grades are exposed in Table 1.4, according to EN 1563:

Table 1.4: Conventional ductile iron tolerances according to EN 1563

Grade	Tensile Strength R_m	Yield Strength $R_{p0.2}$	Elongation A%
EN-GJS-350-22-LT	350	220	22
EN-GJS-350-22-RT	350	220	22
EN-GJS-350-22	350	220	22
EN-GJS-400-18-LT	400	240	18
EN-GJS-400-18-RT	400	250	18
EN-GJS-400-18	400	250	18
EN-GJS-400-15	400	250	15
EN-GJS-450-10	450	310	10
EN-GJS-500-7	500	320	7
EN-GJS-600-3	600	370	3
EN-GJS-700-2	700	420	2
EN-GJS-800-2	800	480	2
EN-GJS-900-2	900	600	2

23

The same rules are valid also for SSDI, but with a unique combination of higher tensile properties and elongation thanks to the ferritic matrix and the silicon solid solution strengthening. According to DIN EN 1536, the accepted values of SSDI are exposed in Table 1.5. As it can be noticed, the SSDI present both higher ductility and better tensile properties than conventional grades, A good indicator of the improvement could be the $R_m/R_{p0.2}$ ratio.

Table 1.5: SSDI mechanical properties according to DIN EN 1536 (Relevant wall thickness lower than 30 mm)

Grade	Tensile Strength R_m	Yield Strength $R_{p0.2}$	Elongation A%
EN-GJS-450-18	450	350	18
EN-GJS-500-14	500	400	14
EN-GJS-600-10	600	470	10

Many investigations were performed to analyze the effect of Si on the increasing of these indicators. Glavas et al. [9] performed a study to understand which was the tolerance limit for Si before the mechanical properties before the material would suffer a drop, and it was found that both R_m and $R_{p0.2}$ increase with a higher content of Si, up to 4.22 wt%. Elongation decreases with higher Si, but still less than it happens with conventional grades. Finally, it was confirmed that SSDI have a higher $R_m/R_{p0.2}$ ratio, and this means that Si effects the yield strength more than the UTS.

Stets et al. [8] also studied this behavior and similar but more detailed information were found. Specifically, tensile strength grows up to 4.3 wt% of Si (slightly higher than Glavas results, most likely for the higher number of melts performed), and yield strength drops just after 4.6 wt% of Si. By the way the embrittlement is already consistent at 4.2 wt%, and at 5 wt% R_m and $R_{p0.2}$ coincide, and elongation is no longer measurable. Results are exposed in Figure 1.24 and Figure 1.25).
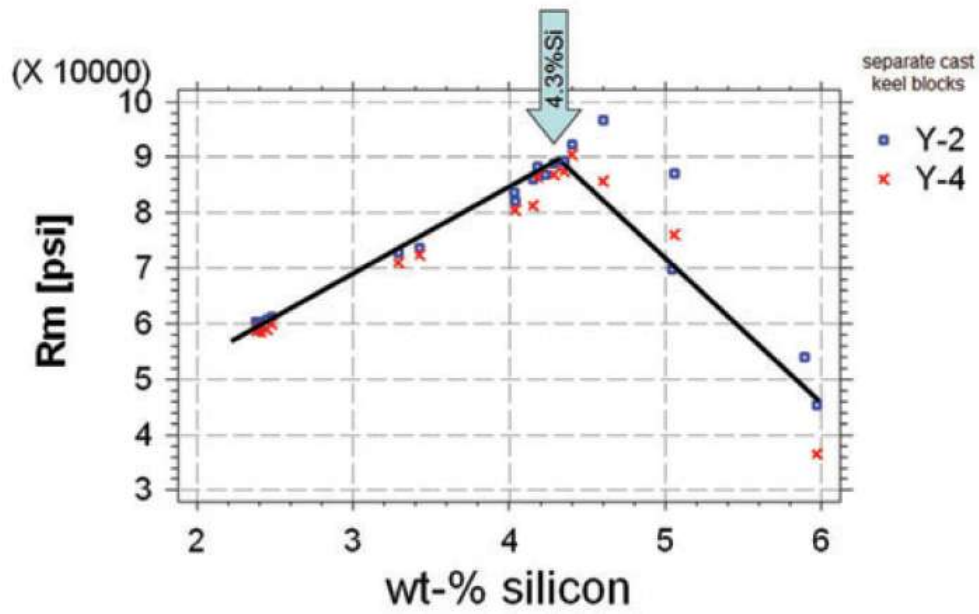
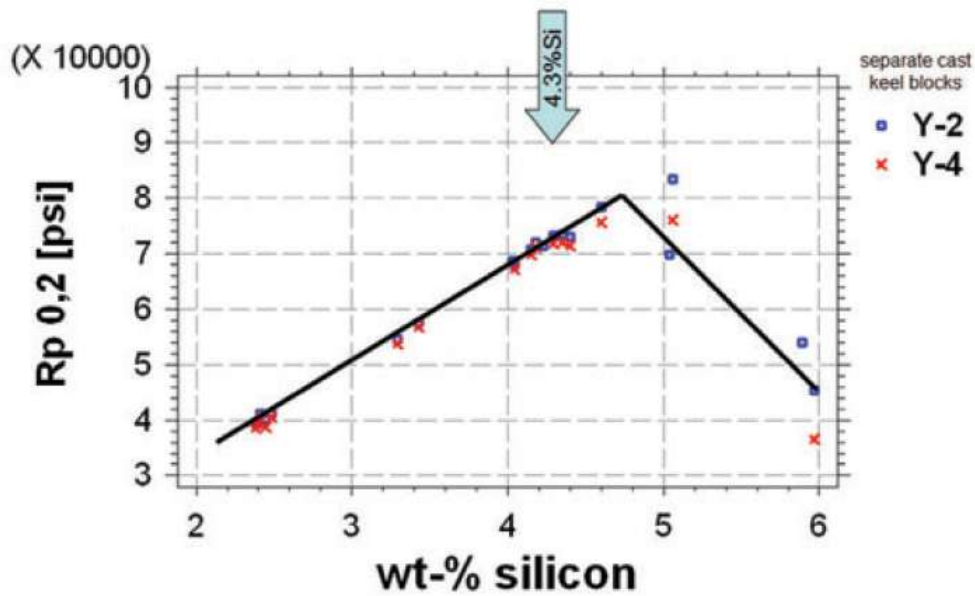Figure 1.24: Stets results: UTS drops after 4.3 wt% of Si

Figure 1.25: Stets results: yield strength drops after 4.6 wt% of Si

A recent publication by González-Martínez et al. though showed different results that can open investigations for even higher Si content cats iron. It was found that Si rises R_m and $R_{p0.2}$ up to 5.0-5.2 wt% and 5.2-5.4 wt% respectively. The same author underlines these differences in comparison with previous results. The data are exposed in Figure 1.26, where also values of Brinell hardness test are reported. Since Si causes distortion into the lattice

structure, there is a linear correlation between hardness and Si content, that in this case doesn't have a maximum peak (also see Figure 1.27). Similar data are obtained by Ghasemi, that analyzed SSDI plates of various thicknesses (up to a minimum of 7 mm, see Figure 1.28).
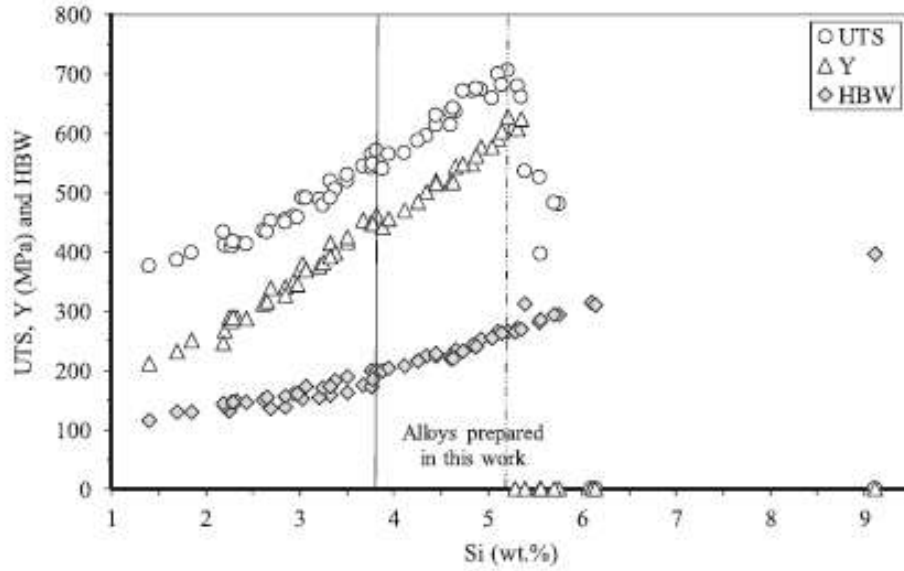
Figure 1.26: González-Martínez: Evolution of UTS, yield strength and Brinell hardness test [10]
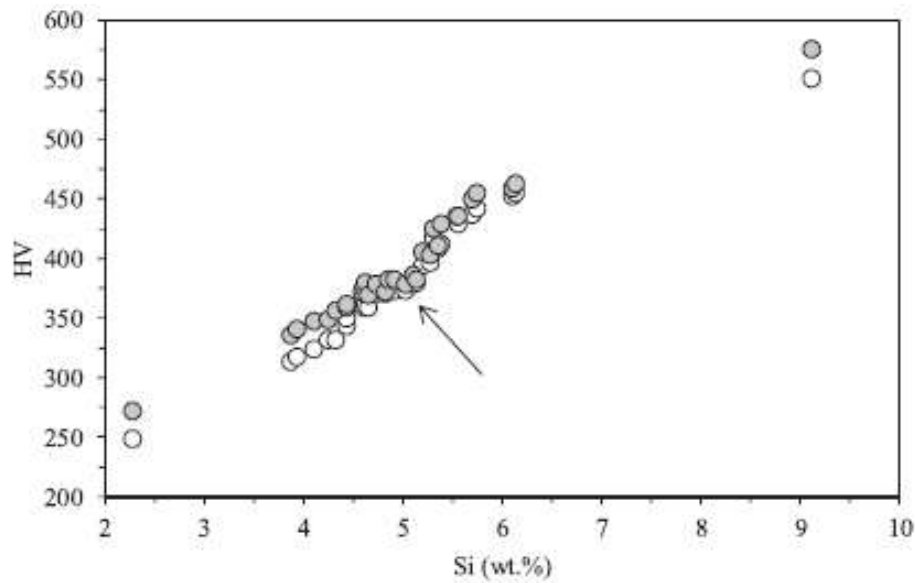
Figure 1.27: González-Martínez: Vickers hardness values depending on Si content [10]
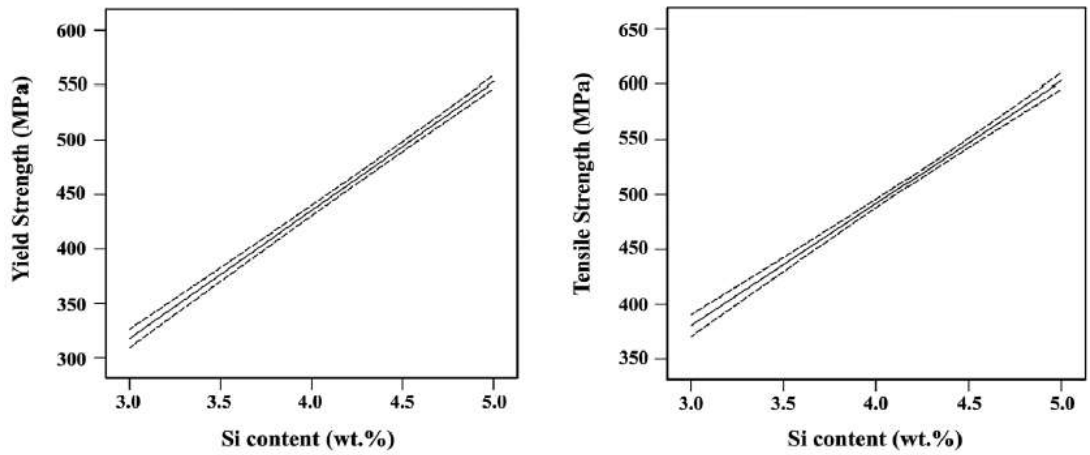
Figure 1.28: Ghasemi results, Si rises UTS and yield strength over 4.4 wt% [28]

In the same study, also elongation at rupture A% has been analyzed, and it was confirmed that Si contrast elongation, as a direct consequence of the embrittlement of the lattice. Another interesting point that results from 1.29 is the correlation between Si content and chunky graphite, that will be discussed in the following chapter.
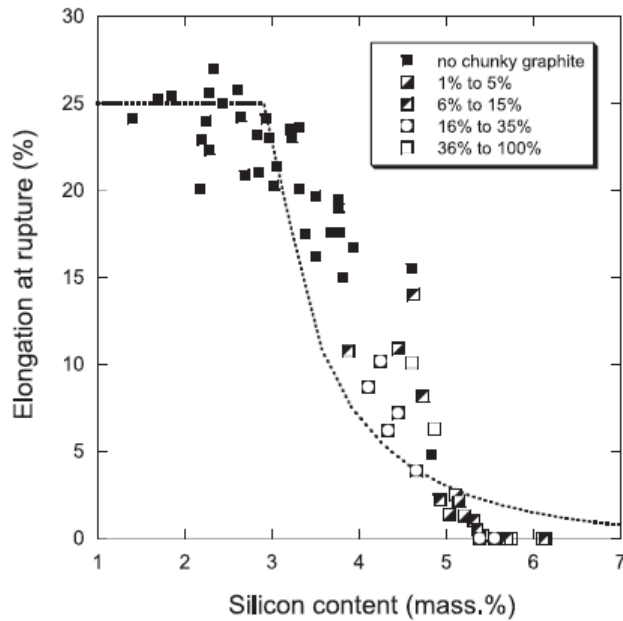
Figure 1.29: Elongation at rupture as a function of silicon content

Then, because of the ferritic matrix, machinability improves consistently, about 50-60% more than conventional ferritic-perlitic grades [8], and a higher plasticity on Charpy tests. As previously pointed out, the nodule count influences the fatigue properties. Cooling rate

helps the formation on nodules, and at the same time the average size of the nodules reduces, because of the lower diffusion distance (λ_G reduces since it is function of the nodule count). A study from Caldera investigated the relation between the nodule count and the fatigue properties, and the theory was confirmed [29]. Figure **??** and Figure 1.31 show how lower thickness components, characterized by a higher nodule count, have both higher endurance limit and fatigue resistance.
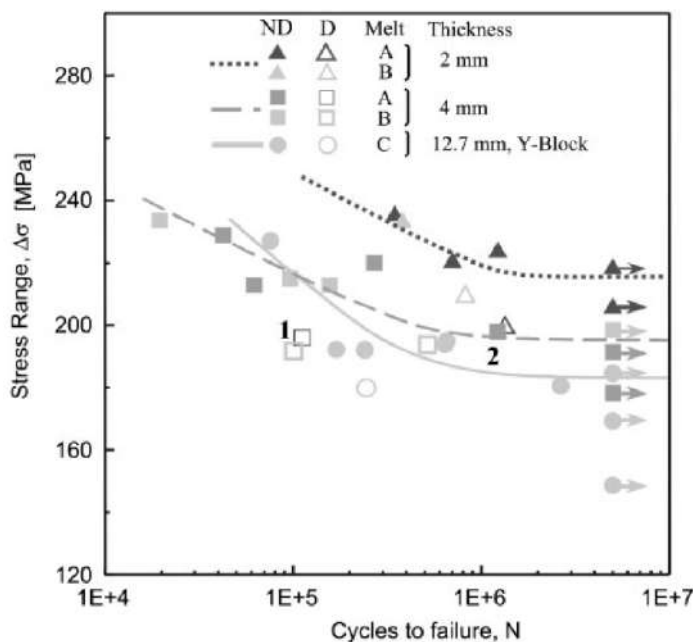
Figure 1.30: Stress range-number of cycles to failure relation considering castings of different thicknesses [29]
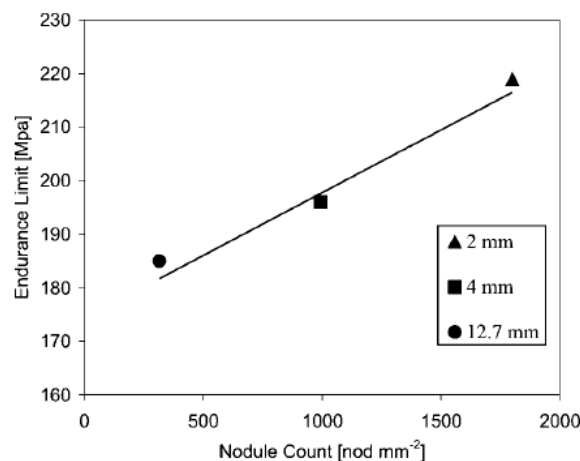
Figure 1.31: Nodule count - Endurance limit relation [29]

In Figure 1.32 and Figure 1.33 another example of the direct relation between fatigue limit and nodule count is shown in two different samples, unnotched and V-notched.
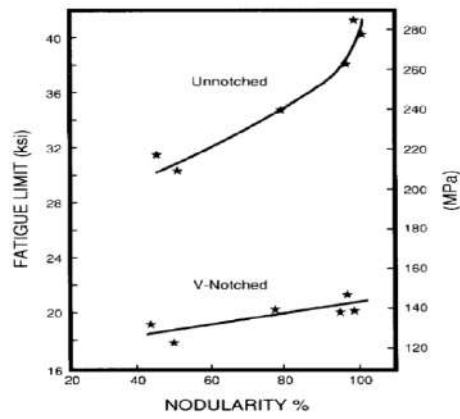
Figure 1.32: Relation between fatigue limit and nodularity [12]
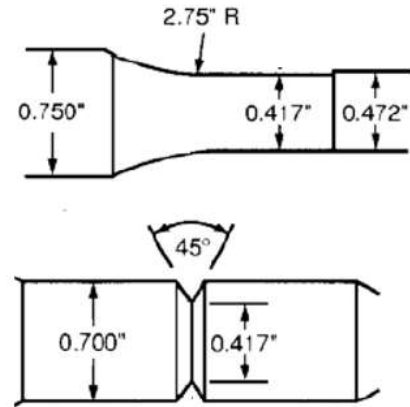
Figure 1.33: Unnotched and V-Notched samples [12]

1.3 Ductile Iron Defects and Specific TWDI Problems

1.3.1 Poorly Spheroidal Shape of the Graphite

Since the searched physical feature of ductile iron in general is the spheroidal shape of the graphite nodules, it can be considered a defect having poor spheroidization, i.e. a low fraction of nodules that can be classified as type VI. This problem can appear for a lack of spheroidizing elements (mainly errors with the Mg treatment) or for an excess of anti-nodularizing agents, mostly Sulphur. For example, spiky graphite (Type II, Figure 1.34) can be caused by effect of rare earths, that could not neutralize the deleterious effect of elements such as lead (Pb), bismuth (Bi), titanium (Ti) and antimony (Sb). Compacted or vermicular graphite (Type III, Figure 1.35) can be caused by an excess of Sulphur and/or by a low Mg amount and high holding time at high temperatures. An excess of rare earths, together with thick walls (lower cooling rates) can cause exploded graphite (Type IV, Figure 1.36), also more common for higher equivalent carbon contents. An article by Takeda et al. [30] enhances how a refinement on graphite nodules can be obtained adding a small amount of Bismuth. Bi was confirmed to be a graphitizing element, promoting a higher nodule count. On the other hand, it causes a decrease on the particle diameter, but this is not necessarily deleterious (see Figure 1.37, Figure 1.38, Figure 1.39).
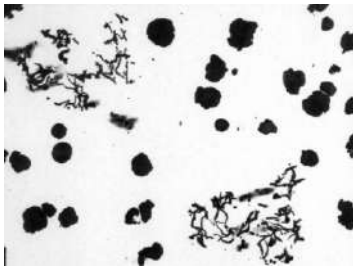
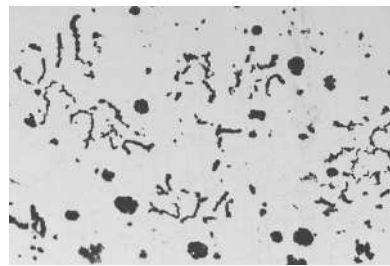

Figure 1.34: Spiky Graphite (Type II) [31]

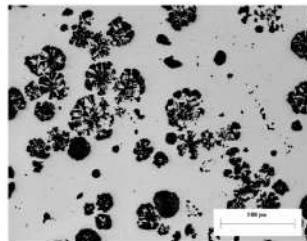*Figure 1.35: Vermicular Graphite (Type III) [31]*

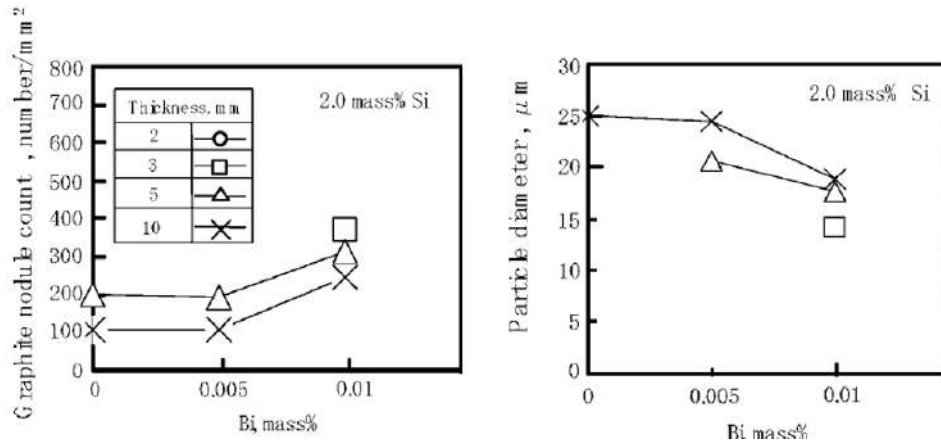*Figure 1.36: Exploded Graphite (Type IV) [31]*

Figure 1.37: Effect of Bismuth on nodule count and particle diameter (1) [30]
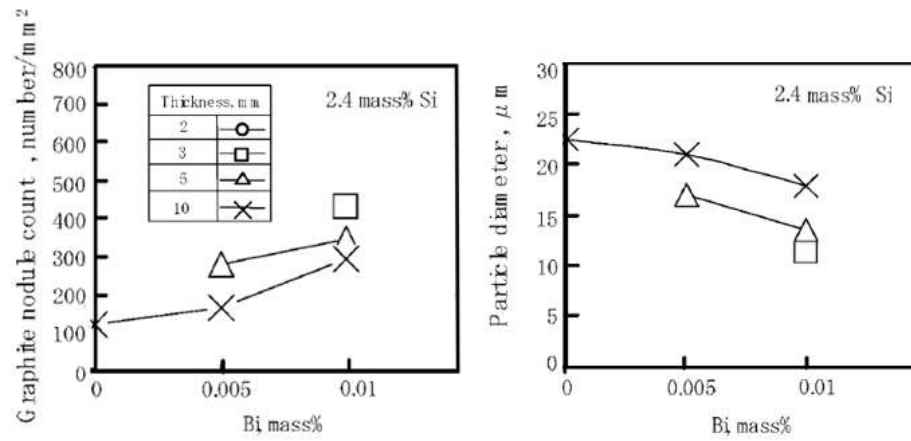

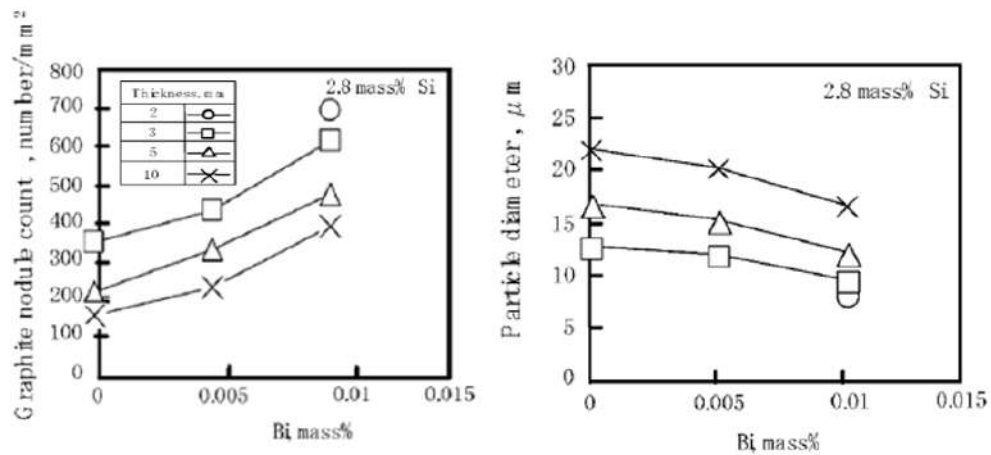*Figure 1.38: Effect of Bismuth on nodule count and particle diameter (2) [30]*

Figure 1.39: Effect of Bismuth on nodule count and particle diameter (3) [30]

1.3.2 Chunky Graphite

A defect that can be more characteristic in thicker sections ductile irons structures is chunky graphite (Figure 1.41). This structure is reported to appear more frequently at high Si and for an excessive concentration of rare earths [32]. It is also well known that Mg and Ce increase the risk of chunky graphite formation, surely deleterious for mechanical properties. Higher cooling rates contrast this phenomenon [32], but it still can be found in thin walled components.

A study by González-Martínez et al. [33] proposed an index (Equation 1.11) to evaluate the risk of the formation of this defect: an important element that is proved to decrease this risk is antimony (Sb). As shown in Figure 1.40, the risk is consistent if the index level is above 7.

$$\Omega_{\text{Si}} = w_{\text{Si}} + 800 * \left(w_{\text{Ce}} * \frac{55}{140.1} - 2w_{\text{Sb}} * \frac{55}{121.8} \right) + 50w_{\text{Mg}} * \frac{55}{24.3} \tag{1.11}$$

Wi represents the wt% of element i, and 55, 140.1, 121.8 and 24.3 are the atomic mass of cast iron, cerium, antimony and magnesium, respectively.
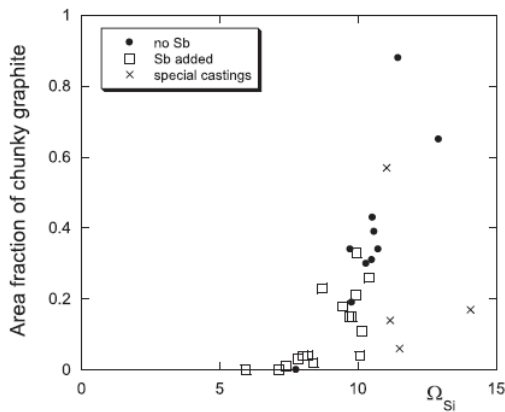

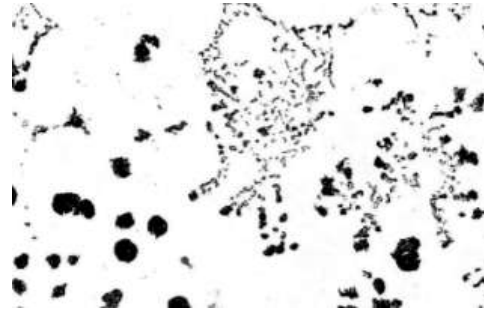Figure 1.40: Correlation between the index Ω_{Si} and the amount of chunky graphite [33]

Figure 1.41: Chunky Graphite [31]

1.3.3 Carbides

One of the biggest challenges for thin walled components is the formation of carbides (cementite formation). Carbides must me strongly avoided because they compromise the mechanical properties of cast iron, leading to embrittlement. The main reason is that high cooling rates generally don't help the formation of a graphitic microstructure, and even if Si enwidens the stable – metastable area, if undercooling is excessive carbides still can form.

Another known factor that lead to the formation of carbides is a low carbon equivalent (CE < 4.30 wt%), where CE is given by the Equation 1.12.

$$CE = w_c + 0.31 * w_{Si} \tag{1.12}$$

Low quality scraps containing carbide promoting elements is also influencing carbides, as well as poor or wrong inoculation (Figure 1.42). However, SSDI has a higher tolerance to pearlite promoters and carbide promoters, so it's possible to use cheaper low-alloyed steel scrap and still obtained a carbide free structure. As analyzed by Riebisch et al. [16], carbide promoting elements such as manganese and niobium are tolerable in SSDI up to 0.5 and 0.2 wt% respectively. Casting designs are also important to keep solidification rate controlled [6].
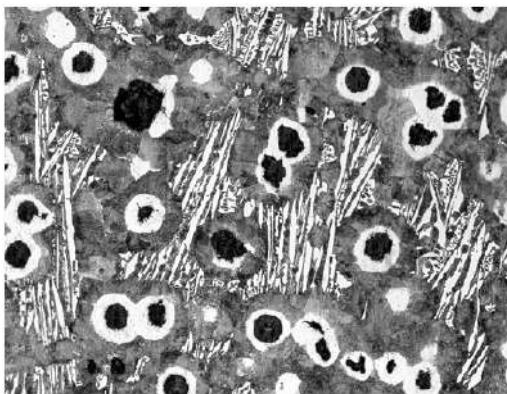

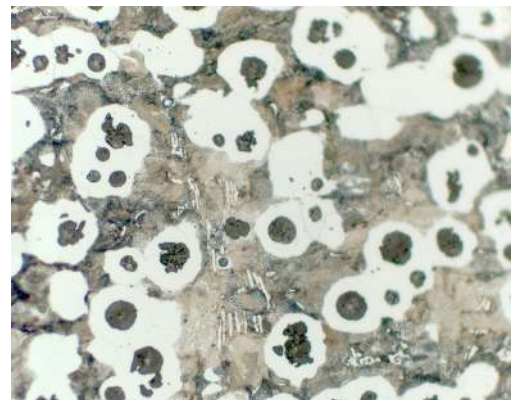Figure 1.42: Carbides caused by poor inoculation [31]

Figure 1.43: Carbides of the GJS-500-14 2.5mm sample

1.3.4 Skin Effect

Skin effect, or Flake Graphite Rim Anomaly (Figure 1.44), is the constitution of a vermicular or flake graphite in the external layer of the casting. It is associated with an excessive content of sulphur that reacts with Mg, that progressively loses its spheroidizing effect. Ruxanda points out that a cause could be a inhomogeneous distribution of Mg in the casting [14], and Sulamet-Ariobimo found out that also a low cooling rate has a role [34]. Skin effect generally appears in sand casting products, and tends to disturb the tensile properties; in general it is considered an acceptable defect, since it can be removed with the finishing processes [6], but in TWDI the low thickness doesn't allow to apply these machining procedures. For this reason, skin effect must be avoided pro-actively, controlling the sulphur content.
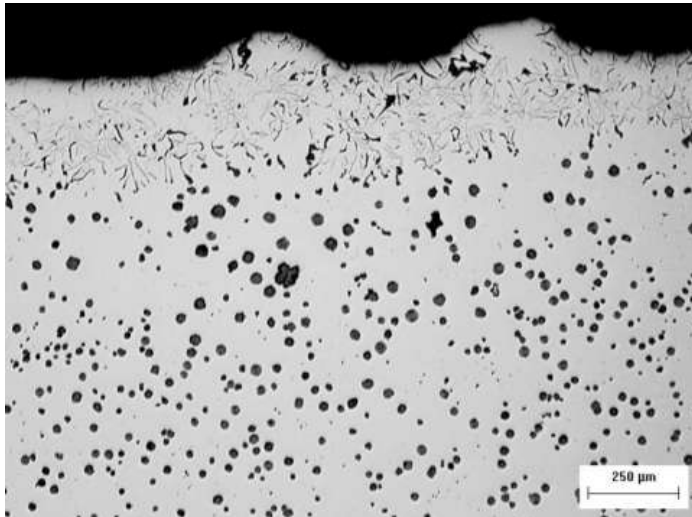

Figure 1.44: Skin Effect or Flake Graphite Ring Anomaly [31]

1.3.5 Shrinkages

Shrinkage is a common defect that appears as small holes or cracks inside the casting (Shrinkage Cavity Defect, Figure 1.45) or as (micro) porosity on the surface (Porosity Shrinkage Defect, Figure 1.46). Premature solidification can also occur and classified as a macro-shrinkage anomaly. Shrinkage can be caused or by problems with the feeding / gating system, or by metallurgical factors like CE, pouring temperature, inoculation or Mg residuals [31]. Mg is necessary to give the spheroidal shape but is also a carbide stabilizer

and it tends to form shrinkages (Figure 1.47), so it must be kept under control, generally never above 0.04 wt%.
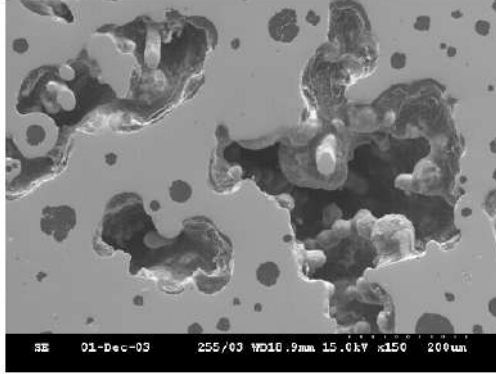

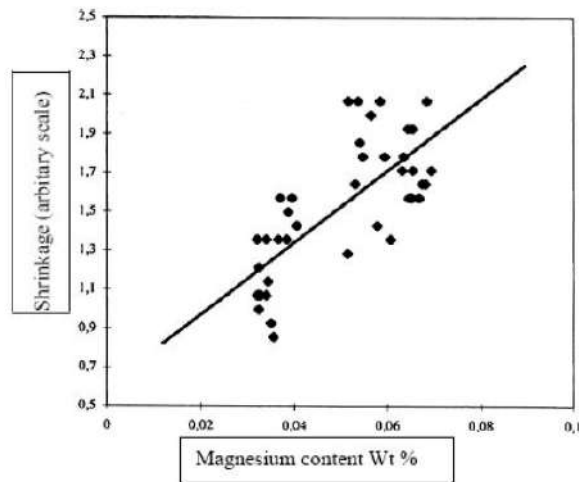Figure 1.45: Micro porosity [31]

Figure 1.46: Macro porosity

Figure 1.47: Mg and porosity correlation [31]

1.3.6   Graphite Floatation

Hypereutectic composition can lead to the formation of primary graphite, that because of their low density tends to float on the austenite matrix that will decompose in ferrite or pearlite. This defect is deleterious for cast iron in general, and it can easily be avoided controlling the CE. An excess of CE leads to what it is shown in Figure 1.48:
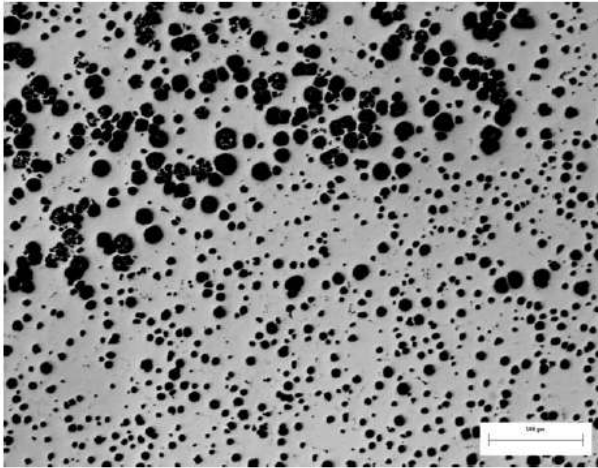
Figure 1.48: Graphite floatation in hypereutectic ductile iron [31]

1.3.7 Inverse Chill

Solidification anomaly that leads to the formation of a carbide phase in the central core of the castings. It can be clearly seen without a microscope (Figure 1.38). It is normally associated with thick and long-time solidification components, but they can also appear in thin part, as reported by Ruxanda [14]. Most likely this white solidification defect (Figure 1.49) is caused by the segregation of oxide and sulfide forming elements in the center of the piece. According to Foundry Lexicon [5], there are many ways to prevent this event, like shortening the solidification time, control the weight percentage of oxygen-affine elements, improving the inoculation (mostly introducing late or stream inoculation), reviewing the Mg treatment.
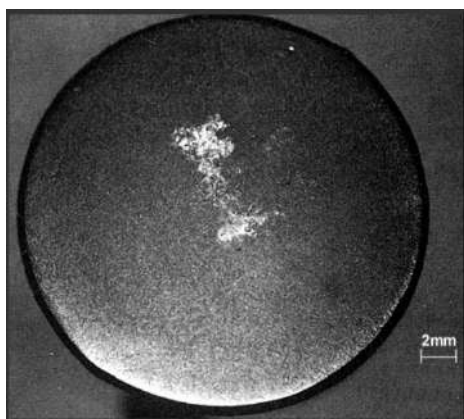

Figure 1.49: Cylindric specimen with clearly visible inverse chill in the core [35]
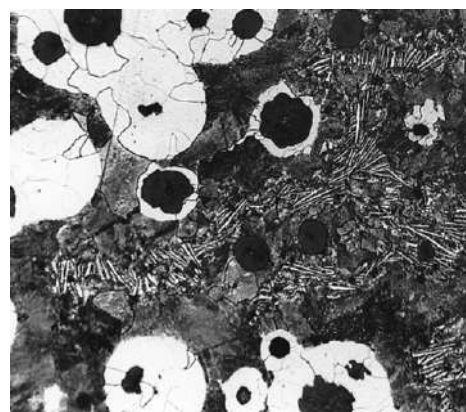

Figure 1.50: Magnification of the core presenting carbides [35]

36

1.3.8 Slag or Sand Inclusion

Errors during the pouring can lead to sand or slag inclusions into the casting, and this causes shrinkage or big solidification anomalies. Slag can be easily removed before pouring, but an excessive content of sulphur or magnesium can form it again during the pouring [36], so it can be avoided controlling these elements and using an appropriate filtering system. Sand inclusion can easily occur if the mold isn't perfectly clean or solidified in some parts. High turbulence is also a possible cause. An effective method to contain these problems are ceramic foam filters (Figure 1.51), because they drop the turbulence of the liquid poured into the mold and they stop external bodies like sand or slag. These kinds of filters were used in the sand molds in this work.

1.3.9 Nodules Alignment

A low CE and/or a not perfect inoculation (not adapted size of the inoculant or a not perfect addition rate) can lead to this clearly visible defect, together with too high pouring temperature and an excessive content of boron and aluminum. The physical cause is that not enough graphite is precipitating [31]. It happens that large dendrites are growing, and the graphite precipitates between the dendrite arms (see Figure 1.52).
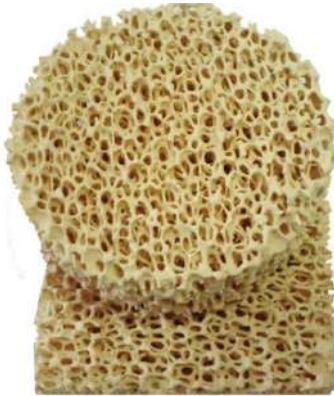

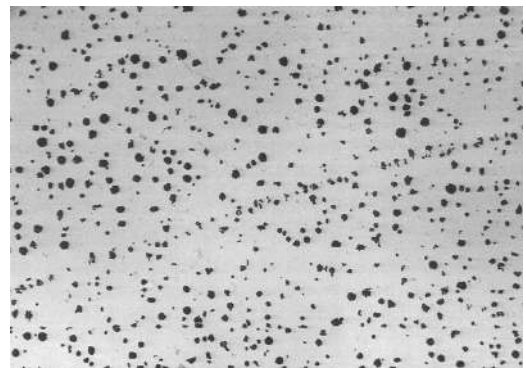*Figure 1.51: Zirconia ceramic foam filters [37]*

Figure 1.52: Nodules alignment [31]

1.4 Thin Wall Ductile Iron

As exposed in the introduction, the developement of thin-walled components is important for their energy saving impact, and for this reason many studies were conductded, both in sand and permanent molds, to better understand the potential of ductile iron. The research were focused either on the optimal casting conditions (for example on the study of the molds and the sprues configurations) and on the carbide-free thickness limits, at different Si contents and with different alloys treatments.

The 2002 Stefanescu's research [7] points out that a carbide free microstructure was obtained with a vertical layout (showed in Figure 1.53) for a series of plates of 2.5, 3.5 and 6 mm, with a Silicon content between 2.47 and 2.75 wt%. The dimension of the plates was 100 x 25 mm (where 25 mm is the heigth). These experiments were realized after some trials with an horizontal layout, where the plates risulted as not completely filled.
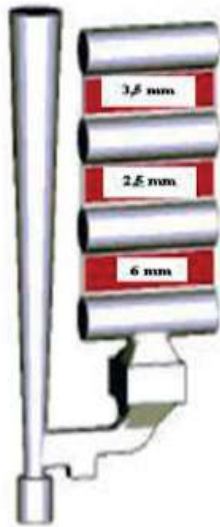

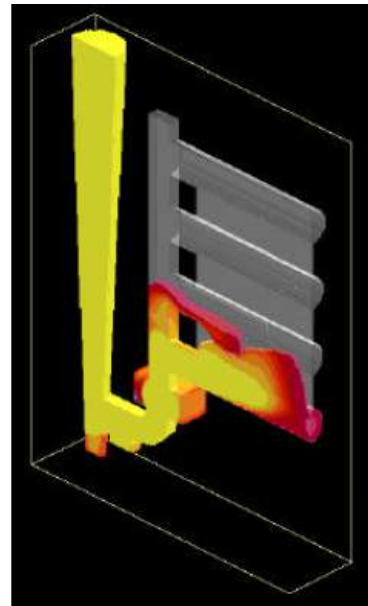Figure 1.53: Stefanescu vertical design

Figure 1.54: Stefanescu vertical design (2)

An horizontal layout was used also by Ahmed [38], and carbide free plates (200 x 100 mm, where 100 mm is the height) up to 2 mm were found working on a thermal insulation material mixed with the Sodium Silicate - CO_2 chemically bonded sand of the sand molds (from 0 to 40 wt% of the mold). It was found that there is a correlation between the amount

of thermal insulating material (74.91 wt% SiO_2,10.64 wt% Al_2O_3, 6.28 wt% Na_2O, 5.06 wt% K_2O, 2.33 wt% Fe_2O_3 and 0.68 wt% CaO). The highest ferrite area percentage was found in the molds with the highest percentage of this element that has the function of controlling the cooling rate.

Sulamet-Ariobimo et others [6] analyzed the literature anout various casting layout, and purpose their own, partially inspired by Stefanescu's one. In this case, plates of 100 x 25 mm, where 25 mm is the height, were found ferritic (the absolutely carbide free microstructure is not specified). The casting layouts used are exposed in Figure 1.55 and 1.56, where this second one consists in the improved version just for the 1 mm plate.
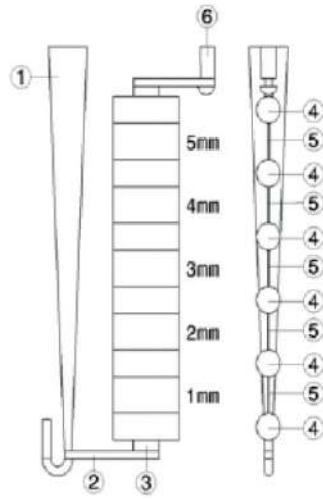
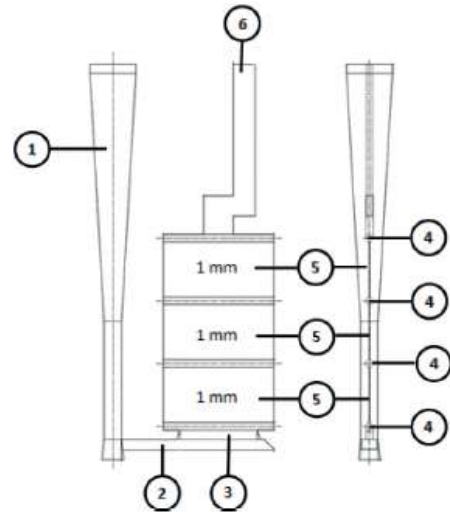

Figure 1.55: Sulamet-Ariobimo design (1)

Figure 1.56: Sulamet-Ariobimo design (2)

Pedersen research of 2006 [19] uses two different layouts, exposed in Figure 1.57 and 1.58 In the horizontal design (chemically bonded sand) results shows how carbides start to appear at 2.8 mm of wall thickness for near eutectic ductile iron, while they also appear at 4.5 mm for hypoeutectic ductile iron. In the vertical green sand layout, carbides are present at 4 mm in some castings, and at 2 mm in others, depending on the Mg treatment used material (Remag 3400, 1.30 wt% in the first, 1.17 wt% in the second). Si content was between 2.03 and 2.70 wt%.
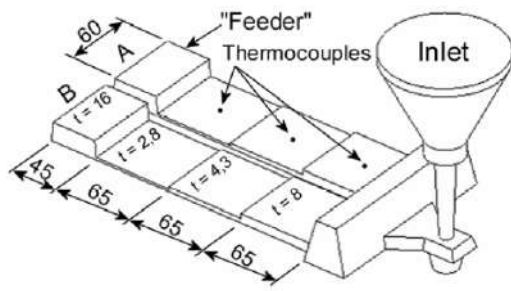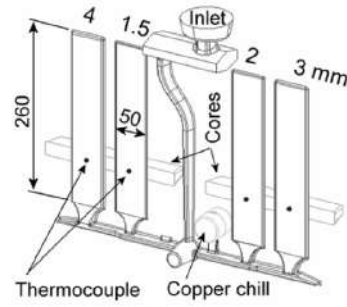
Figure 1.57: Pedersen horizontal design   *Figure 1.58: Pedersen vertical design*

1.5 Permanent Mold Castings

Regarding SSDI, a recent study by Riebisch and others [39] performed in *Gießerei-Institut*, with similar operating conditions. The mold thinnest wall was 10 mm instead of 12 mm, and 12 casting trials were performed at different pre - heating temperatures for the 3 SSDI alloys. Results show that the 10 mm plate always presented primary cementite in every condition, while it was possible to obtain a fully ferritic matrix just for the GJS-600-10 (Si = 4.3 wt%) with a pre heating temperature of 450°C. It was verified how pearlite content decreases with higher per heating mold tempeartures and with higher Si content. The part of the present thesis regarding the permanent mold can be considered a further investigation of the results obtained in this previous work, since the experiments were performed in very similar conditions. The literature review performed in this 2018 project show no other experimental works regarding SSDI permanent mold castings, while several studies about ductile iron were published since early 80's. The article by Kitsudo [40] analyzes the effect of high Silicon wt%, and a as - cast ferritc matrix was obtained with a 30 mm cilinder metal mold and a SIlicon content of 4.7 wt%. Also shrinkage presence was correlated to a lower Carbon Equivalent and an higher Si content.

Similar results were obtained by Khalil-Allafi and Amin-Ahmadi [41] in 2011, that used a metal permanent mold with a 20 mm plate cavity without riser. A carbide and shrinkage free microstructure was obtained at a pre heating temperature of 450°C for a Si content of 2.5 wt% and a CE of 4.45 wt%. An higher Si content rises the nodule count and helps the reduction of the shrinkage volumes and allows to obtain a defect free structure at lower pre heating temperature: for a Si content of 3.3 wt%, this result was possible at 300°.

2 Experiment

2.1 Preliminary Operations

Some necessary operations are described below, from the creation of the molds for the experiment to the optimization of the tools. Figure 2.1 describes the milestones of the process followed during the project.
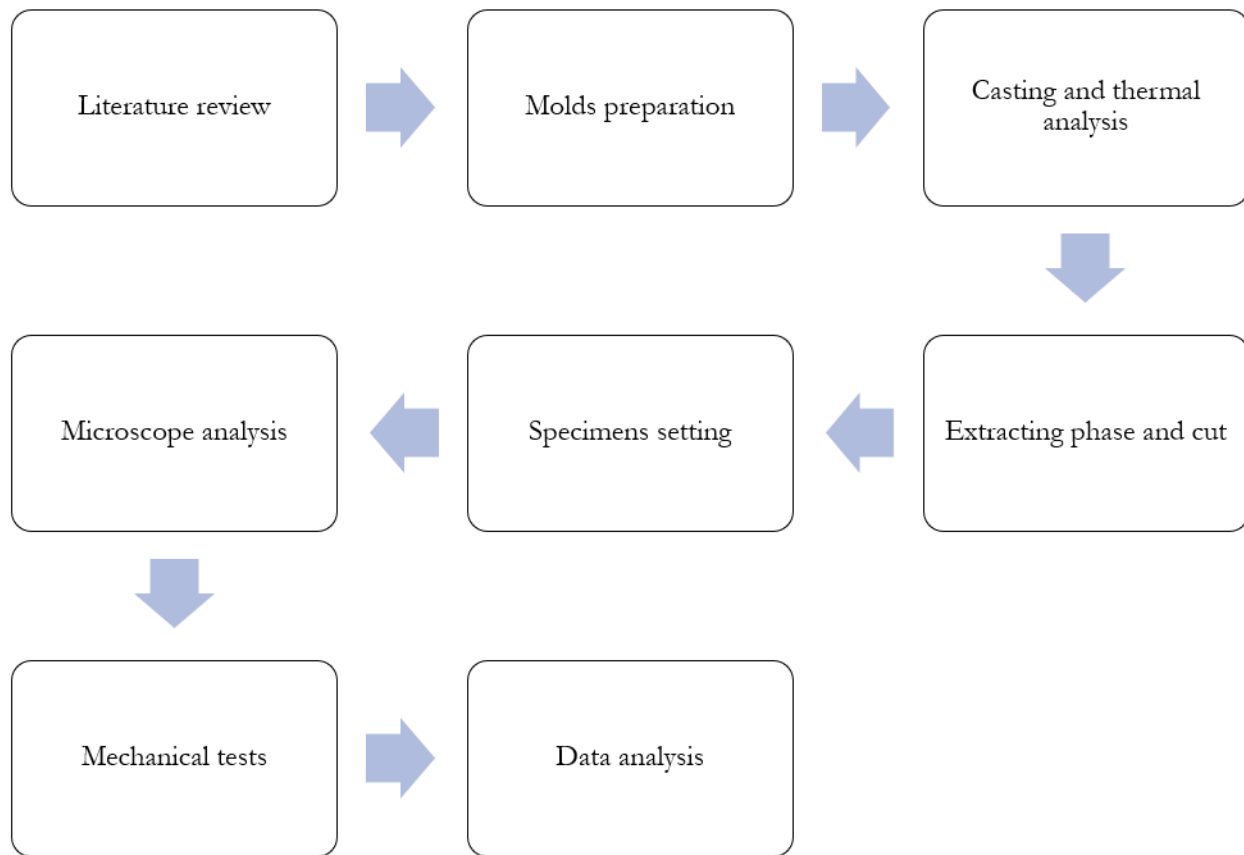

Figure 2.1: Action process of the project

2.1.1 Sand Molds

While the permanent mold for the die casting experiments were already created, it was necessary to build the mold for the thin plate tests (5-4-3-2-1 mm thickness, 15 cm height, 10 cm width, Figure 2.2). The casting of these plates was performed in sand molds, more

specifically the feeding system (including the pouring basin, the raisers and the gas channels) was realized in chemically bonded green sand, while the venues of the plates were realized with the core shooting technique, using a cold box. The sand used was a F32 Quartz Sand (for every mold except for one realized with an H33), chemically bonded with a Kaltharz 7830 resin and an activator, an acid that starts the polymerization of the resin. The ratio of these two elements is function of the velocity of the activator and of the amount of sand to be put into the mixing machine. For 40 kg of F32 sand, 200 g of activator and 560 g of resin must be used. The activator must be put first, after that the mixing machine is already on since a few seconds, and later the resin, both smoothly to enable the correct mixing of the elements and the activation of the process. Afterwards, the standard sand mold creation was followed, first filling the bottom part turned upside-down (drag), then the upper part (cope). It was necessary to wait some hours before removing the pattern from the sand, since it needs to harden completely. Once both sides were ready, they were joined together. The pattern for the sand mold existed already for previous experiments. The following images (Figure 2.7, 2.8, 2.9, 2.10, 2.11, 2.12) show some steps of the preparation on the sand molds.

2.1.2 Core Shooting

The core shooting in cold box technique was used to create the cavity for the plates (see Figure 2.3). Core shooting uses quartz sand hardened with an ammine fog into a cold box. The temperature of the sand should never be over 30°C. This adjustment was needed for the shape of the plates: indeed, the thickness of the plates doesn't allow to entirely build the mold in green sand, since especially the thinnest (1-2 mm) wouldn't be able to stand the high pouring temperature, that starts from 1350°C. The pattern for the core shooting were realized inside the mechanical laboratories of the foundry institute (Gießerei-Institut).
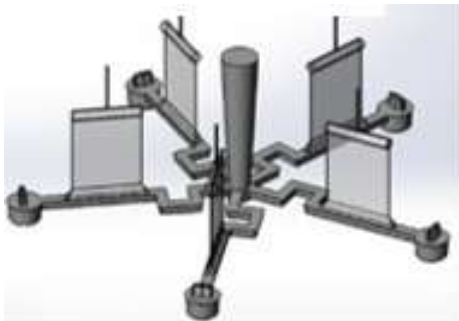

Figure 2.2: Sand Mold Geometry

Figure 2.3: Core Shooted Plate Box

42

2.1.3 Permanent Mold

The existing permanent mold (30-20-12 mm plates, Figure 2.4) was pre-heated at 150°C, then coated (with Solitec CC 407 from ASK Chemicals, see Figure 2.5), and heated again to reach an ideal temperature of 350°C at the moment of the casting. The trials were performed heating up the permanent mold at 370°C. The temperature drop that occured was around 20-40°C, due to the time needed for the inoculation and the Mg treatment.

Before these operations, thermocouples were positioned into specific holes created for them, precisely in the middle of the plates. During the castings, before the Mg treatment and inoculation, the mold halves were removed from the hoven and screwed together. The evolution of the temperatures was recorded with the PicoLog6 Software.
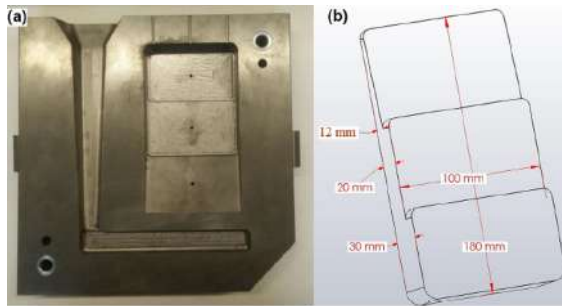
Figure 2.4: Permanent Mold Geometry

Figure 2.5: Coated Permanent Mold

2.1.4 Thermocouples

It was necessary to substitute the case of a standard Type K thermocouple from a plastic one to a ceramic one, because they had to resist to high temperatures. The Type K thermocouple is a Cr-Ni alloy. The thermocouples were placed in the permanent mold to record the temperature drop on the different steps of the mold.

Figure 2.6: Type K thermocouple

Figure 2.7: Drag before filling

Figure 2.8: Drag after filling

Figure 2.9: Cope before filling

Figure 2.10: Cope after filling

Figure 2.11: Joined parts before filling

Figure 2.12: Joined parts after filling

2.1.5 Castings Composition

Table 2.1: Material composition of the melts

Material	Mass [kg]	Notes
GJS-400-15		
Recycled Iron +GF+	35.5	
Pure Iron	8.75	
Recarburizer	0.360	
VL63O	0.585	Mg treatment
SMW 605	0.112	Inoculation
GJS-450-18		
Recycled Iron +GF+	43.0	
Pure Iron	1.0	
FeSi75	0.23	Max 1.5 wt% of Al
VL63O	0.585	
SMW 605	0.112	
GJS-500-14		
Recycled Iron +GF+	40.6	
Pure Iron	3.0	
FeSi75	0.66	
VL63O	0.585	
SMW 605	0.112	
GJS-600-10		
Recycled Iron +GF+	38.7	
Pure Iron	4.5	
FeSi75	1.0	
VL63O	0.585	
SMW 605	0.112	

Table 2.2: *VL63O chemical composition. Missing wt% is Fe [42]*

Element	Wt%
Mg	6.0-6.5
Ca	1.9
Si	45

Table 2.3: *SMW 605 chemical composition. Missing wt% is Fe [43]*

Element	Wt%
Si	62-68
Al	<1.0
Ca	1.8-2.4
Bi	0.8-1.2
Se	0.8-1.2

2.2   Experiment Procedure

2.2.1   Melting Procedure

The melts were performed into the *Gießerei-Institut* foundry hall, with a 50 kg capacity induction furnace. Only the first casting had a different procedure, since the C content had to be adjusted with a Recarburizer and checked with a single use specimen. All the other castings were performed adding the FeSi75 in the beginning, together with the recycled iron and the pure iron. The Mg treatment with the VL36O (see Table 2.2), necessary for the spheroidization, was performed with the plunging bell technique (Figure 2.13, Figure 2.14), immediately before the inoculation with the SMW 605 (see Table 2.3). The plunging bell was specifically coated with Necropal 3, a water based coating from Hüttenes Albertus Chemische Werke GmbH and dried before the casting. The melt was then poured first into a proper round shape specimen for the spectrometer chemical analysis, then inside two disposable CCA (Cooling Curve Analysis) samples for the thermal analysis. The first one (QC 4010, Figure 2.15) to measure the Carbon Equivalent Liquidus (an improved CE formula for the thermal analysis purposed by the disposable CCA test cups supplier) and the undercooling, the second one (QT 4012, Figure 2.16) containing Tellurium and Sulphur to

determine C and Si wt%. Adding Te and S is necessary to extend the measurement range of equivalent carbon an to obtain a white solidification, so that an easy readable solidus arrest necessary for C and Si is displayed [44]. The crucible was taken out of the induction furnace at a temperature around 1550°C, since the Mg treatment and the inoculation time were lowering the pouring temperature. All the pouring temperatures of the melts were between 1350 and 1395°C.
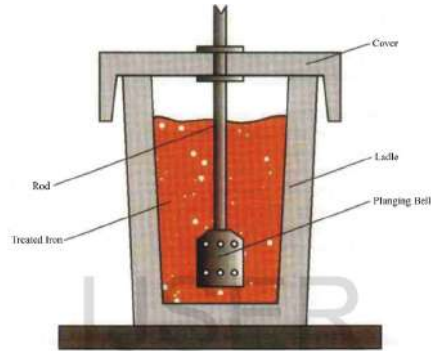

Figure 2.13: Plunging Bell Technique [45]

Figure 2.14: Plunging Bell
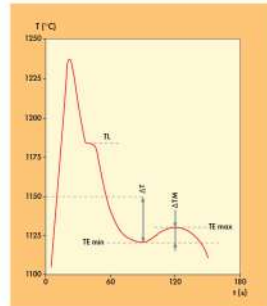
Figure 2.15: QC 4010 CCA Sample [44]
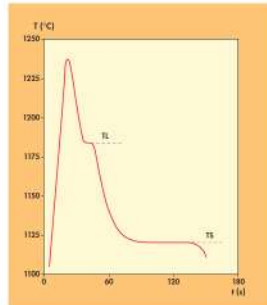
Figure 2.16: QC 4012 CCA Sample [44]

2.2.2 Spectrometer Analysis

A specific sample for the spectrometer analysis was casted in every trial. The machine was Spectro Spectromax (with CCD optics, 2002), together with the software Spark Analyzer. It was necessary to charge the argon gas about 3 hours before the analysis. A further analysis has been made by an external laboratory to compare the results.

2.2.3 Metallographic Analysis: Preparation of the Samples

The plates have been cut with a grinder to separate them from the pouring basin. After that, a *ATM Brillant 230* machine has been used to obtain a precision cut on the central zone of the plate. The result was a small squared shape sample. The next step has been the embedding: the samples were put in a specific cylindric shape form, that has been fulfilled with a Methyl-methacryalat liquid (*KEM 35 Flüssigkeit*) and its correspondent powder to obtain a solid sample necessary for the following steps (see Figure 2.18). Once the samples were embedded, the grinding and the polishing were performed with a *Pollermaschine Saphir*. The grinding was performed using different plates with decreasing grit power (80-120-320-500-1000). The polishing operation specifically was realized in 3 steps with a diamond polish (size 9-3-2.5 μm). If these operations were realized a day before using the digital light Microscope, it was necessary to repeat the last polishing passage with the thinnest plate.
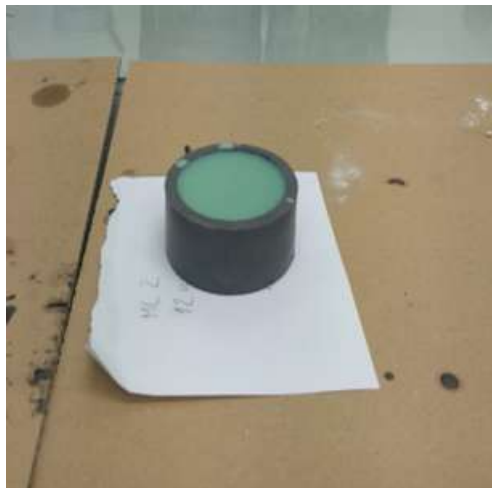
Figure 2.17: Embedding procedure

Figure 2.18: Embedded Sample

2.2.4   Digital Light Microscope Analysis

The microscope analysis was performed with a *Zeiss Axiophot* microscope, using the software Axiovision. For each sample, using a 200x magnification, 10 photos were taken (5 before and 5 after etching). The photos after the etching enhance the pearlite and the ferrite fractions, while the photos before are useful to understand the nodule count, the graphite classification and the presence of some defects.

2.2.5   Mechanical Tests

Tensile Strength R_m, Yield Strength ($R_{p0.2}$) and Elongation (A_5), were calculated on each carbide free sample up to 5 mm, to confirm the international standards exposed in chapter 1.2. Hardness tests were not performed since it's already well known that hardness has a linear correlation with the Si content, due to its strengthening, but also embrittling, effect on the matrix. Test were performed into the mechanical laboratories of the *Gießerei-Institut*.

3 Results

The castig trials were performed in two different phases, with the second one as a consequence of the results of the first; regarding the sand molds, the goal was to find the transaction thicknesses that allow to obtain a carbide free microstructure for each silicon content. To reach this result the first round of castings was performed with standard measures (1, 2, 3, 4 and 5 mm), while the second analyzed intermediate measure (2.5, 3.5, etc. mm), since every composition have a different behaviour and a different transaction point to a carbide free structure due to silicon content. The plates analyzed in the second round of castings obviously were less, because the plates of interest were, as just said, the carbide free transaction thickness and, in some alloys, the transaction point an almost ferritic structure to a fully ferritic structure. On the other hand, the variable for the permanent mold samples was the pre-heating temperature of the mold: also in this case the temperature was changed prograssively to find out the carbide free structure transaction point for each thickness. There was no fulfillment issue in the permanent mold castings.

3.1 Alloys chemical composition

Table 3.1: Chemical composition of the alloys

	C	Si	Mn	Mg	P	S
GJS-400-15 (1)	3.53	2.34	0.110	0.036	0.021	0.005
GJS-450-18 (1)	3.30	3.14	0.112	0.0385	0.023	0.004
GJS-500-14 (1)	3.04	3.81	0.129	0.0407	0.022	0.0038
GJS-600-10 (1)	2.95	4.32	0.130	0.0398	0.021	0.0033

Table 3.2: Chemical composition of the alloys (2)

	C	Si	Mn	Mg	P	S
GJS-400-15 (2)	3.50	2.44	0.139	0.0333	0.0153	0.0066
GJS-450-18 (2)	3.80	3.27	0.164	0.446	0.0264	0.004
GJS-500-14 (2)	2.79	3.85	0.141	0.0441	0.024	0.0043
GJS-600-10 (2)	3.18	4.35	0.153	0.0342	0.0163	0.0082

3.2 Fulfillment of the Plates

Table 3.3: Vertical fulfillment of the Sand Mold Plates - First casting

	GJS-400-10	GJS-450-18	GJS-500-14	GJS-600-10
1 mm	6.5 / 15 cm	8.7 / 15 cm	10.5 / 15 cm	7.5 / 15 cm
2 mm	11 / 15 cm	12.5 / 15 cm	15 / 15 cm	14 / 15 cm
3 mm	15 / 15 cm	15 / 15 cm	15 / 15 cm	15 / 15 cm
4 mm	15 / 15 cm	15 / 15 cm	15 / 15 cm	15 / 15 cm
5 mm	15 / 15 cm	15 / 15 cm	15 / 15 cm	15 / 15 cm

The results of the first round of castings determined the thicknesses of the plates of the second round of castings: except for the GJS-600-10 the 1 mm and the 2 mm plates were abandoned since they appeared completely white solified.

Table 3.4: Vertical fulfillment of the Sand Mold Plates - Second casting

	GJS-400-10	GJS-450-18	GJS-500-14	GJS-600-10
2 mm	-	-	-	14 / 15 cm
2.5 mm	-	-	15 / 15 cm	15 / 15 cm
3.5 mm	-	15 / 15 cm	-	15 / 15 cm *
4.5 mm	15 / 15 cm	-	15 / 15 cm *	-
6 mm	15 / 15 cm	15 / 15 cm	-	-
7 mm	15 / 15 cm	-	-	-
7.5 mm	15 / 15 cm	-	-	-

A second review of the real wall thicknesses of the samples performed during the tensile tests revealed that the 4.5 mm and the 3.5 mm plate of the GJS-500-14 and of the GJS-600-10, respectively, resulted slightly thicker. Even considering that the casting skin makes the plates thicker, for these two samples the error interval has to be considered excessive. For this reason, these samples can't be taken in count for the analysis.

3.3 Sand Mold Plates Microstructures

The metallographic analysis was necessary to determine the nodularity of the samples and to classify the graphite particles in the categories exposed in paragraph 1.1.1, and to determine the ferrite and pearlite area fraction in each sample. For each alloy, the first casting was realized with 5 plates with a thickness between 1 and 5 mm, and the second casting with a variable number of plates due to determine the fully ferritic and the carbide free microstructures.

As explained in paragraph 2.2.4, the software Axiovision was used to take the following pictures (Figure 3.1), just a few moments after the polishing or the etching due to keep a clear image.

The pictures on the left side are samples after polishing, the pictures on the right side are samples after etching.
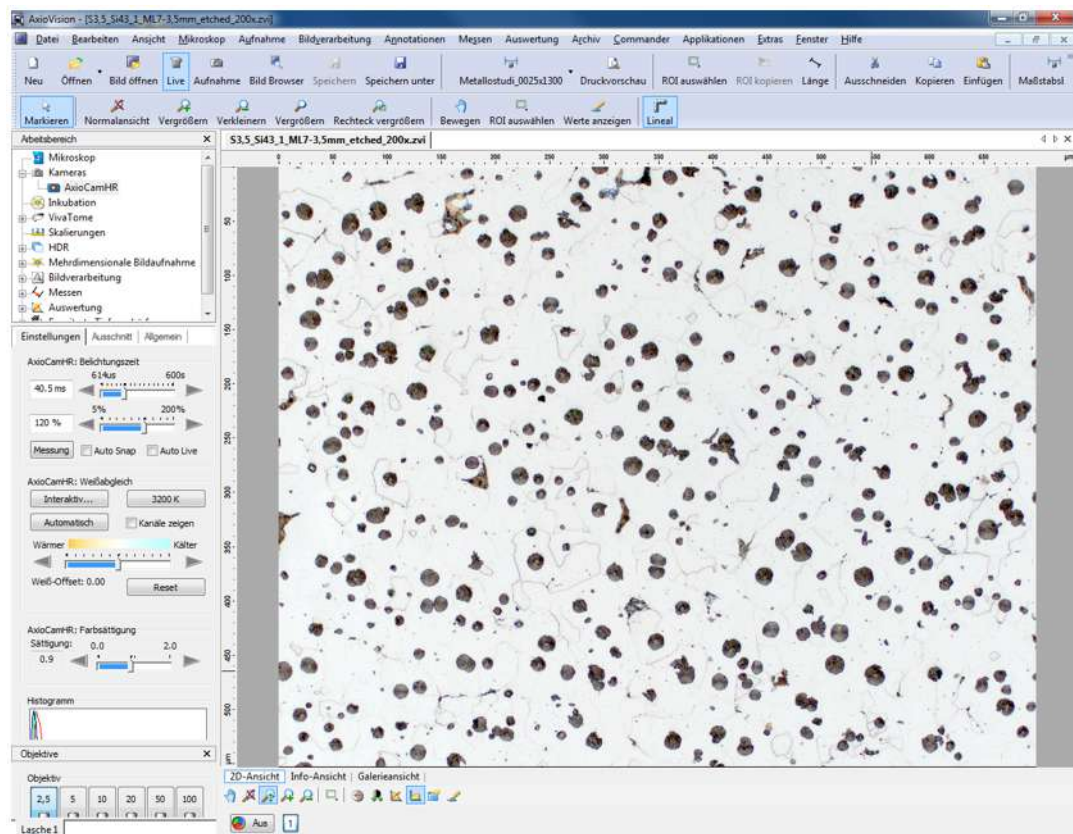
Figure 3.1: AxioVision software

3.3.1 GJS-400-15 - Sand Mold
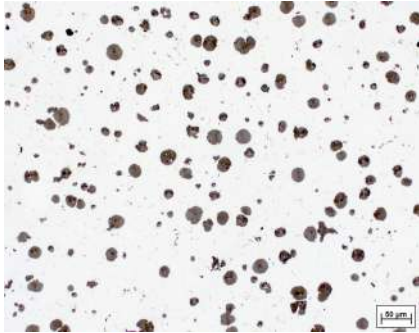
Figure 3.2: GJS-400-15, 5mm-polished
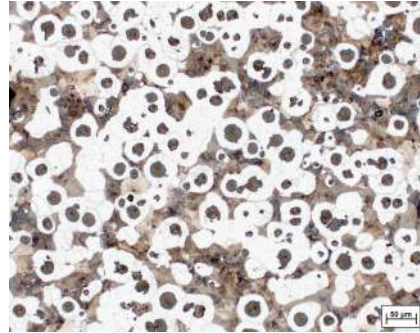

Figure 3.3: GJS-400-15, 5mm-etched

Figure 3.4: GJS-400-15, 4mm-polished
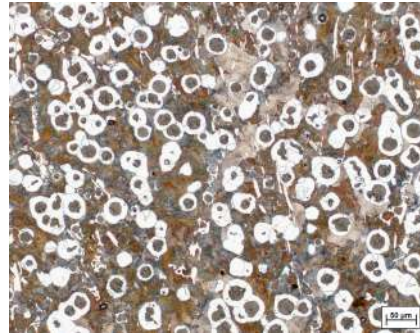

Figure 3.5: GJS-400-15, 4mm-etched

Figure 3.6: GJS-400-15, 3mm-polished

Figure 3.7: GJS-400-15, 3mm-etched

Figure 3.8: GJS-400-15, 2mm-polished

Figure 3.9: GJS-400-15, 2mm-etched

Figure 3.10: GJS-400-15, 1mm-polished

Figure 3.11: GJS-400-15, 1mm-etched

The optimal carbide free structure has to be found between 4 and 5 mm, so a 4.5 mm plate was used. The fully ferritic matrix hasn't been reached despite a progression of 3 thicker plates of 6, 7 and 7.5 mm.
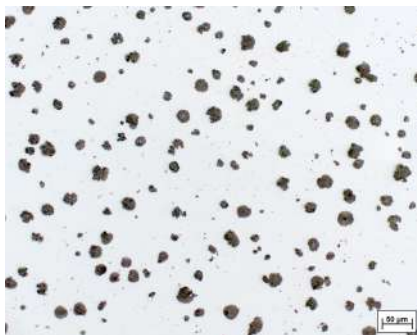
Figure 3.12: GJS-400-15, 7.5 mm-polished
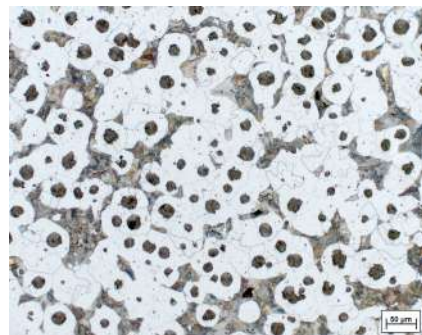
Figure 3.13: GJS-400-15, 7.5 mm-etched

Figure 3.14: GJS-400-15, 7 mm-polished
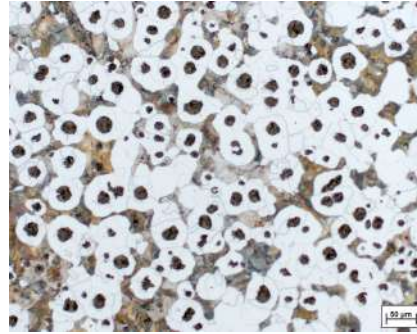
Figure 3.15: GJS-400-15, 7 mm-etched

Figure 3.16: GJS-400-15, 6 mm-polished
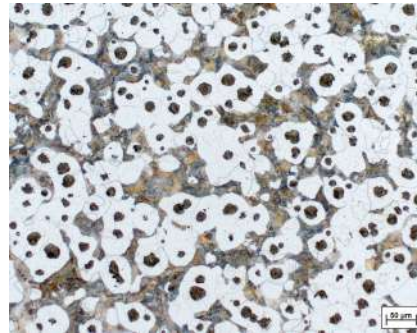
Figure 3.17: GJS-400-15, 6 mm-etched

Figure 3.18: GJS-400-15, 4.5 mm-polished
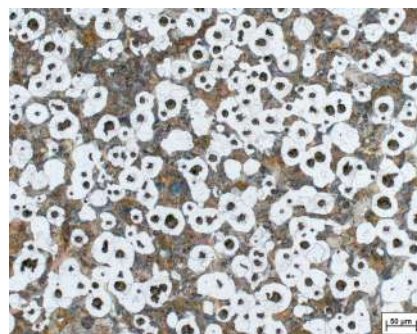
Figure 3.19: GJS-400-15, 4,5 mm-etched
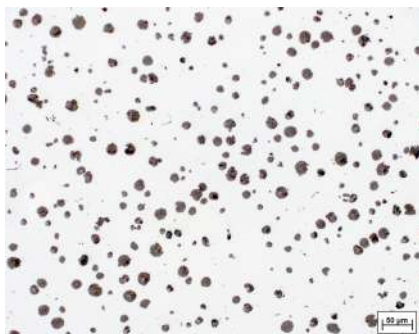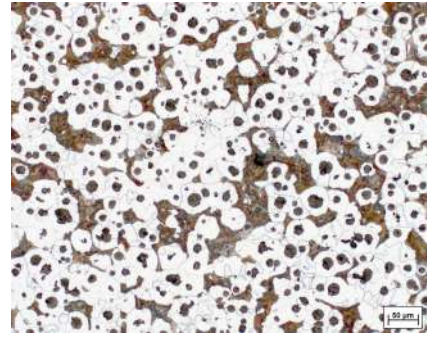
3.3.2 GJS-450-18 - Sand Mold
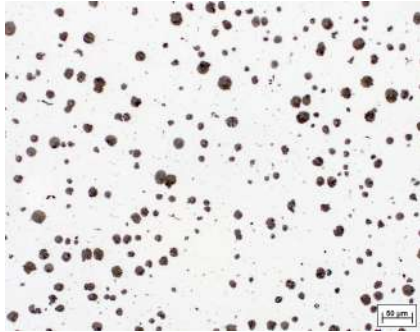
Figure 3.20: GJS-450-18, 5mm-polished
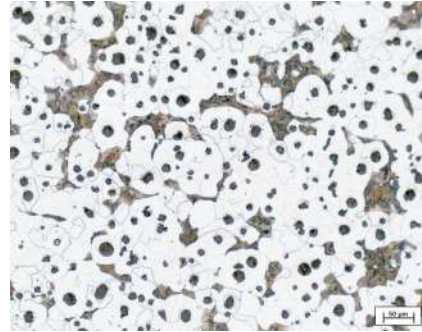
Figure 3.21: GJS-450-18, 5mm-etched
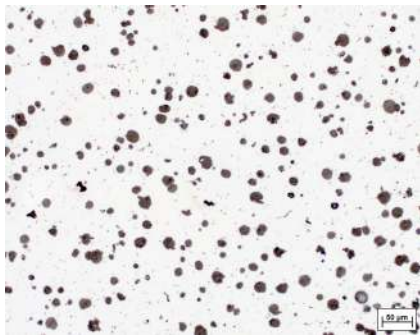
Figure 3.22: GJS-450-18, 4mm-polished
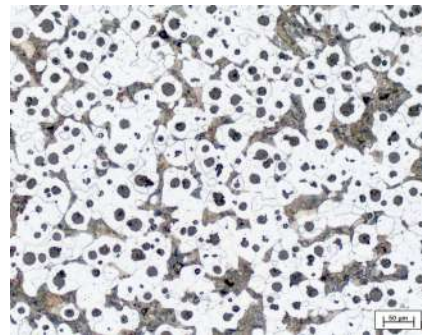
Figure 3.23: GJS-450-18, 4mm-etched
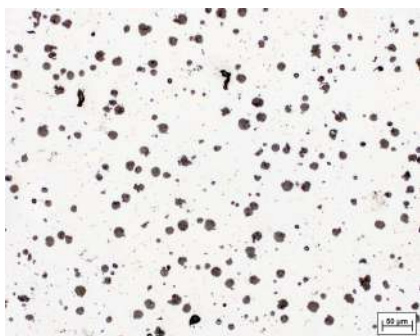
Figure 3.24: GJS-450-18, 3mm-polished
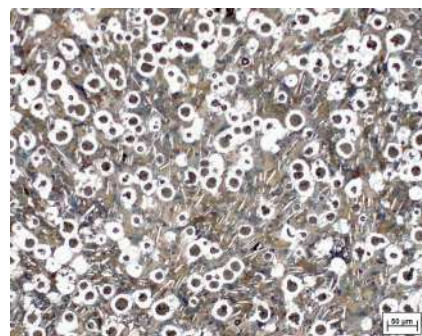
Figure 3.25: GJS-450-18, 3mm-etched
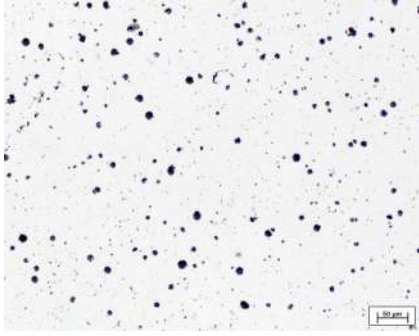
Figure 3.26: GJS-450-18, 2mm-polished

Figure 3.27: GJS-450-18, 2mm-etched
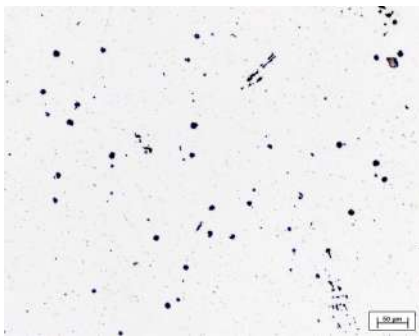
Figure 3.28: GJS-450-18, 1mm-polished

Figure 3.29: GJS-450-18, 1mm-etched

For the GJS-450-14 it was found that the 3mm plates presented carbides, and that the 5mm plate wasn't completely ferritic. Consequently the second casting was performed with a 3,5mm and a 6mm plate. The 3,5mm resulted carbide free, while the 6mm still can't be considered fully ferritic.

Figure 3.30: GJS-450-18, 6mm-polished
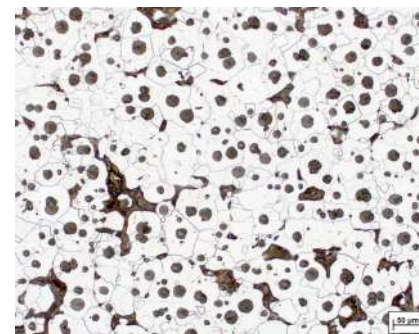
Figure 3.31: GJS-450-18, 6mm-etched

58
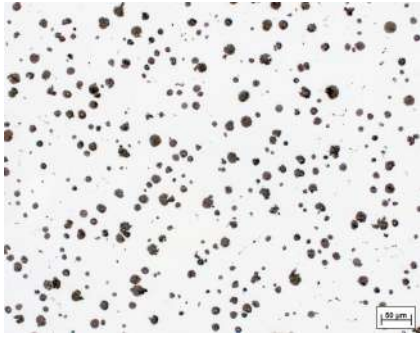
Figure 3.32: GJS-450-18, 3,5mm-polished

Figure 3.33: GJS-450-18, 3,5mm-etched

3.3.3 GJS-500-14 - Sand Mold
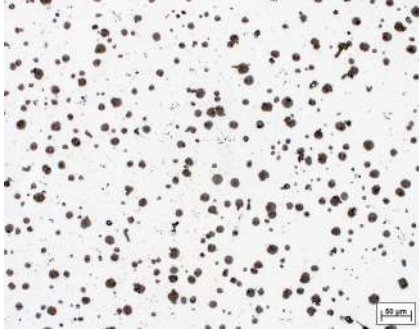
Figure 3.34: GJS-500-14, 5mm-polished
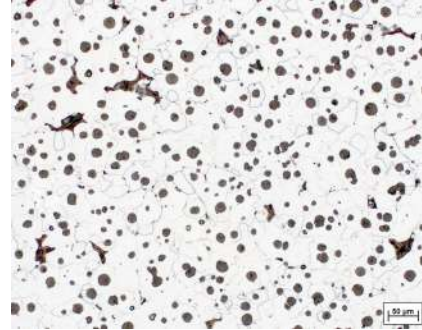

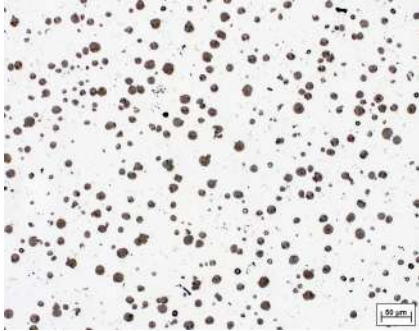Figure 3.35: GJS-500-14, 5mm-etched

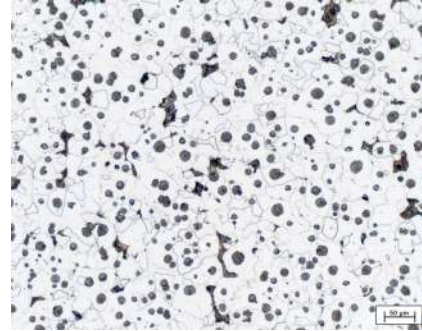Figure 3.36: GJS-500-14, 4mm-polished

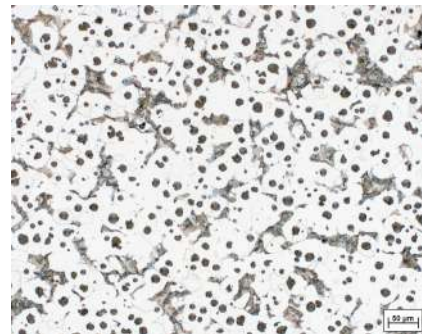Figure 3.37: GJS-500-14, 4mm-etched

Figure 3.38: GJS-500-14, 3mm-polished

Figure 3.39: GJS-500-14, 3mm-etched
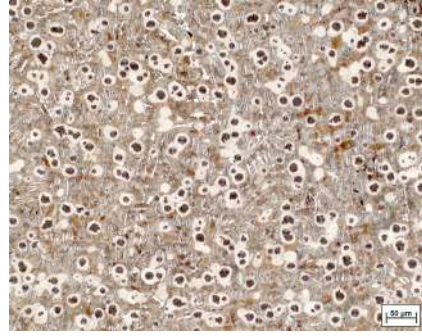
Figure 3.40: GJS-500-14, 2mm-polished

Figure 3.41: GJS-500-14, 2mm-etched
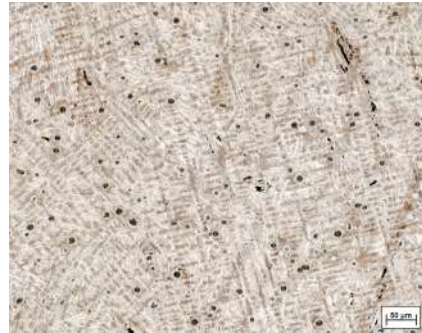

Figure 3.42: GJS-500-14, 1mm-polished

Figure 3.43: GJS-500-14, 1mm-etched

The GJS-500-14 presented a carbide-free microstructure at 3mm and a fully ferritic matrix at 5mm. Although the 2.5 mm plate is not white solified, still presents carbides so the optimal solution is between 2.5 and 3 mm. The fully ferritic matrix can be found, in the conditions of this work, between 4 and 5 mm. The contrast analysis of the images actually revealed at pearlite content of 5.3 wt% on the 4 mm plate.
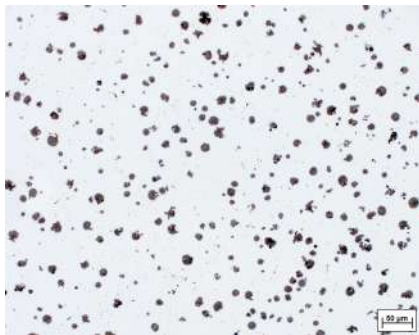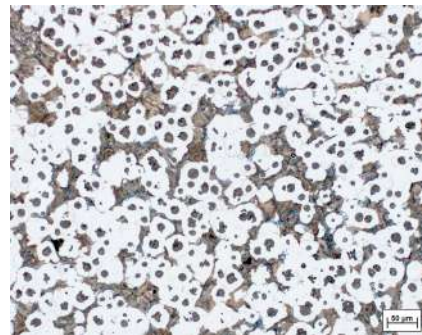

Figure 3.44: GJS-500-14, 2.5mm-polished

Figure 3.45: GJS-500-14, 2.5mm-etched

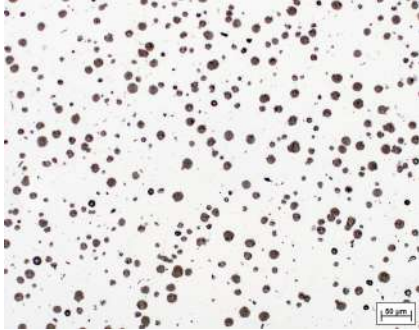### 3.3.4   GJS-600-10 - Sand Mold

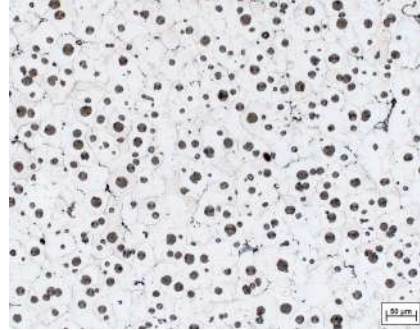*Figure 3.46: GJS-600-10, 5mm-polished*

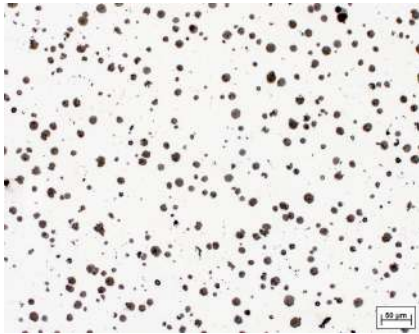*Figure 3.47: GJS-600-10, 5mm-etched*

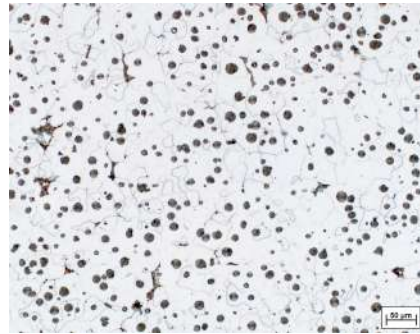*Figure 3.48: GJS-600-10, 4mm-polished*

Figure 3.49: GJS-600-10, 4mm-etched

Figure 3.50: GJS-600-10, 3mm-polished
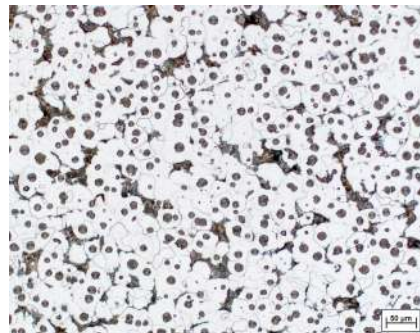
Figure 3.51: GJS-600-10, 3mm-etched
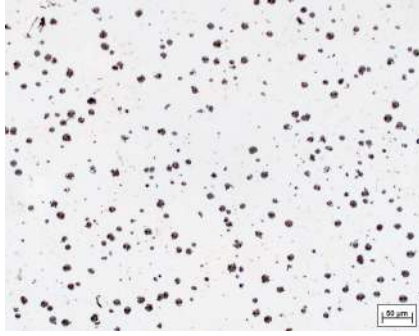
Figure 3.52: GJS-600-10, 2mm-polished
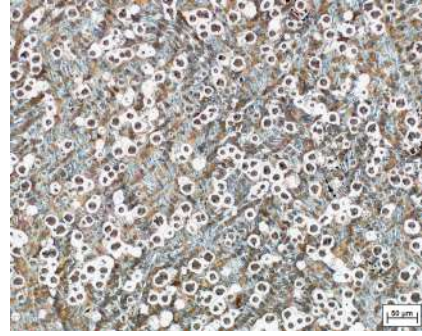
Figure 3.53: GJS-600-10, 2mm-etched

Figure 3.54: GJS-600-10, 1mm-polished

Figure 3.55: GJS-600-10, 1mm-etched

The 3 mm and the 4 mm plate in the first casting had a pearlite content of 15.44 wt% and 2.14 wt%, respectively, so the 5 wt% pearlite limit can be found, in the conditions of this work, between these two values. The the 2.5 mm presented a small amount of carbides, still in a fewer percentage than the GJS-500-14. The first carbide free plate found is consequently the 3 mm.

Figure 3.56: GJS-600-10, 2,5mm-polished
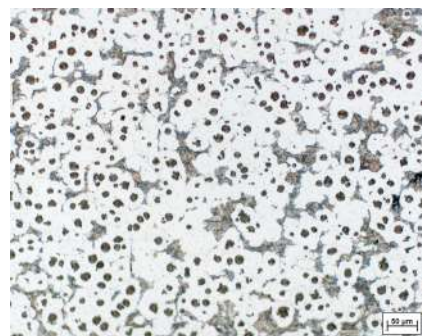
Figure 3.57: GJS-600-10, 2,5mm-etched

63

3.4 Permanent Mold Plates Microstructures

3.4.1 GJS-400-15 - Permanent Mold
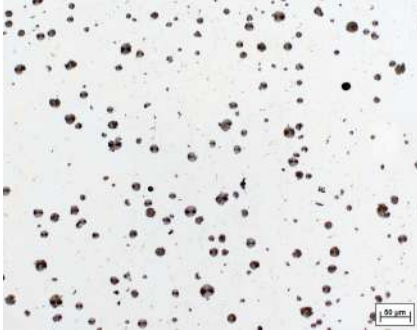
Figure 3.58: GJS-400-15, 30mm-polished

Figure 3.59: GJS-400-15, 30mm-etched

Figure 3.60: GJS-400-15, 20mm-polished
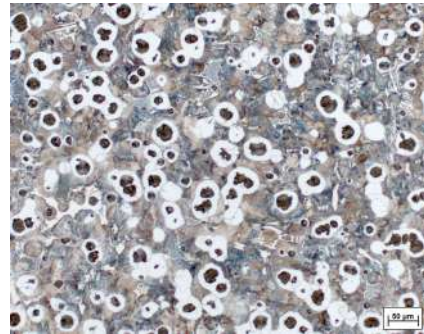
Figure 3.61: GJS-400-15, 20mm-etched
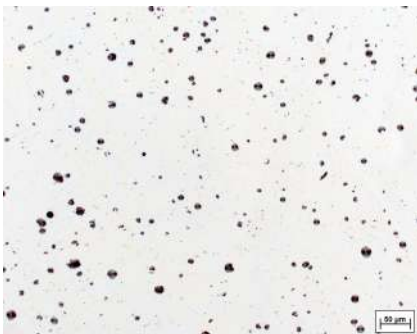
Figure 3.62: GJS-400-15, 12mm-polished
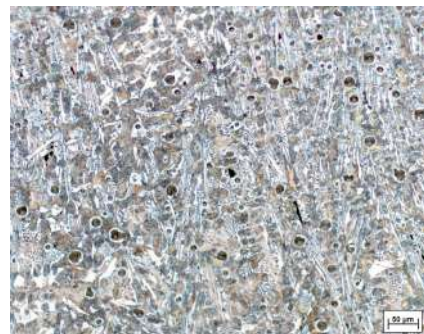
Figure 3.63: GJS-400-15, 20mm-etched

Every step presented carbides; a higher pre heating temperature is necessary.

3.4.2 GJS-450-18 - Permanent Mold

Figure 3.64: GJS-450-18, 30mm-polished
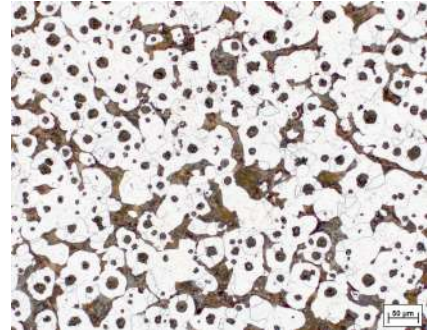
Figure 3.65: GJS-450-18, 30mm-etched
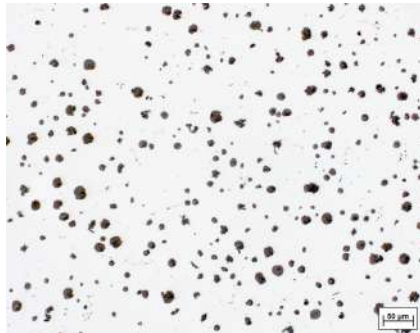
Figure 3.66: GJS-450-18, 20mm-polished
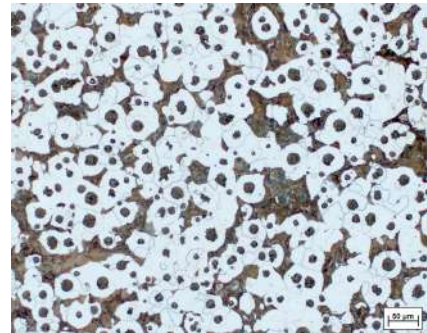
Figure 3.67: GJS-450-18, 20mm-etched
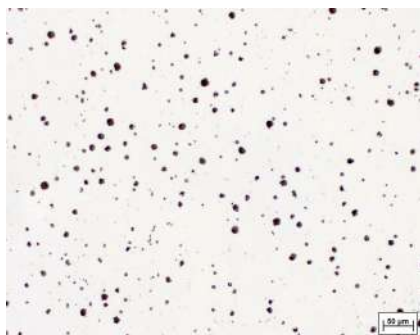
Figure 3.68: GJS-450-18, 12mm-polished
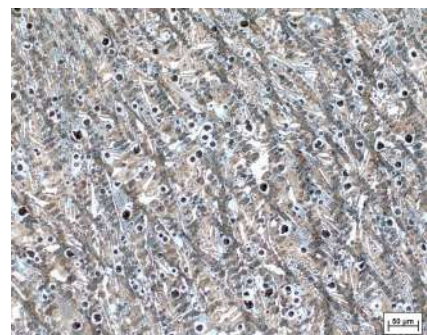
Figure 3.69: GJS-450-18, 12mm-etched

Despite the 20 and the 30mm present a carbide-free microstructure in the core zone, they are both characterized by carbides around the walls of the molds. The high temperature of the mold allowed indeed the formation of ferrite through diffusion, and expecially in the 30mm plate, carbides and ferrite grew together, as it can be seen in Figure 3.70 and 3.71:
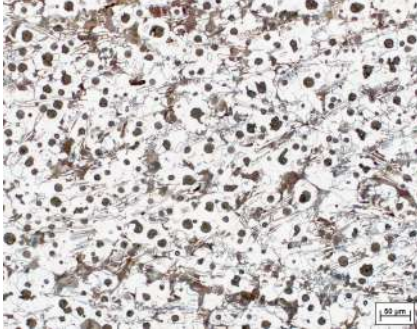
Figure 3.70: Carbides and ferrite in the 30mm plate.
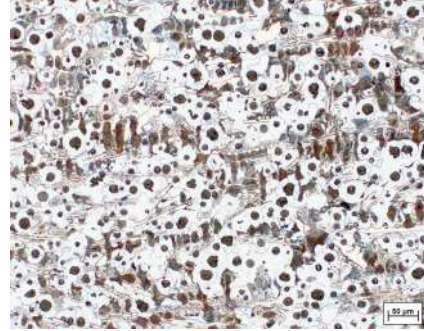
Figure 3.71: Carbides and ferrite in the 20mm plate.

3.4.3 GJS-500-14 - Permanent Mold

Figure 3.72: GJS-500-14, 30mm-polished
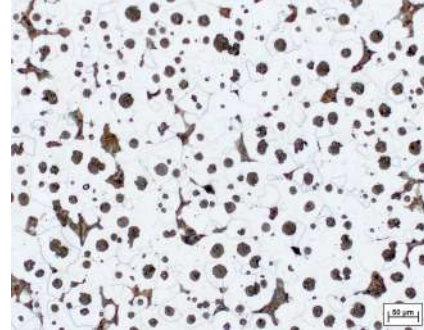
Figure 3.73: GJS-500-14, 30mm-etched

Figure 3.74: GJS-500-14, 20mm-polished
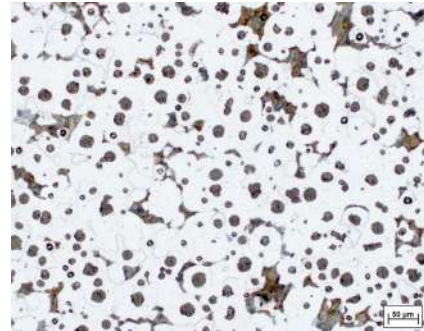
Figure 3.75: GJS-500-14, 20mm-etched

Figure 3.76: GJS-500-14, 12mm-polished
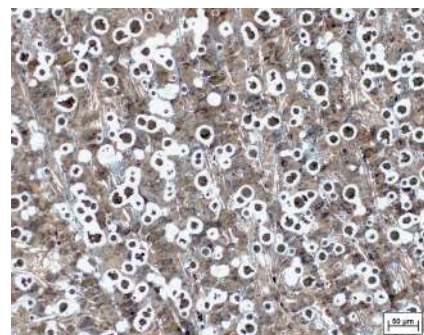
Figure 3.77: GJS-500-14, 12mm-etched

Carbides are present just in the 12 mm step, while 20 mm and 30 mm result carbide free and with a very low pearlite content in the core zone.

3.4.4 GJS-600-10 - Permanent Mold

Figure 3.78: GJS-600-10, 30mm-polished
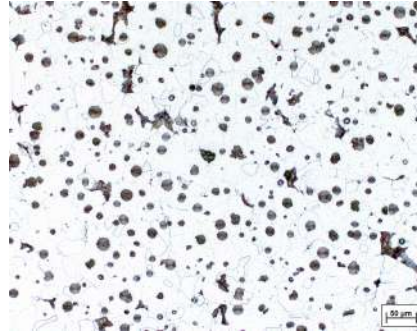
Figure 3.79: GJS-600-10, 30mm-etched
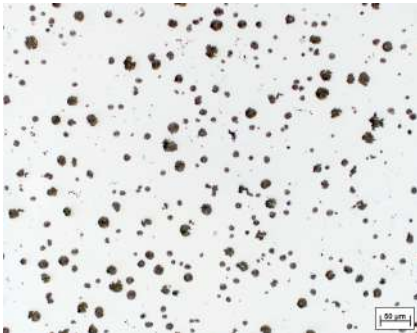
*Figure 3.80: GJS-600-10, 20mm-polished*
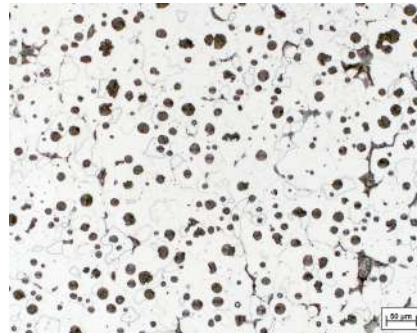
*Figure 3.81: GJS-600-10, 20mm-etched*


Figure 3.82: GJS-600-10, 12mm-polished
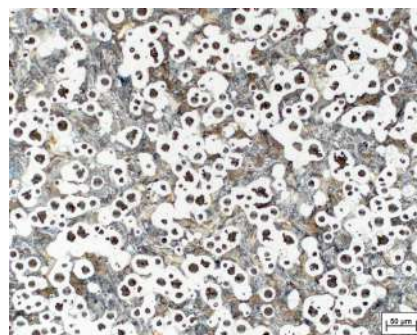
Figure 3.83: GJS-600-10, 12mm-etched

20 and 30 mm steps result fully ferritic, while in the 12 mm step carbides are still present.

3.5 Thermal Analysis

The thermal analysis with the disposable CCA test cups can give many results about the key temperatures and primary indications on many aspects such as the success of the inoculation process, the presence of carbides, and the content of some elements. Points such as Liquidus or Metastable Eutectic can be found easily looking at the derivates curve, as they appear as minimum or maximum in specific points. Finding the Eutectic Metastable is helpful if compared with the thermal analysis of the permanent molds, since gives a clear indication of how the solidification process went. In general, also finding that the End of solidification point is above the Eutectic Metastable means that the solidifiction is graphitic. Obviously this situation is not always true in the thin plates since they are characterized by higher cooling rates. EuLo and EuUp points are representative of the inoculation process: if there is a small difference between the found values (in a range of few $^\circ$C), inoculation can be considered successfull.

The CCA cups interact with the software OCC Phase Lab that displays approximated values of Carbon and Silicon content and the Liquidus, the Eutectic Metastable, and the End of Solidification points. According to the document by the supplier Heraeus Electro-Nite International N.V. [44], the formula used to calculate Carbon and Silicon content for ductile iron are the following ones:

$$\%C = -6.51 - 0.0084 * T_{\mathrm{L}} + 0.0178 * T_{\mathrm{E}} \tag{3.1}$$

$$\%Si = 78.411 - 4.28087 * Si_{\mathrm{adj}} - 0.06831 * (T_{\mathrm{E}} + 2.5) \tag{3.2}$$

T_{L} is Liquidus Point, T_{E} is Eutectic Metastable Point, Si_{adj} is a correction factor based on the P content (normally around 0.001 wt%). From what was found in these experiments, the results of these equations don't match the composition results obtained with the spectrometer for the GJS-500-14 and the GJS-600-10, while they confirm the composition for the GJS-400-15 and the GJS-450-18. The reason of this disalignment is that the correlation between Silicon content and Eutectic Temperature was found with a series of experiments with a Si content up to 3 wt%. These formula already have a correction coefficient introduced just for the higher Si content of ductile iron compared to grey cast iron. The Solid Solution strengthened ductile iron may need a further correction coefficient.

3.5.1 GJS-400-15 - Thermal Analysis

Figure 3.84: GJS-400-15 1ˢᵗ casting thermal analysis

Figure 3.85: GJS-400-15 1ˢᵗ casting, derivates of the thermal analysis curves

Figure 3.86: GJS-400-15 2nd casting thermal analysis

Figure 3.87: GJS-400-15 2nd casting, derivates of the thermal analysis curves

Table 3.5: GJS-400-15 1st casting critical points

Point	Temperature [°C]	Time [s]
Liquidus	1164.67	36.4
Eutectic Metastable	1108.17	106.4
End of Solidification	1116.29	190.4
EuLo	1153.47	81.46
EuUp	1155.76	109.67

Table 3.6: GJS-400-15 2nd casting critical points

Point	Temperature [°C]	Time [s]
Liquidus	1176	38.4
Eutectic Metastable	1109.08	117.4
End of Solidification	1116.96	188.4
EuLo	1154.02	88.95
EuUp	1155.16	113.04

3.5.2 GJS-450-18 - Thermal Analysis
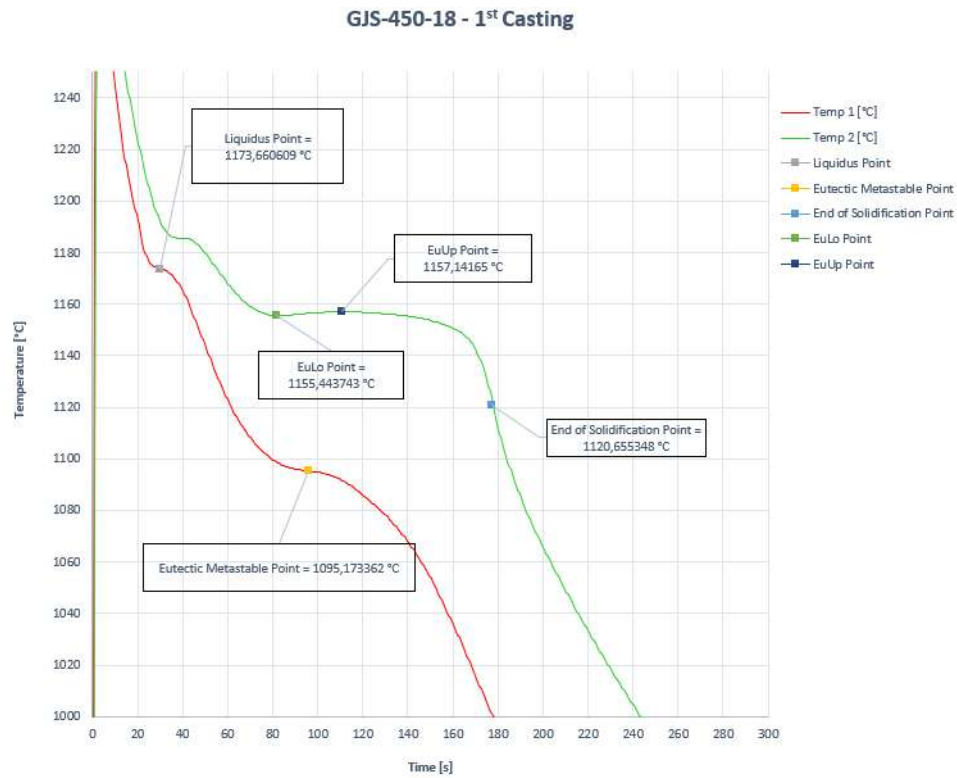
Figure 3.88: GJS-450-18 1st casting thermal analysis

Figure 3.89: GJS-450-15 1st casting, derivates of the thermal analysis curves
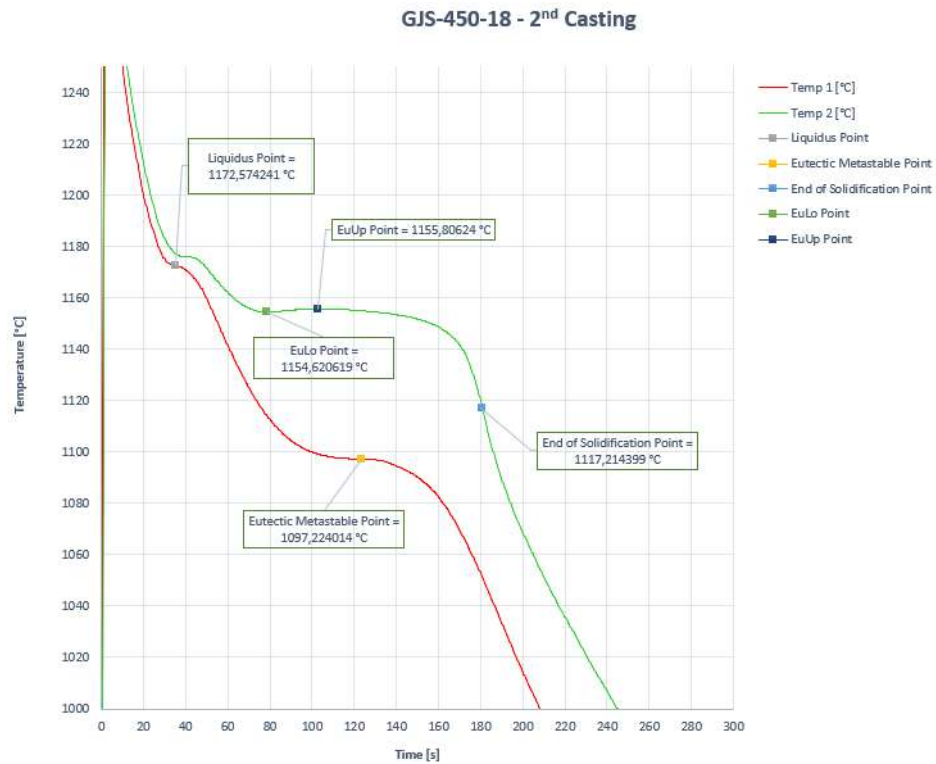
Figure 3.90: GJS-450-18 2nd casting thermal analysis
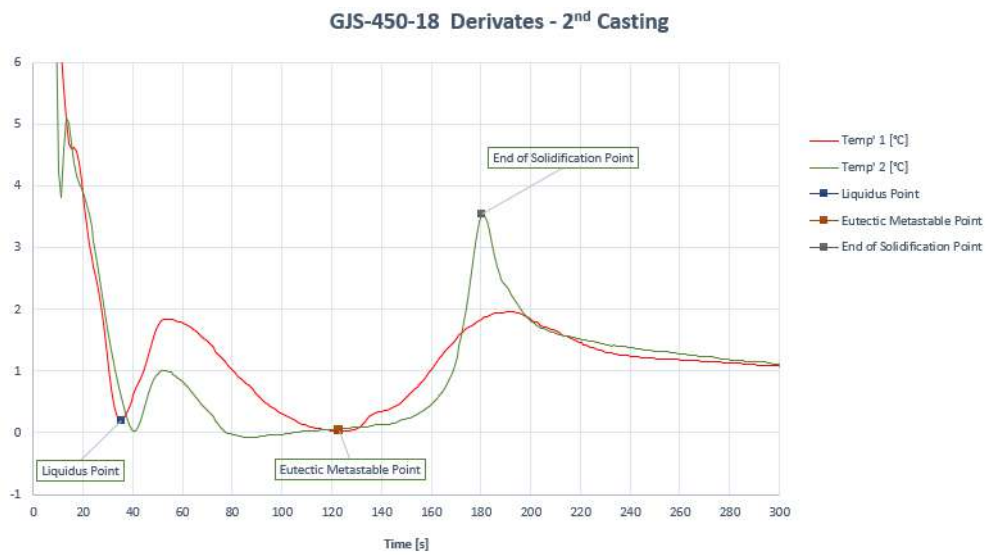
Figure 3.91: GJS-450-15 2nd casting, derivates of the thermal analysis curves

Table 3.7: GJS-450-18 1st casting critical points

Point	Temperature [°C]	Time [s]
Liquidus	1173.66	30.2
Eutectic Metastable	1095.17	96.2
End of Solidification	1120.66	177.2
EuLo	1155.44	81.93
EuUp	1157.14	110.5

Table 3.8: GJS-450-18 2nd casting critical points

Point	Temperature [°C]	Time [s]
Liquidus	1172.57	35.3
Eutectic Metastable	1097.22	123.3
End of Solidification	1117.21	180.3
EuLo	1154.62	78.23
EuUp	1155.81	103.05

3.5.3 GJS-500-14 - Thermal Analysis
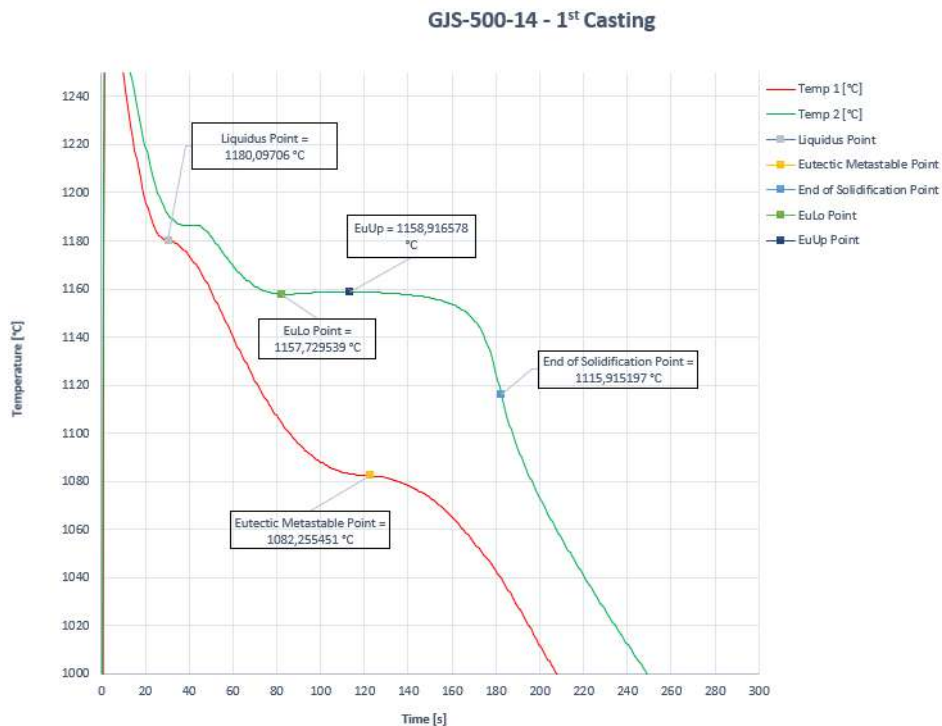
Figure 3.92: GJS-500-14 1st casting thermal analysis
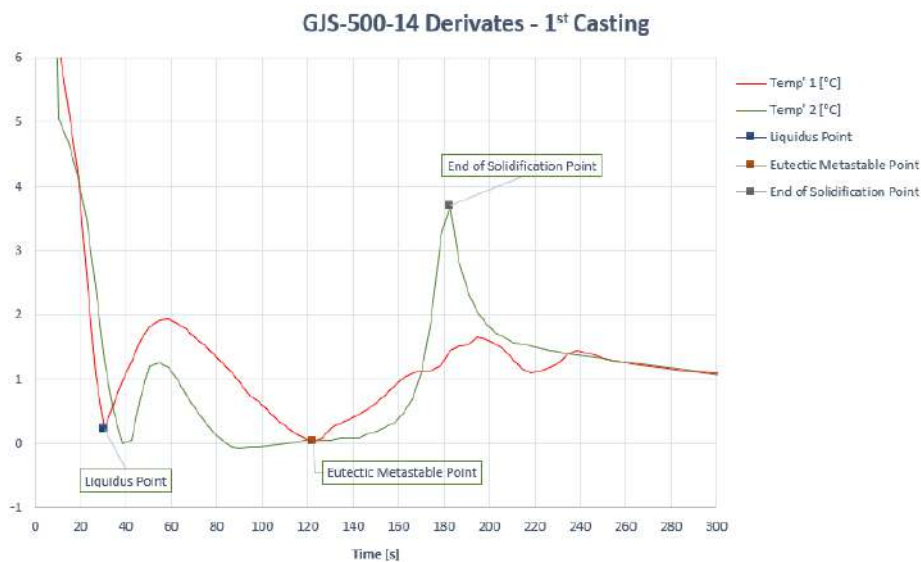
Figure 3.93: GJS-500-14 1st casting, derivates of the thermal analysis curves

Table 3.9: GJS-500-14 1st casting critical points

Point	Temperature [°C]	Time [s]
Liquidus	1180.1	30.5
Eutectic Metastable	1082.26	122.5
End of Solidification	1115.91	182.5
EuLo	1157.73	82.43
EuUp	1158.92	113.37

During the second casting trial a CCA disposable cup error didn't allow the correct calculation of the eutectic point, so that the permanent mold temperatures comparison was made using the data from the first GJS-500-14 casting.
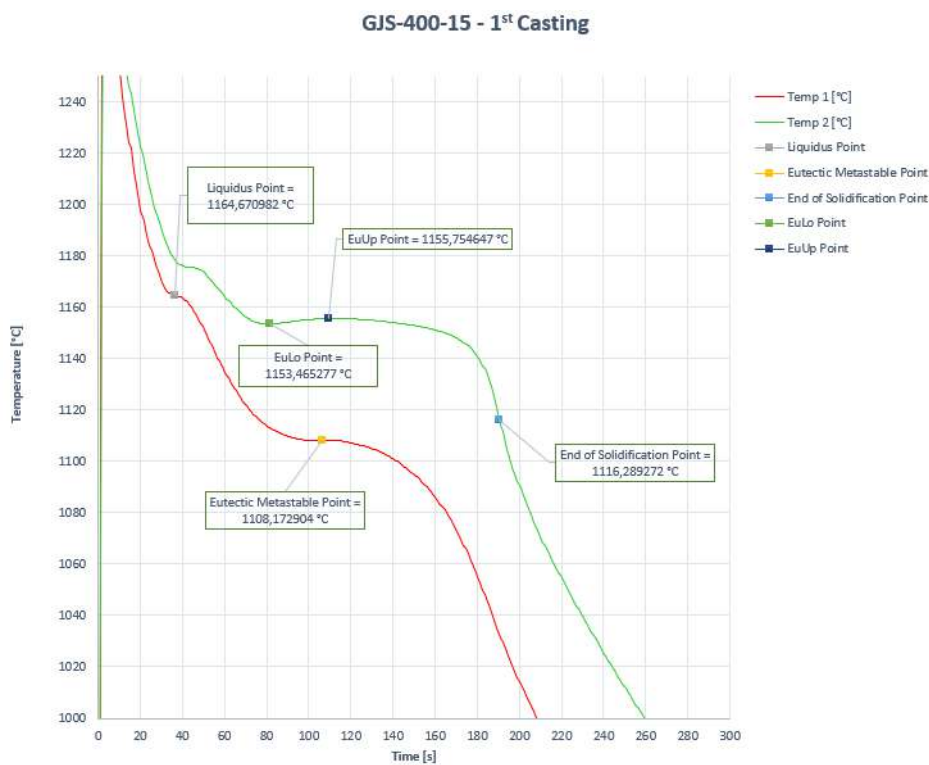
3.5.4   GJS-600-10 - Thermal Analysis
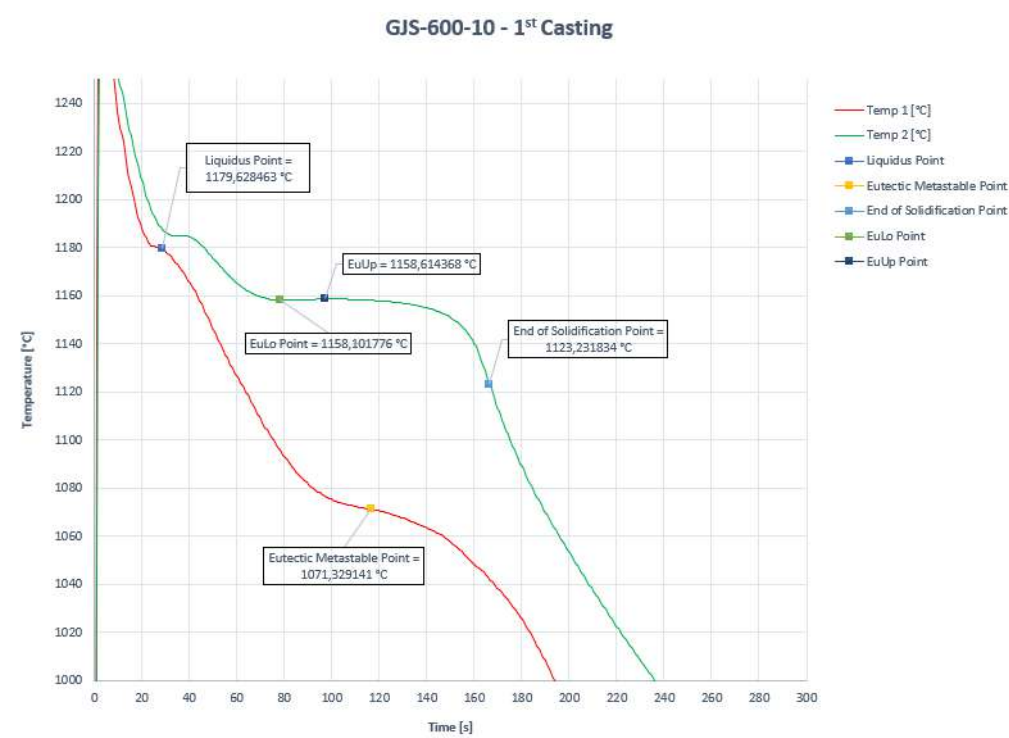
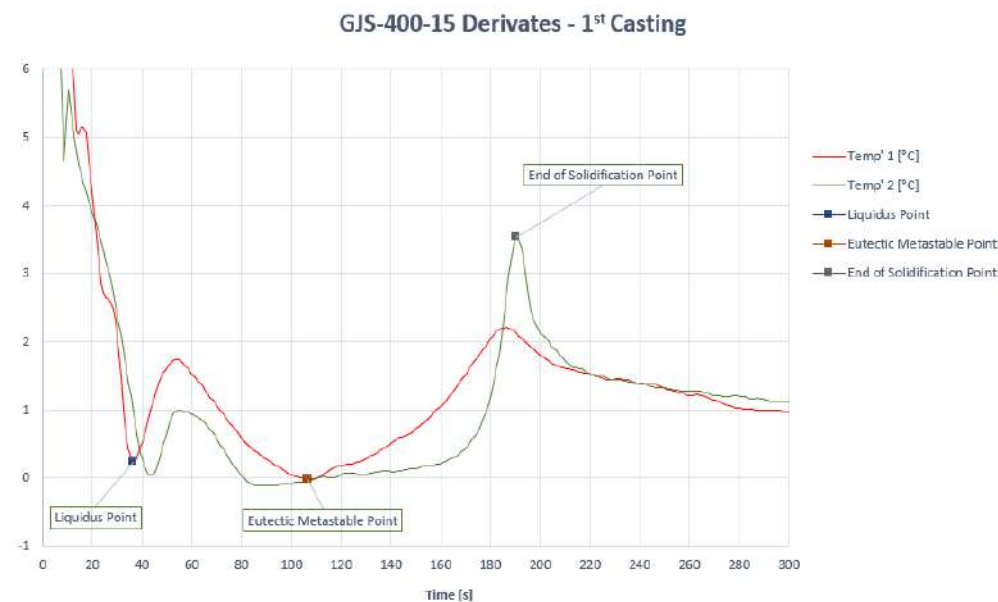*Figure 3.94: GJS-600-10 1st casting thermal analysis*
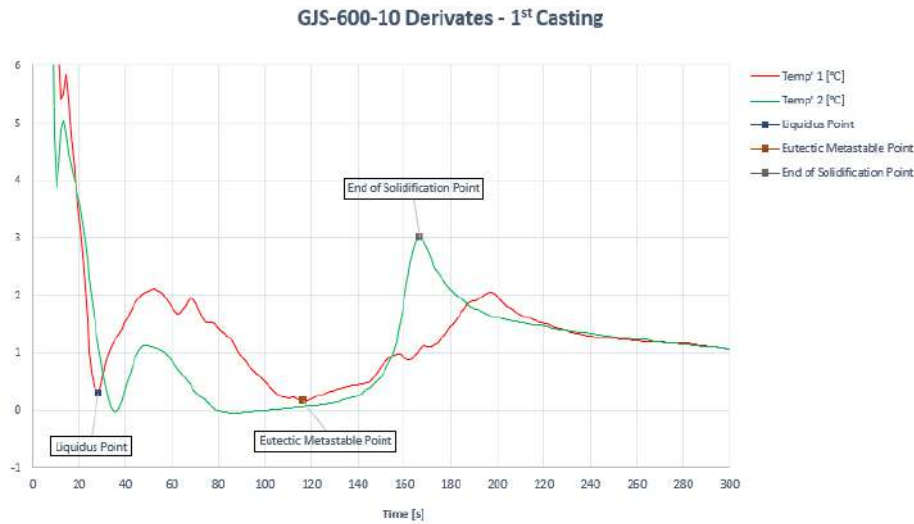
Figure 3.95: GJS-600-10 1st casting, derivates of the thermal analysis curves
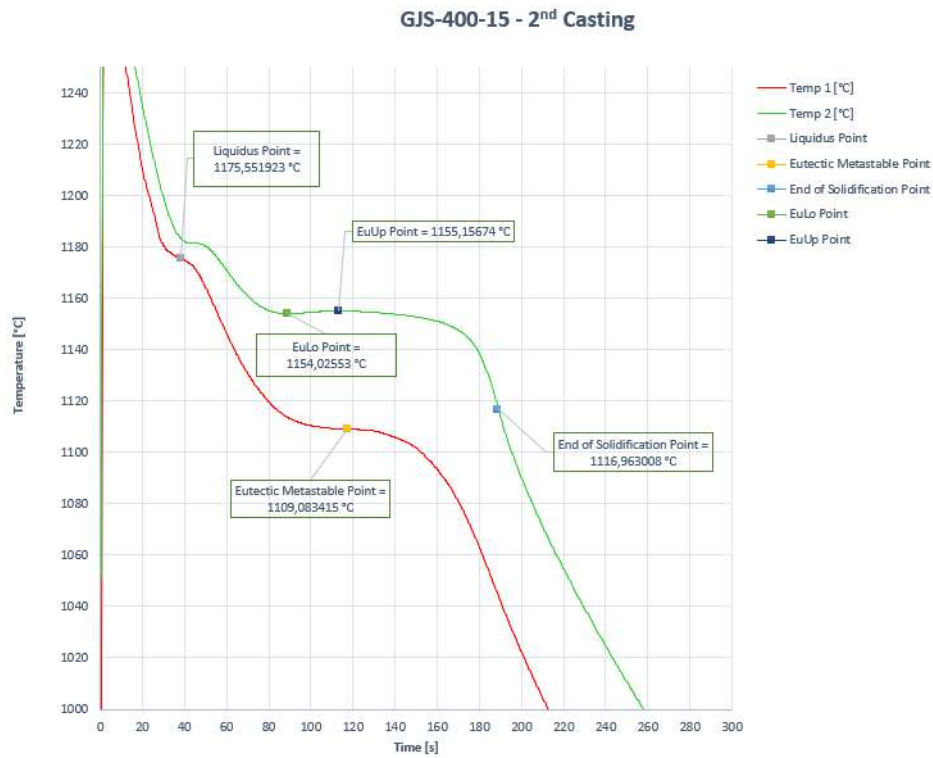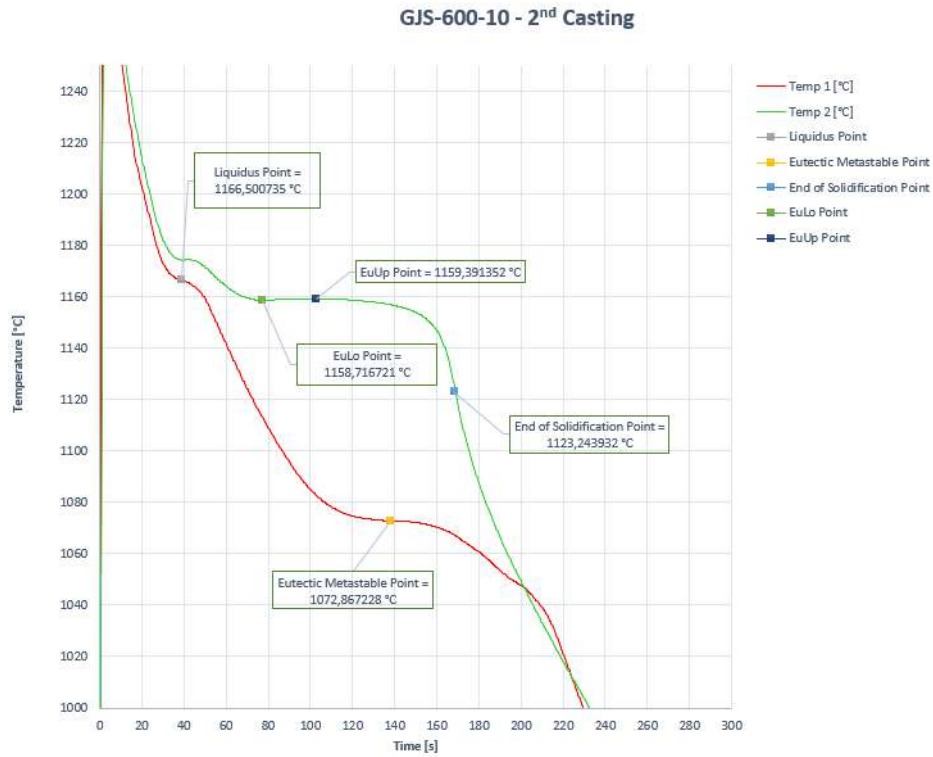
Figure 3.96: GJS-600-10 2nd casting thermal analysis
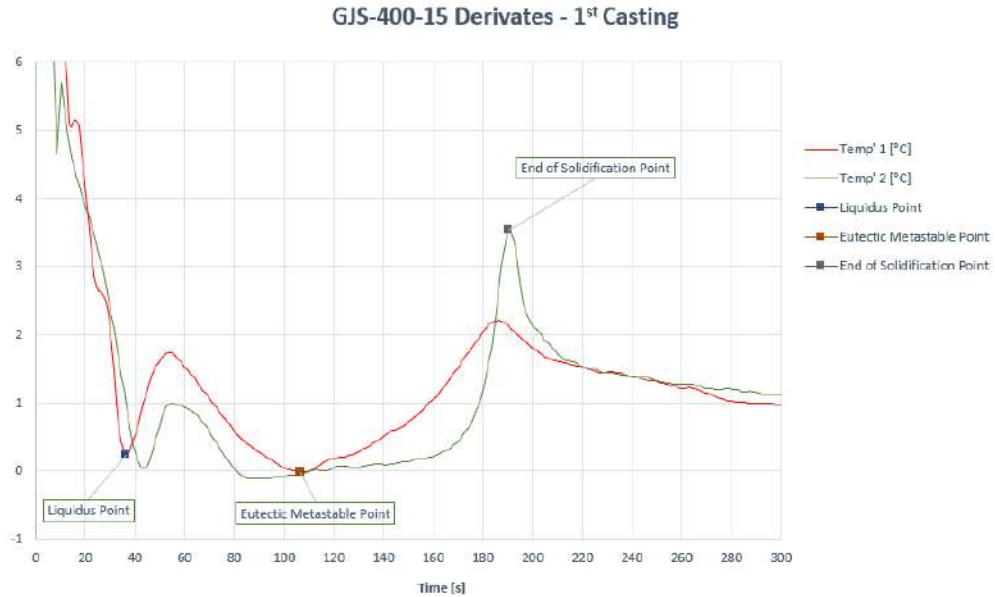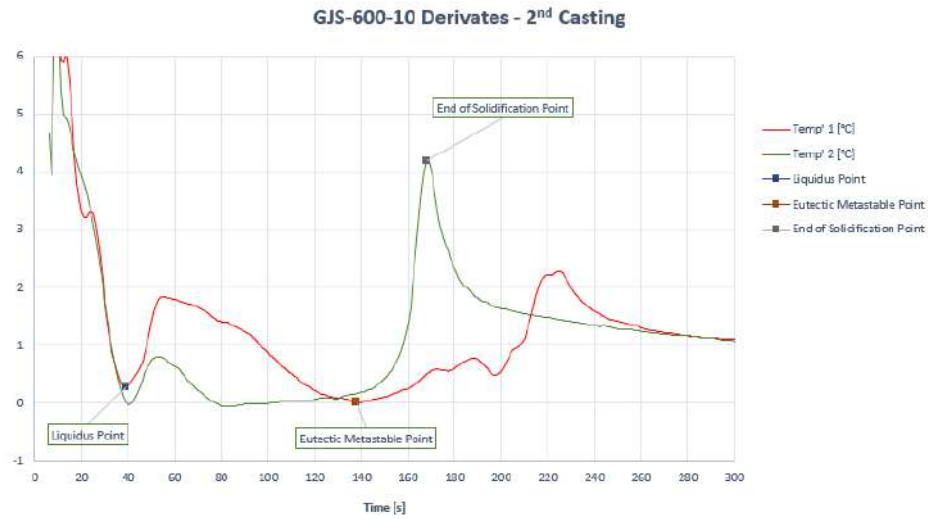

Figure 3.97: GJS-600-10 2nd casting, derivates of the thermal analysis curves

Table 3.10: GJS-600-10 1st casting critical points

Point	Temperature [°C]	Time [s]
Liquidus	1179.63	28.5
Eutectic Metastable	1071.33	116.5
End of Solidification	1123.23	116.5
EuLo	1158.10	78.25
EuUp	1158.61	97.27

Table 3.11: GJS-600-10 2nd casting critical points

Point	Temperature [°C]	Time [s]
Liquidus	1166.50	39
Eutectic Metastable	1072.87	138
End of Solidification	1123.24	168
EuLo	1158.72	77.42
EuUp	1159.39	102.80

3.6 Permanent Mold Thermal Analysis

The software PicoLog6 was used to register the cooling curves inside the permanent mold with the Type K thermocouples, and these curves were compared with the CCA data, to have a more consistent proof about the white solidification limits.

3.6.1 GJS-400-15 - Permanent Mold Thermal Analysis
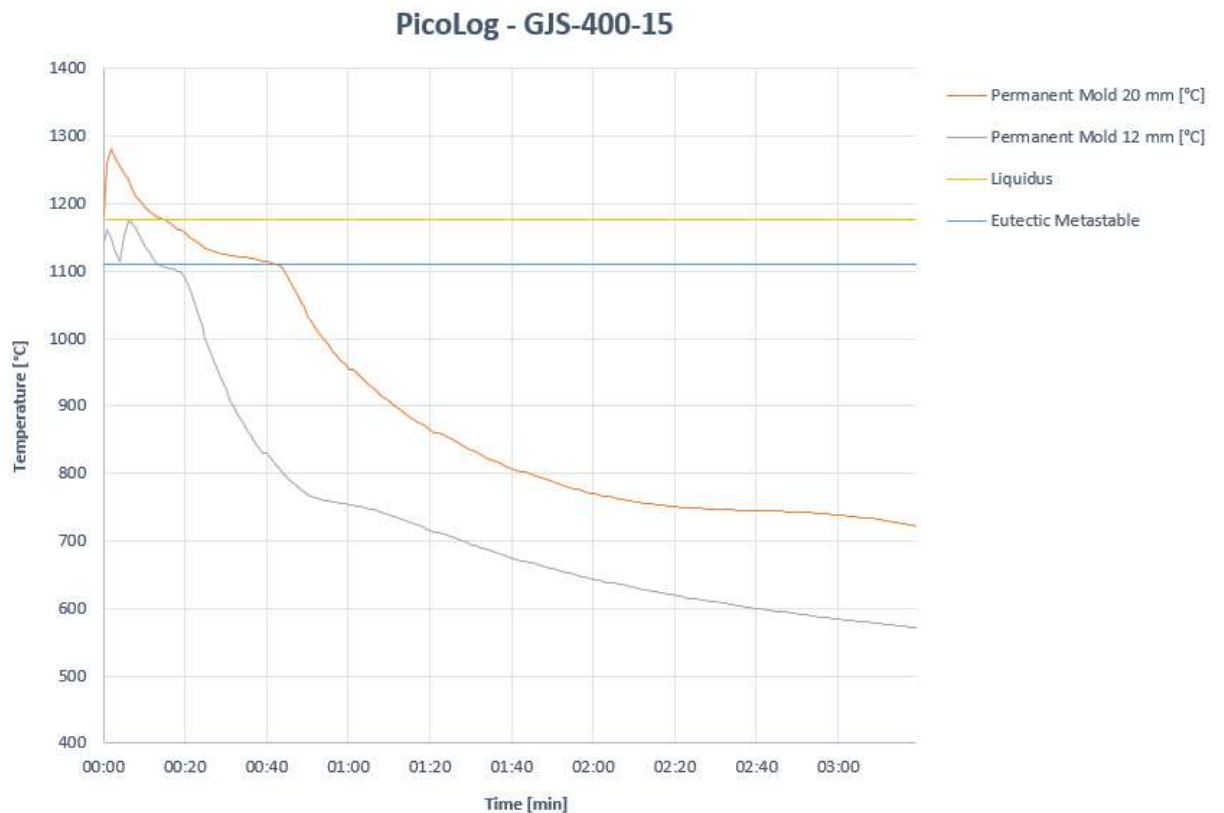
Figure 3.98: GJS-450-18 Permanent Mold Thermal Analysis

A connection misfunction of the 30 mm plate thermocouple didn't allow to display its result. However it can clearly be noticed how the 12 mm plate presents a white solidification, since the Metastable Eutectic Temperature of the alloy is higher than the recorded in the thinnest plate of the permanent mold, as well as it can be assumed that also the 20 mm plate presents a consistent amount of carbides (result confirmed by metallographic investigation).

3.6.2   GJS-450-18 - Permanent Mold Thermal Analysis
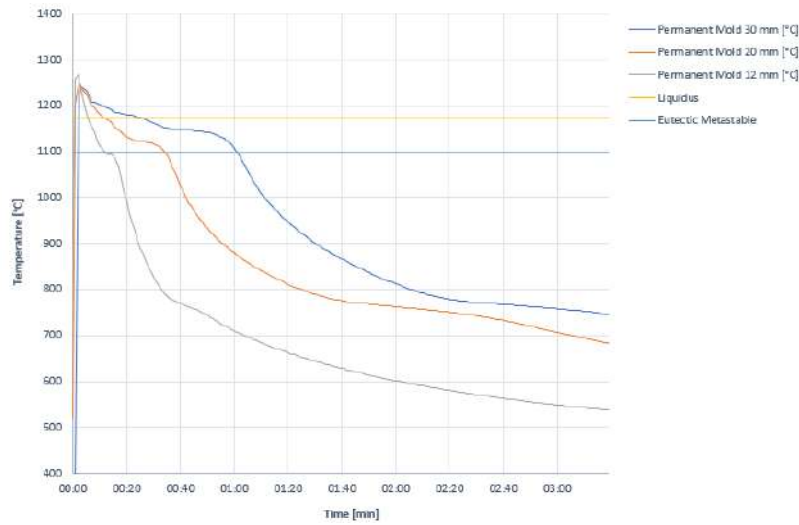
Figure 3.99: GJS-450-18 Permanent Mold Thermal Analysis

12 mm plate is to be considered white solified, as confirmed by the metallographic analysis. Both 20 and 30 mm plate are characterized by a ferritic matrix in the core, but they present a growing concentration of carbides as much as we get closer to the external surface.

3.6.3   GJS-500-14 - Permanent Mold Thermal Analysis
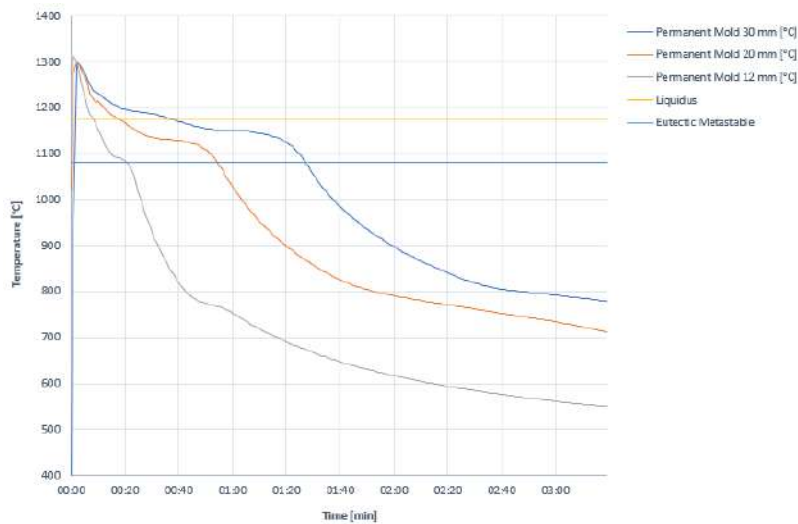
Figure 3.100: GJS-500-14 Permanent Mold Thermal Analysis

For the GJS-500-14, both 20 and 30 mm resulted carbide free, while the 12 mm wasn't, but surely with an improved structure compared to the GJS-450-18.

3.6.4   GJS-600-10 - Permanent Mold Thermal Analysis
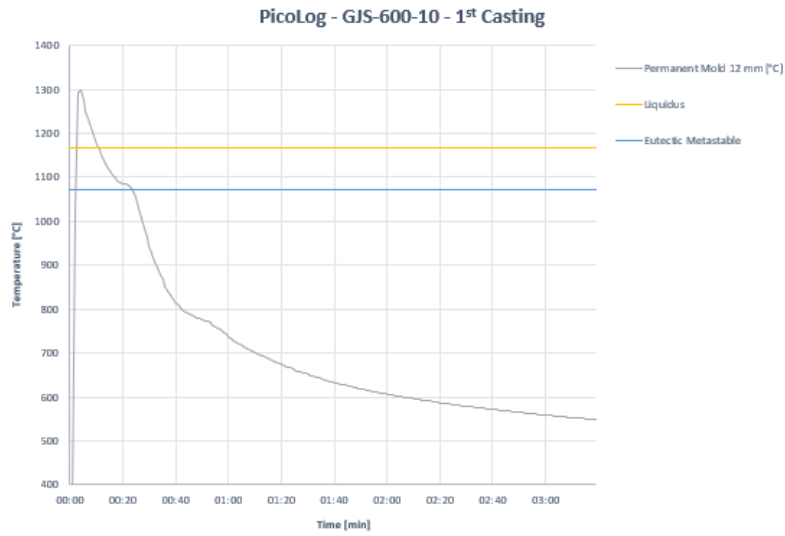
Figure 3.101: GJS-600-10 Permanent Mold Thermal Analysis (1)
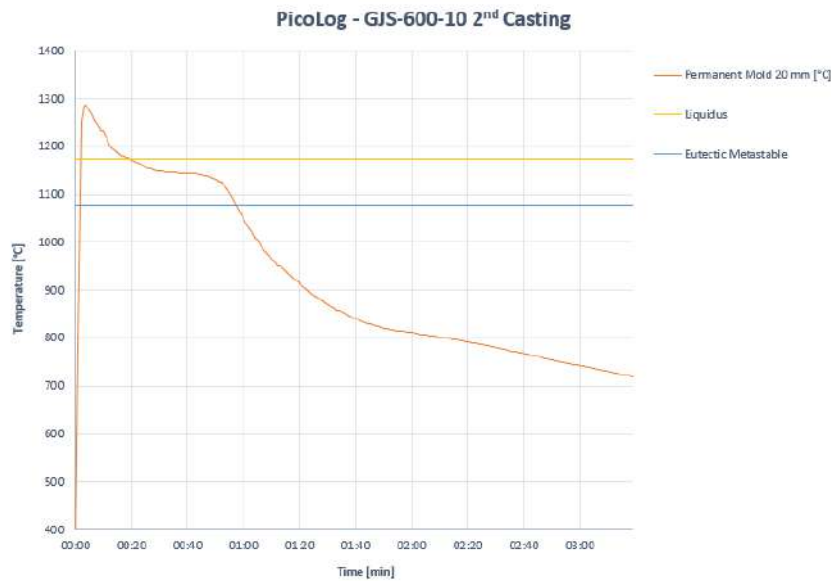
Figure 3.102: GJS-600-10 Permanent Mold Thermal Analysis (2)

It wasn't possible to obtain a full graphic due to thermocouples misfunctioning. An extra casting was performed just to record the curves, but just the 20 mm plates cooling temperature was recorded. From the metallographic analysis, it is confirmed that the 20 mm plates is carbide free, while the 12 mm still presents them, though in a lower quantity than all the other alloys.

3.7   Nodularity and Graphite Shape Analysis

For each sample, a quantitative analysis of the graphite nodules was realized. Each nodule was classified as a Type VI, V or IV, according to Velichko's formula exposed in paragraph 1.1 (Equation 1.7), through the parameters roundness and compactness. Also nodularity percentage could be calculated with Equation 1.7. Nodule count, number of nodules of type IV, V and VI, Nodule density and Nodularity percentage are presented in Table 3.12. Since the quantitative analysis involved every nodule of each sample image, every nodule that resulted having a MaxFeret < 5 μm (see Figure 1.6) was not taken in consideration to calculate roundness, compactness and nodule count. For all the others, the area in μm^2 was calculated, together with the Convex perimeter, necessary to calculate the Compactness parameter. Nodularity resulted over 85% in every sample analyzed, except for the 2 mm of the GJS-400-10 (46%, since it was white solified) and the GJS-500-14 (76%). Referring to the same alloy, nodule density changes amongst the two trials, since this value is strongly correlated to the casting conditions; for example, the 2.5 and the 4.5 mm plates of the GJS-500-14 present a nodule density of 873.78 and 762.58 Nodules / mm^2, respectively, while all the plates from the first casting have values that overcome 1000 Nodules / mm^2.

Table 3.12: Nodules Analysis main features. NC stands for Nodule Count, ND for Nodule Density, Nod for Nodularity percentag, WT for Wall Thickness

Alloy	WT [mm]	NC	Type IV + V	Type VI	ND [Num/mm^2]	Nod [%]
	2	575.6	313.6	55.6	972.86	46.07%
	3	213.8	61.4	140.2	531.23	88.63%
	4	209	55.8	139	513.31	84.88%
GJS-400-15	4.5	237.8	89.8	142	610.8	86.76%
	5	213	68.6	134.2	534.39	87.77%
	6	220.4	79.8	141.2	582.35	88.14%
	7	190.8	65.2	120	488.01	87.32%
	7.5	191.2	67.2	128.4	515.42	91.85%
	2	168.8	69.8	93.6	430.57	86.63%
	3	293.6	96.6	193.2	763.64	86.86%
GJS-450-18	3.5	343	80.8	262.4	904.35	91.13%
	4	308.2	85	205.4	765.22	88.55%
	5	289.8	79.2	203.6	745.19	91.64%
	6	290.6	68.6	220.6	762.06	91.97%

Alloy	WT [mm]	NC	Type IV + V	Type VI	ND [Num/mm²]	Nod [%]
	2	430.8	228.8	194.4	1115.15	76.83%
	2.5	334	120.4	211.2	873.78	82.81%
GJS-500-14	3	444.2	158.8	287.4	1175.76	86.87%
	4	406.2	104.2	295.6	1053.49	90.73%
	5	367.2	96	274	1041.9	93.77%
	2	289.2	104.4.	192.6	782.61	88.05%
	2.5	384	162.6	238.8	1057.71	84.54%
GJS-600-10	3	425.6	115.2	315.4	1134.65	91.83%
	4	385.6	84.8	308	1035.05	93.85%
	5	400	96.2	299.2	1041.9	93.77%

Nodule count is confirmed to rise for lower wall thicknesses until carbides are not present. As previously pointed out, since each casting had different thermal condition, amongst the same alloy just the plates of one single casting can be compared (for istance, in the second casting trial of the GJS-500-14, the 4.5 mm has a significantly lower nodule count than the 5 mm that was realized with the first casting trial).

3.8   Phases Area Analysis

A phases area analysis was also performed to determine the area fractions of cementite (if present), graphite, ferrite and perlite. The work was performed by the internal laboratories of the institute, examining the pictures taken from the digital light microscope. The analysis of the etched pictures made possible to distinguish dark areas (ferrite and eventually carbides) from white areas (graphite and pearlite), as shown in Figure 3.103. Since the calculation of graphite area percentage was possible with the analysis of the polished pictures (see Figure 3.104), the calculation of pearlite and ferrite was immediate if carbides were not present. Otherwise, to separate ferrite and carbides content, the MatLab software Ziehgitter 3.0 was used to approximate the ferrite content (see Figure 3.105). Results are exposed in Tables 3.13, 3.14, 3.15 and 3.16.
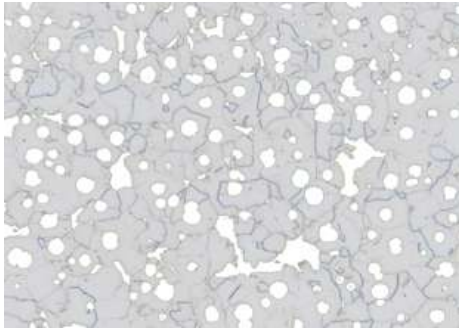
Figure 3.103: Area fraction analysis (1)
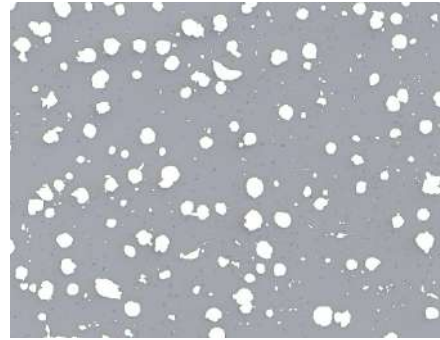
Figure 3.104: Area fraction analysis (2)

Figure 3.105: Ziehgitter 3.0 software

Table 3.13: GJS-400-15 Phases Area Percentage

GJS-400-15				
mm	G%	P%	F%	C%
2	8,46	60,82	0,79	29,92
3	7,15	66,94	6,16	19,75
4	9,85	55,29	27,96	6,90
4,5	6,04	47,61	46,35	0,00
5	11,77	43,55	44,69	0,00
6	7,36	33,29	59,35	0,00
7	8,42	31,03	60,55	0,00
7,5	10,47	24,96	64,57	0,00
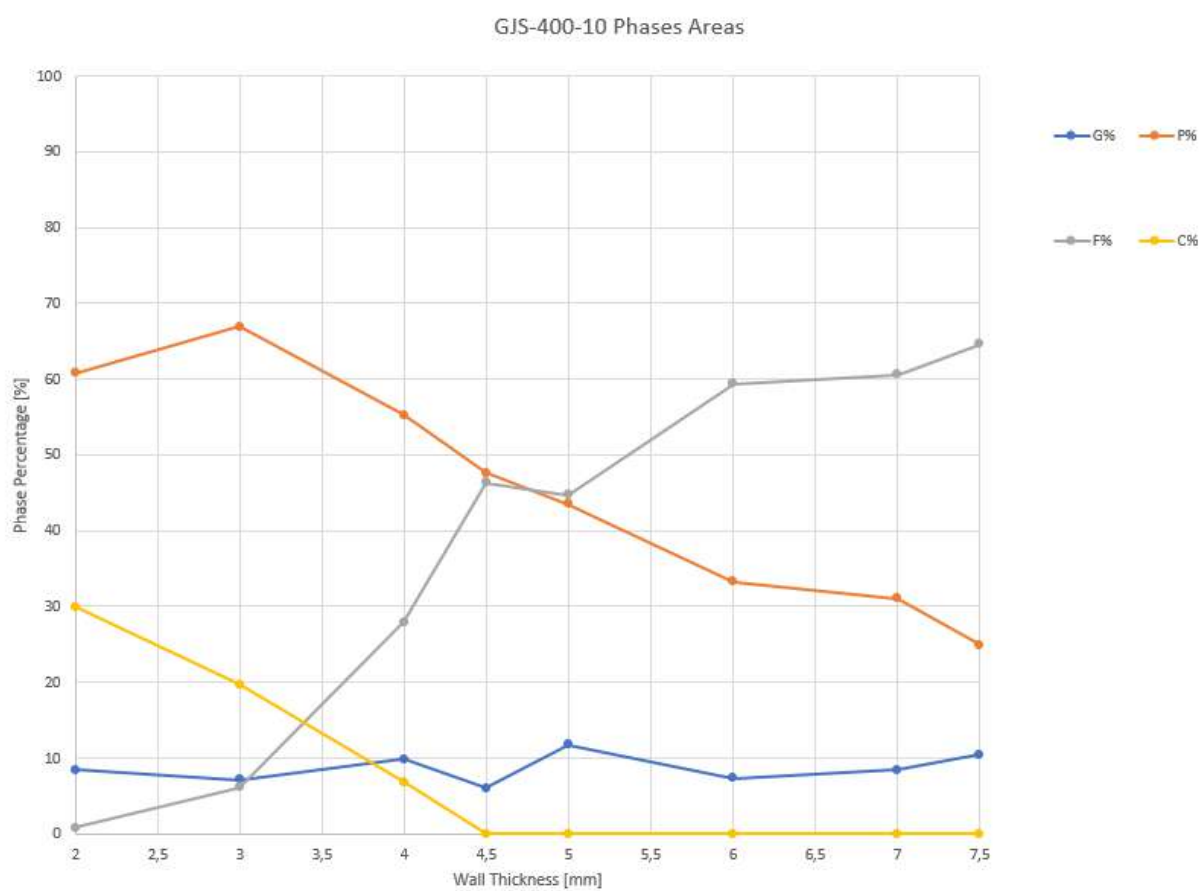
Figure 3.106: GJS-400-10 Phases Area Percentage Progression

Table 3.14: GJS-450-18 Phases Area Percentage

GJS-450-18				
mm	G%	P%	F%	C%
2	2,72	70,17	3,91	23,21
3	9,27	54,11	29,12	7,50
3,5	10,66	24,32	65,03	0,00
4	11,98	23,40	64,61	0,00
5	11,05	14,46	74,49	0,00
6	11,34	11,33	77,32	0,00
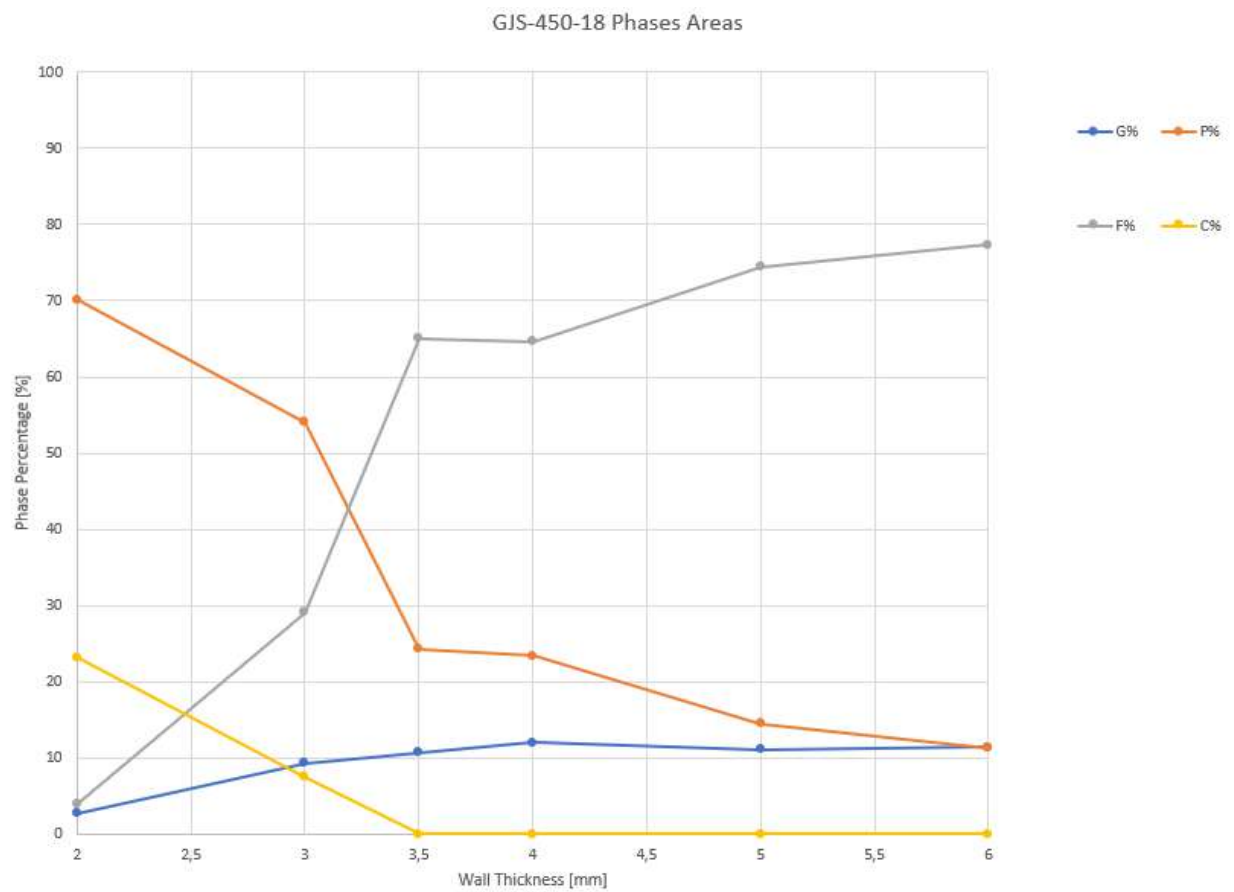
Figure 3.107: GJS-450-15 Phases Area Percentage Progression

GJS-500-14				
mm	G%	P%	F%	C%
2	10,62	64,01	18,32	7,05
2,5	9,63	28,13	58,67	3,57
3	11,34	13,68	74,98	0,00
4	11,94	5,31	82,75	0,00
5	11,13	2,68	86,20	0,00
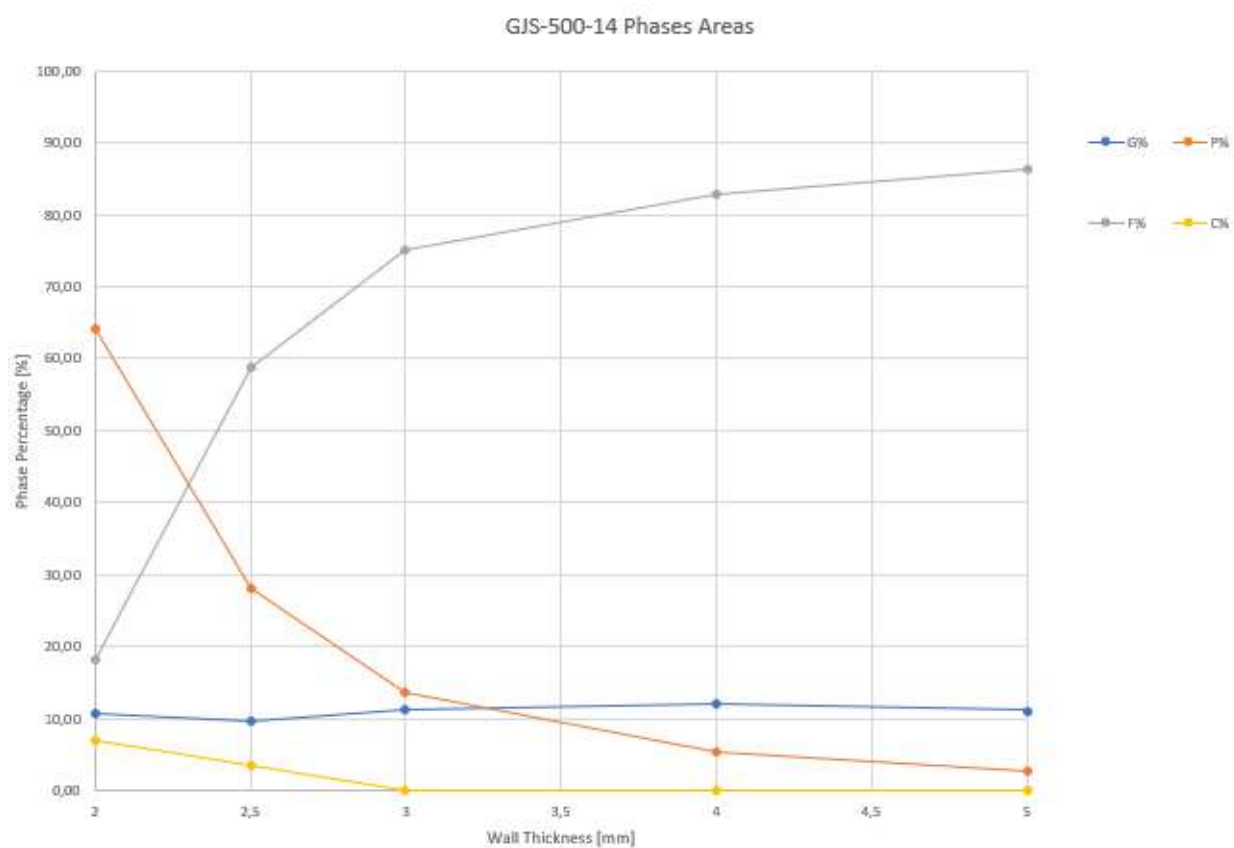
Figure 3.108: GJS-500-14 Phases Area Percentage Progression

Table 3.16: GJS-600-10 Phases Area Percentage

		GJS-600-10		
mm	**G%**	**P%**	**F%**	**C%**
2	5,68	63,90	22,10	8,32
2,5	8,10	24,58	60,00	7,31
3	11,61	15,44	72,95	0,00
4	10,78	2,14	87,09	0,00
5	11,84	0,50	87,66	0,00
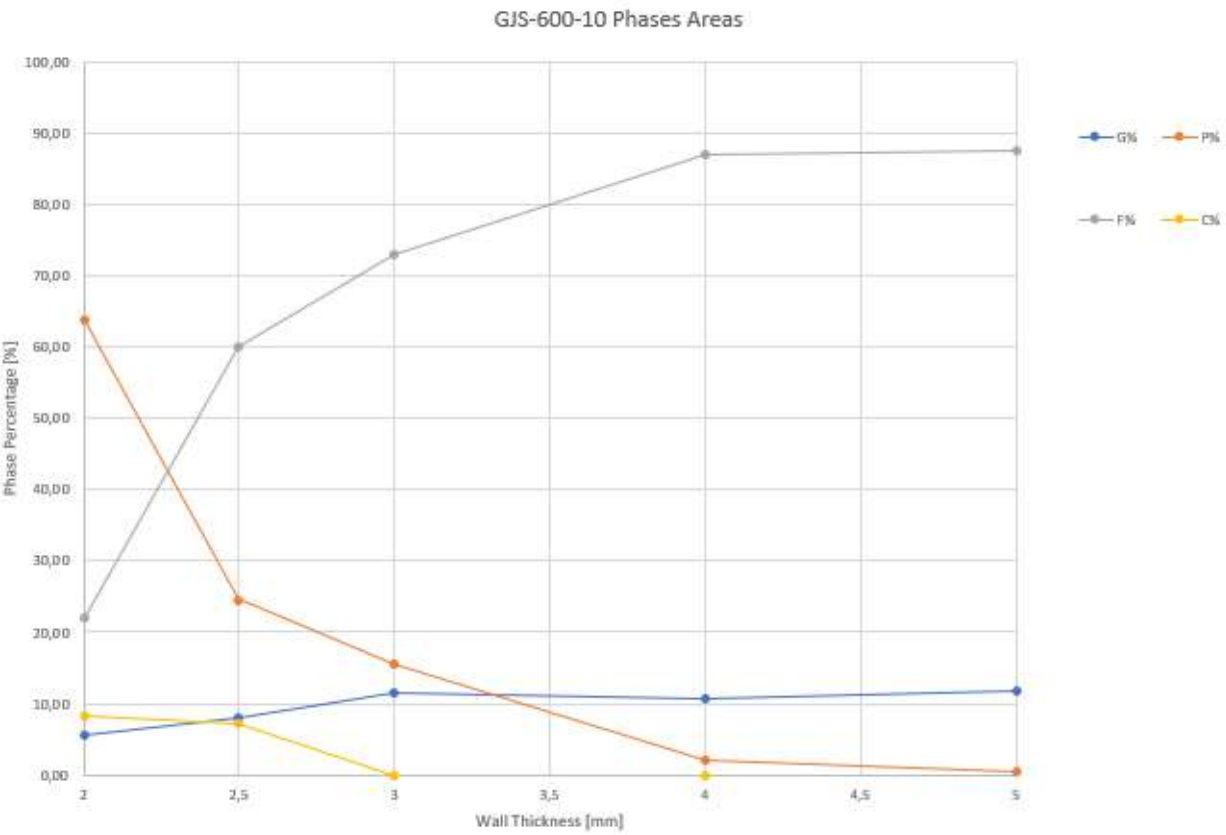
Figure 3.109: GJS-600-10 Phases Area Percentage Progression

The results confirm what expected. It is especially clear in the GJS-500-14 and in the GJS-600-10 that pearlite and ferrite have an anti - exponential and a logaritmic progression, respectively. The scattering of the plots in the GJS-400-15 and in the GJS-450-18 doesn't allow such a clear visual impact, but the tendency lines can be considered of the same shape. Cementite is present at low wall thicknesses and goes to zero at different values depending on the Silicon content. Graphite is lower at low wall thicknesses and stabilizes around 10 wt% when the structure is mostly ferritic.

3.9   Mechanical Tests Results

Tensile tests have been realized in *Gießerei-Institut*: Ultimate Tensile Strength, Yield Strength and Elongation have been measured for each carbide free sand mold plate of the four analyzed alloys, up to 5 mm. Two samples have been cut off from each plate, as shown in Figure ...DIN EN 1536 limits for these alloys are referreed to a fully ferritic matrix, so a match is possible only in the GJS-500-14 and in the GJS-600-10, while the other two alloys weren't found fully ferritic in the conditions of this work.

The results of the test are not constant: possible shrinkages or internal defects could have compromised the values found. Regarding the GJS-500-14, data are more linear than the other alloys; UTS is always reached, while Yield Strength is never above 14 %: at 5 mm the found value for one of the two samples is 12.57 %, probably for the pearlite content (2.68%). The expected values were on the other hand found for the GJS-600-10 at 4 mm (R_m = 662 MPa, A_t = 10.12 %). The pealite found in the 4 mm plate was 2.14%, and despite the fact that the 5 mm plate had 0.50%, the tensile values were low both for UTS and Yield Strength, most likely for the reasons discussed above. An higher number of plates and samples would be necessary to have a consistent database of results. Starting from GJS-400-15, results are exposed in Table 3.17, 3.18, 3.19, and 3.20.

A_t is the total extension (elastic plus plastic extension) at the moment of the fracture of the sample. That's the reason why is slightly higher than the A_{gt}, that stands for the maximum extension at the moment of the maximum force substained by the sample. E is the Elastic Modulus.

Table 3.17: GJS-400-15 Tensile tests results

Sample	R_m [MPa]	$R_{p0.2}$ [MPa]	A_t [%]	A_{gt} [MPa]	E [MPa]
GJS-400-15 4.5mm - A	643	480	1.73	1.73	173868
GJS-400-10 4.5mm - B	595	378	5.39	5.29	189597
GJS-400-15 5mm - A	612	425	2.36	2.35	147288
GJS-400-15 5mm - B	508	413	2.45	2.38	202879
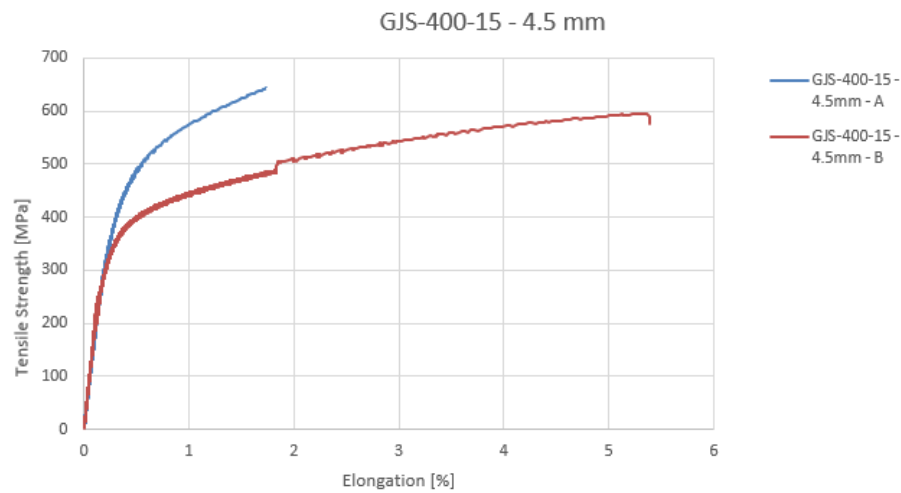
Figure 3.110: GJS-400-15 4.5 mm tests results
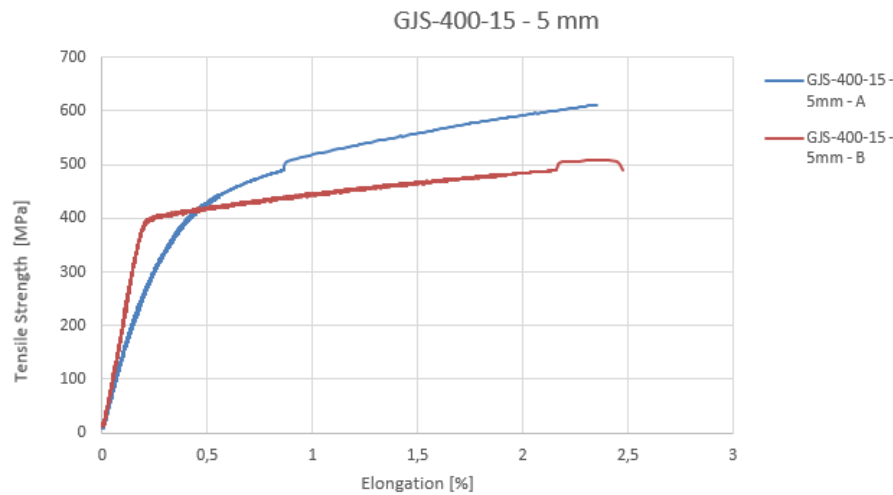
Figure 3.111: GJS-400-15 5 mm tests results

Table 3.18: GJS-450-18 Tensile tests results. Both the samples of the 3.5mm failed, one for a system failure, one because the Elastic Modul is too low, probably for a bad placement in the machine

Sample	R_m [MPa]	$R_{p0.2}$ [MPa]	A_t [%]	A_{gt} [MPa]	E [MPa]
GJS-450-18 4mm - A	664	480	5.21	5	172995
GJS-450-18 4mm - B	617	439	9.13	9.01	171806
GJS-450-18 5mm - A	517	380	5.44	4.91	178617
GJS-450-18 5mm - B	573	317	12.48	8.90	112196
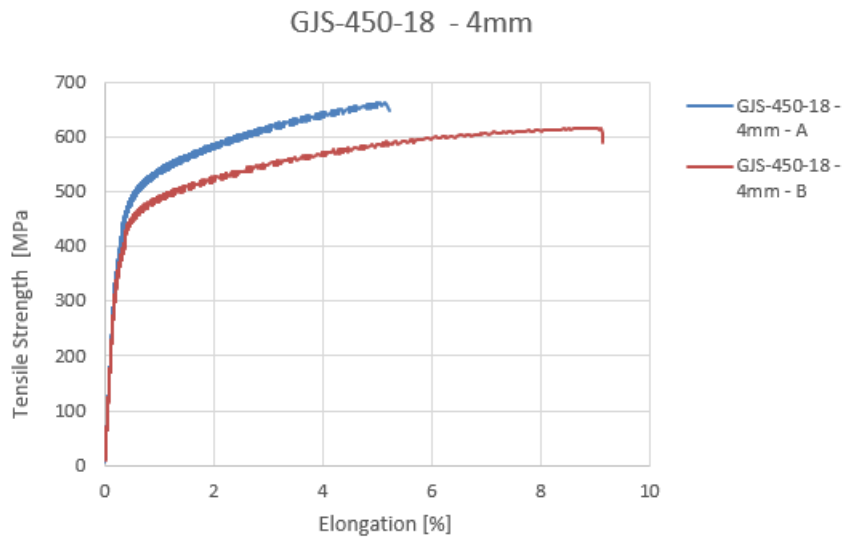
Figure 3.112: GJS-450-18 4 mm tests results
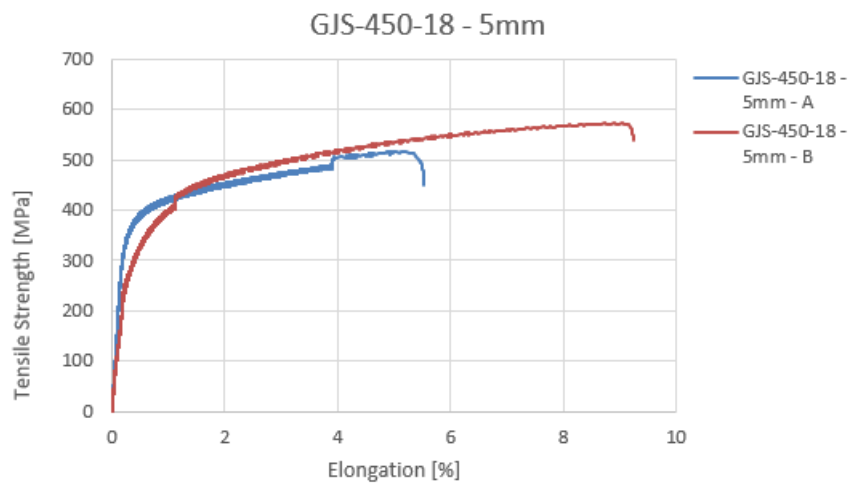
Figure 3.113: GJS-450-18 5 mm tests results

Table 3.19: GJS-500-14 Tensile tests results

| Sample	R_m [MPa]	$R_{p0.2}$ [MPa]	A_t [%]	A_{gt} [MPa]	E [MPa]
GJS-500-14 3mm - A	660	504	5.32	513	164258
GJS-500-14 3mm - B	623	456	6.25	6.17	151648
GJS-500-10 4mm - A	618	461	11.74	11.31	187329
GJS-500-14 4mm - B	589	432	12.07	11.15	163915
GJS-500-14 5mm - A	585	466	10.76	10.31	205882
GJS-500-14 5mm - B	577	429	12.57	10.78	160972
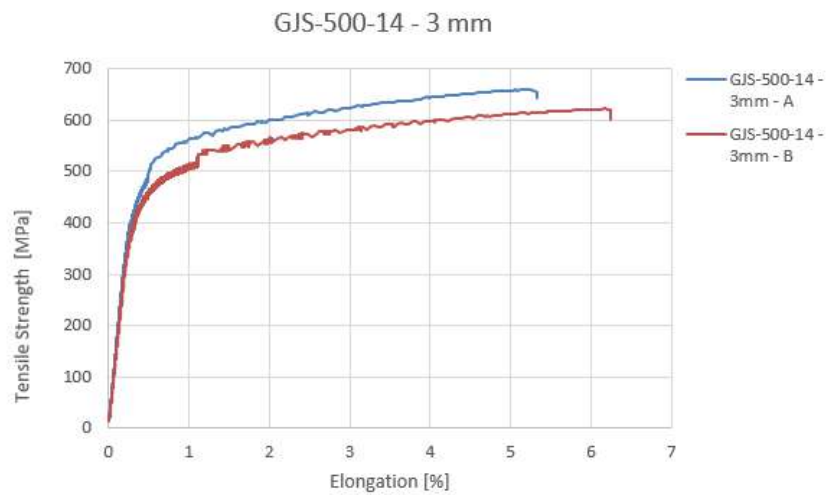
Figure 3.114: GJS-500-14 3 mm tests results
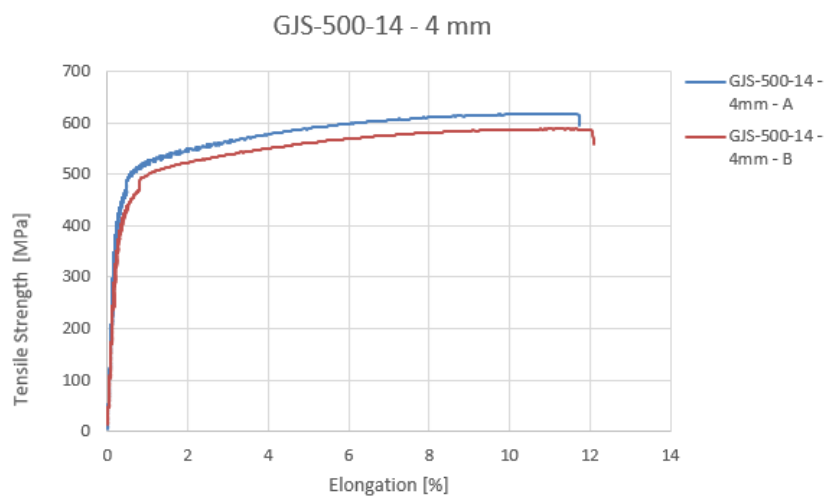
Figure 3.115: GJS-500-14 4 mm tests results

95
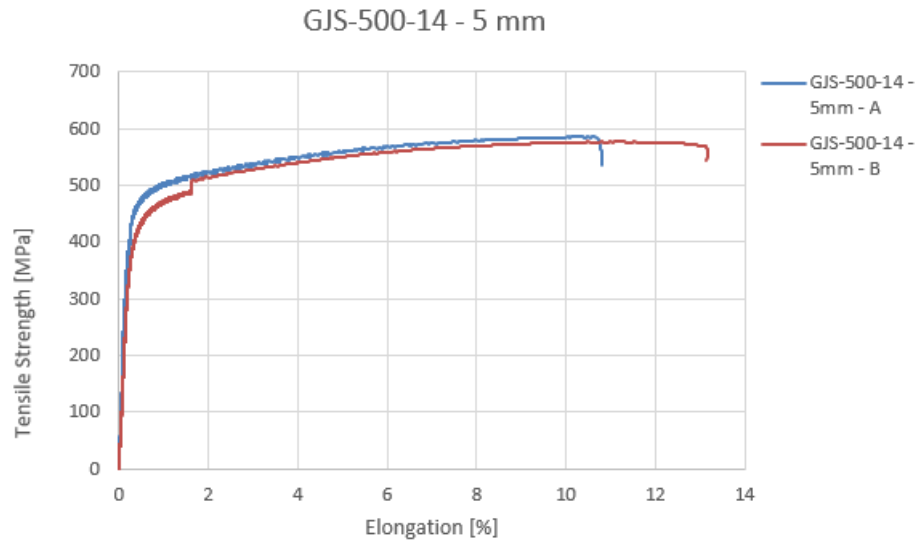
Figure 3.116: GJS-500-14 5 mm tests results

Table 3.20: GJS-600-10 Tensile tests results. GJS-600-10 3mm - A test failed

Sample	R_m [MPa]	$R_{p0.2}$ [MPa]	A_t [%]	A_{gt} [MPa]	E [MPa]
GJS-600-10 3mm - B	614	508	1.90	1.74	162973
GJS-600-10 4mm - A	601	496	4.60	4.75	175164
GJS-600-10 4mm - B	662	544	10.12	9.75	181503
GJS-600-10 5mm - A	599	507	3.52	3.30	185155
GJS-600-10 5mm - B	584	472	3.89	3.38	180339
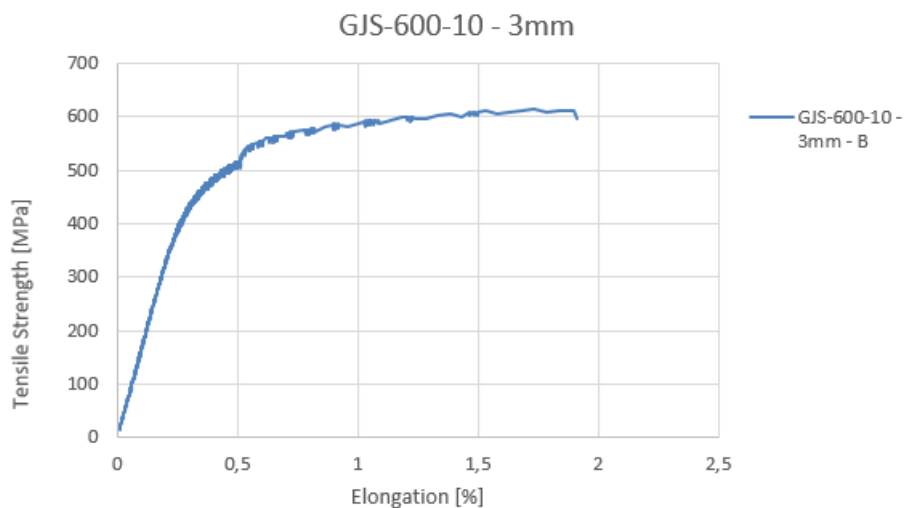
Figure 3.117: GJS-600-10 3 mm plate tensile tests results
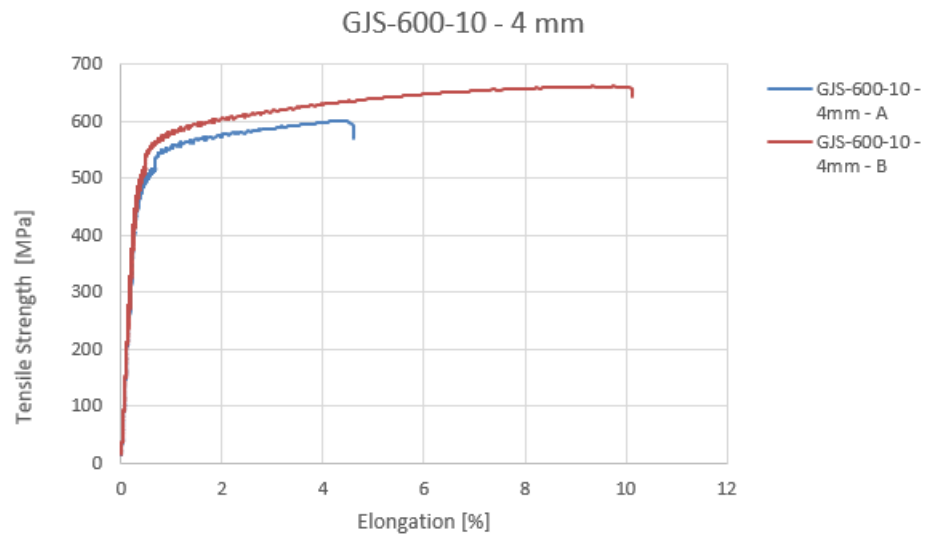
Figure 3.118: GJS-600-10 4 mm plate tensile tests results
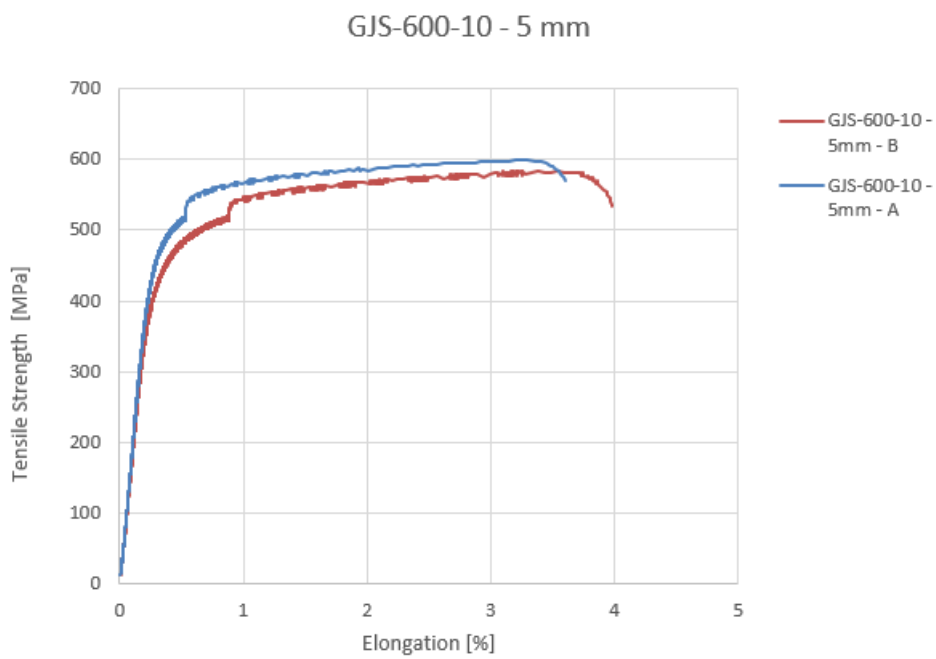
Figure 3.119: GJS-600-10 5 mm plate tensile tests results

3.10   Resume of the results

The goal of this project was to investigate the lightweight potential of Solid Solution Strengthened Ductile Iron (SSDI), both in chemically bonded green sand molds and in permanent metal mold (gravity die casting). The sand mold analysis focused on thin wall plates (initially 1-2-3-4-5 mm, each one with dimensions 15x10 cm), while the permanent mold steps were 30-20-12 mm, with dimensions 6x10 cm. The research aim was to found at which wall thickness it was possible to obtain a carbide free and a fully ferritic microstructure for each alloy considered (GJS-400-15, GJS-450-18, GJS-500-14, GJS-600-10, with a Silicon content of 2.4, 3.1, 3.8 and 4.3 wt%, respectively). Regarding the sand molds, after a first round of casting trials, a second one was performed with intermediate wall thicknesses. Initially, also a second round of castings with the permanent mold was programmed, due to determine the minimum pre heating temperature of the mold that allows to obtain the two microstructures exposed above. Unfortunately this last part of the experiments wasn't performed for reasons of time, but the results obtained confirm previous investigations. A possible suggestion for future investigations is to rise the minimum step and / or to rise the pre heating temperature.

Concerning the thin wall plates of the sand molds, it was possible to reach an as cast carbide free microstructure for every alloy, and a fully ferritic microstructure for the GJS-500-14 and the GJS-600-10, as exposed in Table 3.21. The permanent mold experiments, that came along with a thermal analysis that confirms the metallographic investigations, showed that it wasn't possible to obtain a carbide free matrix at the 10 mm step in none of the alloys, while a carbide free and a fully ferritic matrix was obtained at the 20 and 30 mm steps for the GJS-500-14 and the GJS-600-10.

Table 3.21: Sand Mold Plates Results

Alloy	Carbide Free Thickness [mm]	Fully Ferritic Thickness [mm]
GJS-400-10	4.5	-
GJS-450-18	3.5	-
GJS-500-14	3	$4 < x < 5$
GJS-600-10	3	$3 < x < 4$

Possible limiting factors of the experiments were the operating conditions of the Mg treatment and of the inoculation, that in foundries can be performed in-mold and at higher

temperatures, and the difficulty to control the pouring temperature (since the Mg treatment and the inoculation were not performed inside the molds, and even a few seconds can affect the undercooling of the melt). Due to these considerations, it is reasonable to compare the samples of th same alloy, but not reasonable to compare the same wall thickness for different alloys, expecially on the nodule count, that is heavily affected by the thermal conditions of the experiment.

Even though previous experiments led to carbide free microstructures at lower wall thicknesses for the GJS-400-15, the conditions of the experiments must be considered: for istance, a key role is played by the height of the plates and by the heat exchange surface in general. The reviewed experiments in the literature that had such results were performed at different geometrical conditions and with a double riser system ([7], [6]). Pedersen didn't use a double riser, and the surface area of his plates is slightly lower than the plates used in these experiment (13.000 mm^2 against 15.000 mm^2). The results for hypoeutectic ductile iron that he analyzed (Si content below 2.7 wt%) are comparable (carbides at 4.5 mm).

Mechanical tests, even if not consistent, show acceptable values for one of the samples of the GJS-600-10 at 4 mm (considered fully ferritic since it had a pearlite content of 2.14 wt%), 662 MPa for R_m and 10.12 % for A_t, and slightly unacceptable value for the Elongation at Fracture (12.57 % against 14 % necessary) for the GJS-500-14 at 5 mm (pearlite content of 2.68 wt%), that showed a 577 MPa for R_m. Acceptable values cannot be found for GJS-400-15 and for GJS-450-18 since fully ferritic plates were not found in the conditions of this experiment.

4 Conclusions

- This project was developed at the foundry institute of the RWTH University of Aachen, Germany. The purpose of this investigation was to analyze the lightweight potential of a family of graphitic high - silicon cast iron called Solid Solution Strengthened Ductile Iron (SSDI), officially recognised by the DIN EN 1563 since 2012.

- Using a suitable chemically bonded green sand mold and a permanent mold, several experiments were performed to determine the lowest possible wall thicknesses that could allow to obtain, for each alloy, a carbide free and a fully ferritic microstructure, in the larger frame of a possible improvement of the actually used ductile irons in terms of weight.

- The experiment followed the process described in Figure 2.1: starting from the review of the literature, the practical work then included the manual preparation of the molds, the setting of the casting and the preparation of the specimens to analyze. Metallo-grahic, thermal, and mechanical tests were perfomed to verify the requirements of the material.

- The results obtained are summed up in Figure 3.21. It was possible to find the wall thickness limits for a carbide - free and a fully ferritic microstructure, both for the GJS-500-14 and the GJS-600-10, while for the GJS-400-15 and for the GJS-450-18 it was only possible for the carbide - free microstructure.

- Compared to the results published in the literature, data are coherent. Still, different operating conditions surely lead to different results, as exposed in paragraph 3.10.

- Further investigations are possible, on different settings and variables, with the possil-ity to have an impact on the weight of ductile iron components used in the industrial world.

References

[1] C. Koffler and K. Rohde-Brandenburger. On the calculation of fuel savings through lightweight design in automotive life cycle assessments. *The International Journal of Life Cycle Assessment*, 15(1):128, 2010.

[2] H.C. Kim, T.J. Wallington, J.L. Sullivan, and G.A. Keoleian. Life cycle assessment of vehicle lightweighting: novel mathematical methods to estimate use-phase fuel consumption. *Environmental science & technology*, 49(16):10209–10216, 2015.

[3] U.S. Energy Information Administration. Monthly energy review (september 2018), 2018.

[4] E. Fraś, M. Górny, and H. Lopez. Thin wall ductile iron castings as substitutes for aluminium alloy castings. *Archives of Metallurgy and Materials*, 59(2):459–465, 2014.

[5] M. Pisanu and M. Brancia. La fonderia nel 2015, 2016.

[6] R.D. Sulamet-Ariobimo, J.W. Soedarsono, and T. P. Soemardi. Thin wall ductile iron castings. In *Advanced Casting Technologies*. IntechOpen, 2017.

[7] D.M. Stefanescu, L.P. Dix, R.E. Ruxanda, C. Crobitt-Coburn, and T.S. Piwonka. Tensile properties of thin wall ductile iron. *AFS Transactions*, 110, 2002.

[8] W. Stets, H. Löblich, G. Gassner, and P. Schumacher. Solution strengthened ferritic ductile cast iron properties, production and application. *International Journal of Metalcasting*, 8(2):35–40, 2014.

[9] Z. Glavas, A. Strkalj, and A. Stojakovic. The properties of silicon alloyed ferritic ductile irons. *Metalurgija*, 55(3):293–296, 2016.

[10] R. González-Martínez, U. de la Torre, A. Ebel, J. Lacaze, and J. Sertucha. Effects of high silicon contents on graphite morphology and room temperature mechanical properties of as-cast ferritic ductile cast irons. part ii - mechanical properties. *Materials Science and Engineering: A*, 712:803–811, 2018.

[11] F. Bonollo and A. Tiziani. La solidificazione delle ghise. *A cura di Franco Bonollo*, page 29, 2000.

[12] Franco Bonollo. Slide corso di chimica e materiali metallici, 2013.

[13] L.A. Morales-Hernández, F. Manríquez-Guerreroa, I.R. Terol-Villalobosa, , A. Domínguez-Gonzálezb, and G. Herrera-Ruizb. Caracterización de nódulos de grafito usando la técnica de morfología matemática. *Acta Microscópica*, 18(2):174–184, 2009.

[14] R.E. Ruxanda, D.M. Stefanescu, and T.S. Piwonka. Microstructure characterization of ductile thin-wall iron castings. *Transactions-American Foundrymens Society*, 2:1131–1148, 2002.

[15] A. Velichko and F. Mücklich. Quantitative 3d characterisation of graphite morphology in cast iron–correlation between processing, microstructure and properties. *International Journal of Materials Research*, 100(8):1031–1037, 2009.

[16] Moritz Riebisch, Hergen Groß Sönke, Björn Pustal, and Andreas Bührig-Polaczek. Influence of carbide-promoting elements on the pearlite content and the tensile properties of high silicon ssdi ductile iron. *International Journal of Metalcasting*, 12(1):106–112, 2018.

[17] K.M. Pedersen and N.S. Tiedje. Graphite nodule count and size distribution in thin-walled ductile cast iron. *Materials Characterization*, 59(8):1111–1121, 2008.

[18] J.O. Choi, J.Y. Kim, C.O. Choi, J.K. Kim, and P.K. Rohatgi. Effect of rare earth element on microstructure formation and mechanical properties of thin wall ductile iron castings. *Materials Science and Engineering: A*, 383(2):323–333, 2004.

[19] K.M. Pedersen. Solidification and microstructure of thin walled ductile cast iron. 2006.

[20] McGill University. Pearlite caught with sem, 2009.

[21] D.M. Stefanescu. Modeling of cast iron solidification—the defining moments. *Metallurgical and Materials Transactions A*, 38(7):1433–1447, 2007.

[22] H. Föll. Iron, steel and sword script.

[23] A. Merten. Die neue din en 1563:2012-03, 2012.

[24] R. Okunnu et al. High strength solution-strengthened ferritic ductile cast iron. 2015.

[25] Gopag c 500 f: Cast material for mechanical engineering with higher strength and breaking elongation and highly homogeneous hardness distribution.

[26] O.A. Partanen. Optimization of solid solution strengthened ferritic ductile iron production by thermal analysis and solidification simulation. 2016.

[27] T Skaland, Ø Grong, and T Grong. A model for the graphite formation in. *Metallurgical Transactions A*, 24(10):2321–2345, 1993.

[28] R. Ghasemi, J. Olofsson, A.E.W. Jarfors, and I.L. Svensson. Modelling and simulation of local mechanical properties of high silicon solution-strengthened ferritic compacted graphite iron. *International Journal of Cast Metals Research*, 30(3):125–132, 2017.

[29] M. Caldera, M. Chapetti, J.M. Massone, and J.A. Sikora. Influence of nodule count on fatigue properties of ferritic thin wall ductile iron. *Materials Science and Technology*, 23(8):1000–1004, 2007.

[30] H. Takeda, K. Asano, and H. Yoneda. Effect of bismuth on refinement of graphite in thin wall spheroidal graphite cast iron. *International Journal of Cast Metals Research*, 21(1-4):81–85, 2008.

[31] C.M. Ecob. A review of common metallurgical defects in ductile cast iron. *Customer Services Manager, Elkem AS, Foundry Products Division*, 2005.

[32] U. De La Torre, J. Lacaze, and J. Sertucha. Chunky graphite formation in ductile cast irons: effect of silicon, carbon and rare earths. *International Journal of Materials Research*, 107(11):1041–1050, 2016.

[33] R. González-Martínez, U. de la Torre, J. Lacaze, and J. Sertucha. Effects of high silicon contents on graphite morphology and room temperature mechanical properties of as-cast ferritic ductile cast irons. part i – microstructure. *Materials Science and Engineering: A*, 712:794 – 802, 2018.

[34] R.D. Sulamet-Ariobimo, J.W. Soedarsono, and B. Suharno. Cooling rate analysis of thin wall ductile iron using microstructure examination and simulation. *Applied Mechanics & Materials*, 2015.

[35] Foundry lexicon. www.giessereilexicon.com.

[36] Borui Castings International LTD. Typical defects of ductile iron castings.

[37] Ninxing new materials, www.foundrymaterial.com.

[38] Hashim Hassan Ahmed, Hashim Ahmed Ali, MM Mourad, and AA Nofal. Investigation of the parameters affecting the production and properties of thin-wall ductile iron casting. 2015.

[39] Moritz Riebisch, Christoph Seiler, Björn Pustal, and Andreas Bührig-Polaczek. Microstructure of as-cast high-silicon ductile iron produced via permanent mold casting. *International Journal of Metalcasting*, 13(1):112–120, 2019.

[40] T Kitsudo, Y Kawano, K Fujita, and S Kurose. The production of] as cast high elongation spheroidal graphite cast iron when cast in metal moulds. *Imono(Journal of the Japan Foundrymen's Society)*, 53(8):453–459, 1981.

[41] Jafar Khalil-Allafi and Behnam Amin-Ahmadi. Influence of mold preheating and silicon content on microstructure and casting properties of ductile iron in permanent mold. *Journal of Iron and Steel Research International*, 18(3):34–39, 2011.

[42] Ask chemicals, www.ask-chemicals.com.

[43] Ask chemicals, http://www.cometalsa.com.

[44] Heraeus Electro-Nite International N.V. Thermal analysis of cast iron.

[45] J.O. Olawale, S.A. Ibitoye, and K.M. Oluwasegun. Processing techniques and productions of ductile iron: A review. *International Journal of Scientific & Engineering Research*, 7:397–423, 2016.